


5-1-2017

Fast Neutron Detection in Nuclear Material Photofission Assay Using a 15 MeV Linear Electron Accelerator

Matthew Steven Hodges

University of Nevada, Las Vegas, hodgesm@unlv.nevada.edu

Follow this and additional works at: <https://digitalscholarship.unlv.edu/thesesdissertations>

 Part of the [Mechanical Engineering Commons](#), [Nuclear Commons](#), and the [Nuclear Engineering Commons](#)

Repository Citation

Hodges, Matthew Steven, "Fast Neutron Detection in Nuclear Material Photofission Assay Using a 15 MeV Linear Electron Accelerator" (2017). *UNLV Theses, Dissertations, Professional Papers, and Capstones*. 2986.
<https://digitalscholarship.unlv.edu/thesesdissertations/2986>

This Dissertation is brought to you for free and open access by Digital Scholarship@UNLV. It has been accepted for inclusion in UNLV Theses, Dissertations, Professional Papers, and Capstones by an authorized administrator of Digital Scholarship@UNLV. For more information, please contact digitalscholarship@unlv.edu.

FAST NEUTRON DETECTION IN NUCLEAR MATERIAL PHOTOFISSION ASSAY
USING A 15 MEV LINEAR ELECTRON ACCELERATOR

By

Matthew Hodges

Bachelor of Science in Engineering – Chemical Engineering
Arizona State University
2003

Master of Science in Engineering – Mechanical Engineering
University of Nevada, Las Vegas
2006

Master of Science – Materials and Nuclear Engineering
University of Nevada, Las Vegas
2015

A dissertation submitted in partial fulfillment
of the requirements for the

Doctor of Philosophy - Mechanical Engineering

Department of Mechanical Engineering
Howard R. Hughes College of Engineering
The Graduate College

University of Nevada, Las Vegas
May 2017

Copyright by Matthew Hodges, 2017

All Rights Reserved



Dissertation Approval

The Graduate College
The University of Nevada, Las Vegas

June 12, 2017

This dissertation prepared by

Matthew Hodges

entitled

Fast Neutron Detection in Nuclear Material Photofission Assay Using a 15 MeV Linear
Electron Accelerator

is approved in partial fulfillment of the requirements for the degree of

Doctor of Philosophy - Mechanical Engineering
Department of Mechanical Engineering

Alexander Barzilov, Ph.D.
Examination Committee Co-Chair

Kathryn Hausbeck Korgan, Ph.D.
Graduate College Interim Dean

Yi-Tung Chen, Ph.D.
Examination Committee Co-Chair

William Culbreth, Ph.D.
Examination Committee Member

Robert Boehm, Ph.D.
Examination Committee Member

Ke-Xun Sun, Ph.D.
Examination Committee Member

Daniel Gerrity, Ph.D.
Graduate College Faculty Representative

Abstract

FAST NEUTRON DETECTION IN NUCLEAR MATERIAL PHOTOFISSION ASSAY USING A 15 MEV LINEAR ELECTRON ACCELERATOR

by

Matthew Hodges

Dr. Alexander Barzilov, Examination Committee Co-chair

Associate Professor of Mechanical Engineering

University of Nevada, Las Vegas

Dr. Yi-Tung Chen, Examination Committee Co-chair

Co-Director, Center for Energy Research

Professor of Mechanical Engineering

University of Nevada, Las Vegas

The purpose of this research was to use a 15 MeV (K15 model by Varian) linear electron accelerator (linac) for the photon assay of special nuclear materials (SNM). First, the properties of the photon radiation probe were determined. The stochastic radiation transport code, MCNP5, was used to develop computational models for the linac. The spectral distribution of photons as well as dose rate contour maps of the UNLV accelerator facility were computed for several linac operating configurations. These computational models were validated through comparison with experimental measurements of dose rates.

The linac model was used to simulate the photon interrogation of SNM targets of various compositions and shielding materials. The spectra of neutrons produced by the irradiation of shielded SNM was characterized. The effects of shielding material and the SNM enrichment on

the neutron yields following photon assay were determined. It was determined that the radiation signatures following the photon assay of SNM consisted of photons and neutrons produced from the fissions, in addition to neutrons produced from photonuclear reactions.

The EJ-299-33A plastic scintillator was evaluated for this study due to its ability to discriminate between fast neutrons and gamma rays. The neutron coincidence measurement option was also evaluated. The detector response functions were determined for different incident neutron energies. Further, it was computationally shown that an array of EJ-299-33A detectors allows to measure neutron multiplicity, enabling discrimination between fission neutrons and the photoneutrons.

Acknowledgements

This dissertation would not have been possible without the help of many friends and colleagues. Specifically, I would like to thank my co-advisors, Dr. Alexander Barzilov and Dr. Yi-Tung Chen. Without their guidance and assistance, this dissertation would not have been possible. I have learned much from them, and hope that we can collaborate in the future.

The instruction and guidance provided by my dissertation committee - Dr. William Culbreth, Dr. Robert Boehm, Dr. Ke-Xun Sun, and Dr. Daniel Gerrity - proved invaluable in accomplishing my research goals.

I would like to thank Dr. Daniel Lowe of Varian Medical Systems. His understanding of the accelerators used in the study proved invaluable, as well as the MCNP insight and knowledge that he was kind enough to share. Additionally, I would like to thank Varian Medical Systems for the training and knowledge they provided.

I would like to thank the UNLV Graduate and Professional Student Association for the generous travel funding that I received in order to present this work at conferences across the country.

I would like to thank Joan Conway, the administrative assistant for the Department of Mechanical Engineering. Joan always looks out for engineering students and keeps us on the right track to graduation. Without Joan, I (and many other students) would be lost. Joan is the glue that holds the office together and UNLV is lucky to have her.

Lastly I would like to thank all the classmates that became my friends over the years. Without you all, I would not be here.

Dedication

To my family, who taught me the value of knowledge.

Table Of Contents

Abstract	iii
Acknowledgements.....	v
Dedication.....	vi
List of Tables	xi
List of Figures.....	xii
Chapter 1: Introduction.....	1
1.1 Motivation.....	1
1.2 Nuclear Safeguards and Security	2
1.3 Detection of Radioactive Materials	3
1.3.1 Passive Assay Methods.....	3
1.3.2 Active Interrogation Methods	4
1.3.3 Review of the Current State of Nuclear Material Assay Systems	7
1.4 Research Goals.....	13
1.5 Dissertation Outline	15
Chapter 2: Background	16
2.1 Fundamentals of Nuclear Physics.....	16
2.1.1 Nuclear Reactions	19
2.1.2 Types of Radiation.....	20
2.2 Radiation Interactions with Matter	20

2.2.1 Photon Interactions	20
2.2.2 Neutron Interactions.....	22
2.2.3 Photoabsorption Reactions.....	22
Chapter 3: Computational Modeling of Electron Linear Accelerators	26
3.1 The Electron Linear Accelerator.....	26
3.1.1 Production of Bremsstrahlung Photons	26
3.2 Dose and Biological Dose Equivalent	27
3.3 UNLV Accelerator Facility.....	28
3.3.1 Varian M6 Linac	30
3.4 Computational Modeling of the Linacs	33
3.4.1 Monte Carlo Methods	33
Chapter 4: Characterization of Radiation Generated by a Linac	35
4.1 Accelerator Facility Dose Rate Modeling.....	35
4.1.1 Accelerator Facility Layout	36
4.1.2 Radiation Source Term	36
4.1.3 Flux Tallies and Dose Rate Conversions	39
4.1.5 Determination of the Electron Current on the Linac Targets	42
4.2 Facility Dose Rates - Results	44
4.2.1.2 Electron Energy Cutoff.....	47
4.2.2 Radiation Environment During Operation of the M6	49

4.2.3 K15 Source Term Characterization	58
4.2.4 Radiation Environment During Operation of the K15 Linac.....	60
4.2.5 Summary of Linac Source Term Characterization	68
4.3 Accelerator Driven Photoneutron Source	69
4.3.1 MCNPX Model	71
4.3.3 Experimental Set-Up and Results	74
4.3.4 Model Validation	77
Chapter 5: Assay of SNM Using a 15 MeV Linac	79
5.1 Computational Model of SNM Assay.....	79
5.1.2 Modeling the active assay of SNM	84
5.2 Computational Results	85
5.2.1 Assay of Bare SNM	87
5.2.2 Assay of Shielded SNM.....	90
5.2.4 Neutron Spectra	100
5.2.4 Photon Spectra	105
Chapter 6: Neutron Detection	107
6.1 Scintillator Detectors	108
6.2 Pulse Shape Discrimination	113
6.3 Neutron multiplicity and coincidence counting	114
6.4 Computational Model of the Detector	116

6.5 Computational Results	120
6.5 Experimental Set-up.....	129
6.6 Experimental Results	130
Chapter 7: Conclusions	138
References.....	140
Curriculum Vitae	151

List of Tables

Table 1. SNM categories.....	3
Table 2. Subatomic particle data.....	16
Table 3. Neutron energy ranges [46]	19
Table 4. Common Neutron Binding Energies [48].....	23
Table 5. Radiation quality factors [60]	28
Table 6. Photon flux results, electron energy cutoff study	48
Table 7. Flux value similarity percentage.....	48
Table 8. Time savings using electron cutoff energies.....	49
Table 9. Linac configuration data	50
Table 10. Accelerator facility dose rates due to M6 operation	56
Table 11. K15 Linac configuration data	60
Table 12. Photoneutron binding energies of common materials [98].....	61
Table 13. UNLV linac characteristics.....	69
Table 14. Average number of neutrons per fission [124]	115

List of Figures

Figure 1. Fission process [8].....	6
Figure 2. Nuclear car wash [36].....	10
Figure 3. Electromagnetic spectrum [45].....	18
Figure 4. Photon interactions with matter [47]	21
Figure 5. Photonuclear cross sections (ENDF/B-VII.1) of Pu-239 [49].....	25
Figure 6. Production of bremsstrahlung photons [58]	26
Figure 7. UNLV accelerator facility	29
Figure 8. Accelerator facility layout	30
Figure 9. Varian M6 linac [64]	31
Figure 10. Varian M6 inside accelerator facility	31
Figure 11. Accelerator facility sample table	32
Figure 12. Varian K15 linac [66].....	32
Figure 13. Source term for M6 linac model.....	37
Figure 14. Gaussian spatial distribution of electrons on M6 target	38
Figure 15. Gaussian energy distribution of incident electrons on M6 target.....	38
Figure 16. Bremsstrahlung angular distribution	40
Figure 17. F5 tally locations, M6 characterization	41
Figure 18. M6 electron voltage, single pulse	43
Figure 19. M6 electron current, single pulse	43
Figure 20. M6 bremsstrahlung spectra for 3 MeV incident electrons	45
Figure 21. M6 bremsstrahlung spectra for 6 MeV incident electrons	45
Figure 22. Radial fluxes, 35 degree conical segment	46

Figure 23. M6 Configuration 1 dose rates, 6 MeV electrons.....	51
Figure 24. M6 Configuration 1 dose rates, 3 MeV electrons.....	51
Figure 25. M6 configuration 2 dose rates, 6 MeV electrons	53
Figure 26. M6 configuration 2 dose rates, 3 MeV electrons	53
Figure 27. M6 configuration 3 dose rates, 3 MeV electrons	54
Figure 28. M6 configuration 3 dose rates, 6 MeV electrons	55
Figure 29. Vertical dose rate, M6	57
Figure 30. K15 Bremsstrahlung spectra for 9 MeV incident electrons	58
Figure 31. K15 Bremsstrahlung spectra for 15 MeV incident electrons	59
Figure 32. K15 configuration 1 photon dose rates, 9 MeV electrons	62
Figure 33. K15 normal operation photon dose rate, 15 MeV electrons.....	62
Figure 34. Photon dose rate during normal operation of the K15 in high energy mode	63
Figure 35. Dose rates, K15 configuration 1, 15 MeV electrons	64
Figure 36. Photoneutron spectrum 1 m from K15 linac	65
Figure 37. K15 maximum photon dose rate, 15 MeV electrons.....	66
Figure 38. K15 maximum neutron dose rate, 15 MeV electrons.....	67
Figure 39. Au-198 decay scheme.....	70
Figure 40. Determination of photoneutron flux.....	72
Figure 41. Comparison of neutron fluxes based on converter orientation.....	73
Figure 42. Photoneutron spectrum, 1 cm behind collimator cavity.....	74
Figure 43. M6 linac setup used for photoneutron production.....	75
Figure 44. Experimental equipment a) ORTEC HPGe detector and b) a gold activation foil	76
Figure 45. Activated gold foil spectrum	76

Figure 46. Calculating the number of reactions in MCNPX	77
Figure 47. The photon SDEF	80
Figure 48. Bremsstrahlung spectra, 1 cm from linac	81
Figure 49. MCNPX output - photon creation results	82
Figure 50. SDEF source check, 10 degree angle at 10 cm from source	83
Figure 51. ACT card example.....	84
Figure 52. Tally tagging example	85
Figure 53. Reactions occurring during photofission assay of shielded SNM.....	87
Figure 54. Uranium photoabsorption cross sections.....	88
Figure 55. Plutonium photoabsorption cross sections	88
Figure 56. Neutron fluxes during assay of bare weapons grade SNM	89
Figure 57. Neutron fluxes during assay of lead shielded weapons grade SNM	90
Figure 58. Bremsstrahlung spectra at 1 meter from K15 linac	91
Figure 59. Neutron fluxes during assay of polyethylene shielded weapons grade SNM	92
Figure 60. Photonuclear cross sections for shielding materials.....	93
Figure 61. Neutron fluxes during assay of lead and polyethylene shielded weapons grade SNM.....	94
Figure 62. Total neutron fluxes for photon assay of SNM	95
Figure 63. Fission neutron fluxes for photon assay of SNM	95
Figure 64. Fraction of fission neutrons at 1 cm behind SNM.....	96
Figure 65. Enrichment effects on the total neutron flux	98
Figure 66. Enrichment effects on the fission neutron flux.....	98
Figure 67. Enrichment effects on the fission neutron fraction.....	99
Figure 68. Spectra of neutrons generated during photon assay of unshielded uranium	100

Figure 69. Spectra of neutrons generated during photon assay of uranium with 5 cm polyethylene shielding.....	101
Figure 70. Spectra of neutrons generated during photon assay of uranium with 5 cm lead shielding.....	101
Figure 71. Spectra of neutrons generated during photon assay of uranium with 5 combination shielding.....	102
Figure 72. Spectra of neutrons generated during photon assay of unshielded plutonium	103
Figure 73. Spectra of neutrons generated during photon assay of plutonium with 5 cm polyethylene shielding	103
Figure 74. Spectra of neutrons generated during photon assay of plutonium with 5 cm lead shielding.....	104
Figure 75. Spectra of neutrons generated during photon assay of plutonium with 5 cm combination shielding.....	104
Figure 76. Spectra of photons generated during photon assay of plutonium with polyethylene shielding.....	105
Figure 77. EJ-299-33A plastic scintillator	109
Figure 78. PMT.....	109
Figure 79. Detector apparatus	110
Figure 80. PID components of a digital signal [123].....	114
Figure 81. Tallies, detector response to monoenergetic neutrons.....	117
Figure 82. Neutron multiplicity computational model set	118
Figure 83. Tallies, neutron coincidence modeling.....	119
Figure 84. EJ-299-33A response functions for monoenergetic neutron source.....	120

Figure 85. EJ-299-33A response function components for 2 MeV neutron source	121
Figure 86. EJ-299-33A response function components for 6 MeV neutron source	121
Figure 87. EJ-299-33A response function components for 15 MeV neutron source	122
Figure 88. Particle contribution to energy deposition in EJ-299-33A	123
Figure 89. EJ-299-33A singlet responses for WG Pu surrounded by lead shielding	124
Figure 90. EJ-299-33A doublet responses for WG Pu surrounded by lead shielding	125
Figure 91. EJ-299-33A singlet responses for SNM fission sources	126
Figure 92. EJ-299-33A doublet responses for SNM fission sources	127
Figure 93. EJ-299-33A triplet response for plutonium fission source.....	127
Figure 94. EJ-299-33A multiplet responses for (α ,n) source	129
Figure 95. UNLV 2 Ci PuBe source	130
Figure 96. Digital pulses from PuBe source [109]	131
Figure 97. PID values, PuBe source [109].....	132
Figure 98. Number of PID counts, PuBe source [109].....	133
Figure 99. PID values, Co-60 source [109]	134
Figure 100. Number of PID counts, Co-60 source [109].....	134
Figure 101. Cobalt-60 Decay Scheme	135
Figure 102. Coincident photon experimental setup [109]	136
Figure 103. Coincident photon pulses, Co-60 source, separated [109]	136
Figure 104. Coincident photon pluses, Co-60 source, combined [109].....	137

Chapter 1: Introduction

1.1 Motivation

After the September 11, 2001 terrorist attacks in New York City, national security issues - particularly scenarios involving the detonation of a nuclear weapon - have become a dominant concern. The consequences of the detonation of a nuclear weapon would be catastrophic for life, critical infrastructure, the environment, as well as the economy. The probability of smuggling an assembled nuclear weapon is less than that of the smuggling of the components needed to construct such a weapon. Moreover, the proliferation of nuclear materials is of concern.

Maritime (oceanic) transport is the backbone of international trade, accounting for around 80% of global trade by volume (70% by value) [1]. In 2014, more than eighteen million marine shipping containers entered the U.S., with more than 58% arriving at the largest three seaports – Los Angeles (4.4 million), Long Beach (3.5 million) and New York-New Jersey (3.0 million) [2]. Currently, only 6% of these containers are physically opened and inspected by customs service due to the need for commerce to continually flow [3]. Great concern lies in the idea that small amounts of special nuclear material (SNM) may enter into the U.S. by smuggling them within these shipping containers. The low physical inspection percentage of maritime containers coupled with the catastrophic effects of a nuclear detonation, has led to an increase in research efforts into the detection of nuclear materials. Accurate detection of SNM is necessary to prevent the accumulation of such material in the hands of those who use it to cause harm.

1.2 Nuclear Safeguards and Security

Nuclear safeguards describe the technical measures used to verify the completeness of the declarations made by States about their nuclear material and activities. Nuclear security measures include "measures for the prevention and detection of, and response to, the theft of nuclear material, sabotage and other malicious acts" [4]. Programs and contingency plans deal with threats, theft, special nuclear materials, high level radioactive waste, nuclear facilities and other radioactive materials that the U.S. Nuclear Regulatory Commission (NRC) regulates [5].

SNM is the classification used by the NRC to categorize fissile materials which, in concentrated form, are the primary ingredients of a nuclear weapon. SNM is divided into three safeguard categories based on mass quantities and thus risk and potential for the direct use in a fissile explosive device. Category 1, or strategic SNM (SSNM) is defined as SNM in masses considered to be of greatest risk. Category II is SNM of moderate strategic significance or of mid-level risk and Category III is SNM of low strategic significance is of lowest risk. Table 1 details the specifics of the safeguard categories of SNM [6].

Table 1. SNM categories

Category	Name	Isotope	Mass (kg)
1	Strategic SNM (SSNM)	Plutonium	≥ 2
		Uranium-235 ($\geq 20\%$ enriched)	≥ 5
		Uranium-233	≥ 2
		$^{235}\text{U} + 2.5 (^{233}\text{U} + \text{Pu})$	≥ 5
2	SNM of moderate strategic significance	Plutonium	0.5 - 2
		Uranium-235 ($\geq 20\%$ enriched)	1 - 5
		Uranium-235 (10-20% enriched)	≥ 10
		Uranium-233	0.5 - 2
		$^{235}\text{U} + 2 (^{233}\text{U} + \text{Pu})$	≥ 1
3	SNM of low strategic significance	Plutonium	0.015 - 0.5
		Uranium-235 ($\geq 20\%$ enriched)	0.015 - 1
		Uranium-235 (10-20% enriched)	1 - 10
		Uranium-235 (natural-10% enriched)	≥ 10
		Uranium-233	0.015 - 0.5
		$^{235}\text{U} + ^{233}\text{U} + \text{Pu}$	≥ 0.015

1.3 Detection of Radioactive Materials

Radioactive materials can emit gamma rays, neutrons, and alpha and beta particles, depending on the source. This emitted radiation is characteristic of the source and thus, the radioactive source may be characterized by the proper identification of the emitted radiation. For an in-depth discussion of radiation detection principles and specifics of detectors beyond the scope of this dissertation, refer to [7]. There are two main approaches for the detection of SNM - they are classified as either passive assay or active detection.

1.3.1 Passive Assay Methods

Passive assay methods are based on the detection of naturally emitted radiations from SNM. The types and energies of these spontaneous emissions can be used as the isotope signatures and successful identification of this radiation allows for identification of the parent nuclei. While

passive detection methods are less invasive than active ones, not all radioactive materials have decay properties and emitted radiations that can be suitable for measurements, and thus would be hard to detect using the passive assay means. In addition, passive methods are often unsuitable for the detection of shielded SNM as the signatures from spontaneously decaying isotopes are often energetically weak, and can be easily masked by the shielding material. In these cases, it may be necessary to induce fission of the SNM and then detect and identify the more energetic radiations from the fission events that can penetrate the shielding.

1.3.2 Active Interrogation Methods

Active interrogation methods involve the use of a penetrating radiation probe (typically photon or neutron beams) to induce nuclear reactions within materials inside the container which otherwise would not occur spontaneously during the reasonable time of assay (fission will occur if SNM is present). Prompt gamma rays and neutrons are released in fission events as well as delayed neutrons and photons. Detection of these radiation signatures allows for identification of the original nucleus. Passive assay techniques are easier to deploy than active ones due to the absence of the probe radiation means.

The subsequent measurement of any such secondary radiations helps to identify the unknown contents within the container. Active assay techniques are generally viewed more favorable than passive techniques for a variety of reasons. While a passive assay system is used to detect radiation spontaneously emitted during nuclear transformations, active interrogations offer a unique flexibility. Different responses from different nuclides can be elicited by varying the type and the energy of the interrogating radiation probe. Further, active techniques can be used on the material of interest that is shielded with high-z and/or low-Z materials. Active interrogation

methods provide means for increasing the radiation emission to detectable levels (above those of the passive detection methods).

The interrogating radiation probe may be either a neutron source or photon source. On average, the induced fission reaction results in the production of two to three prompt neutrons (emitted at the time of the fission), and approximately eight γ -rays. For the next several minutes, the fission fragments continue to emit another 6-7 γ -rays and around 0.01 to 0.02 neutrons per fission that are called *delayed* gamma rays and neutrons (Figure 1). Both prompt and delayed fission radiations then can be detected and identified, leading to the determination of the parent nucleus.

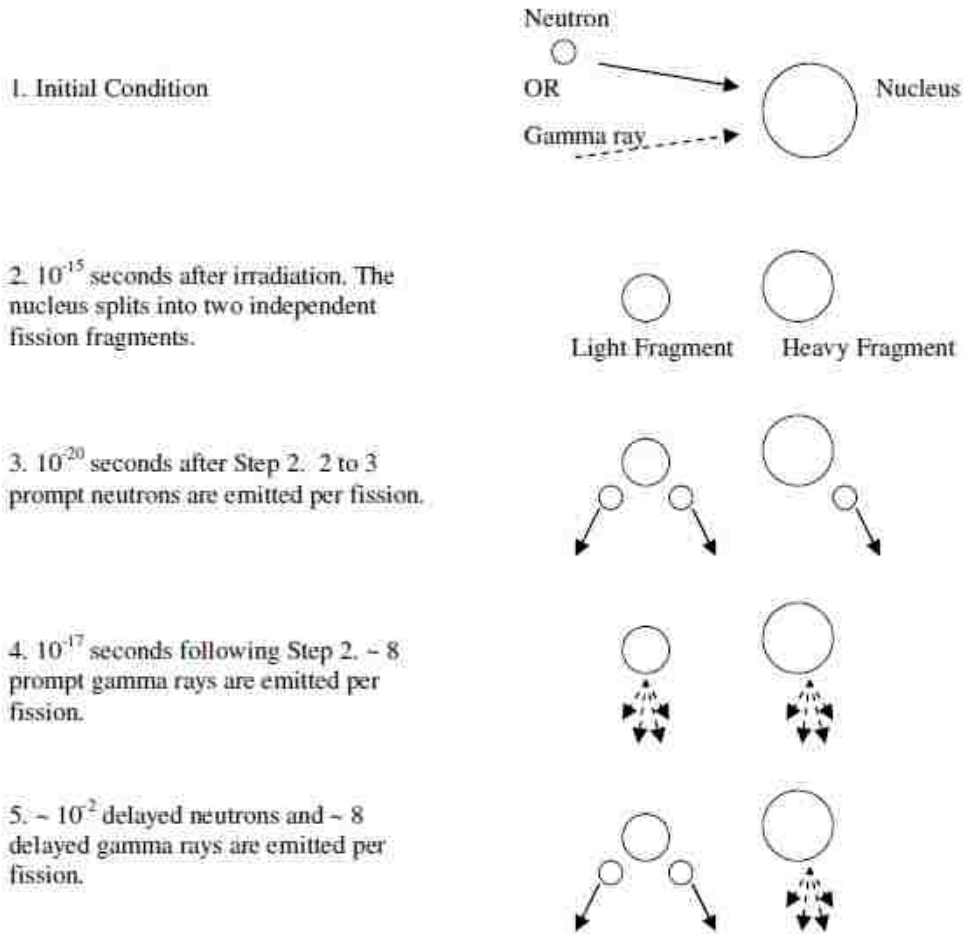


Figure 1. Fission process [8]

Despite the fact that the prompt radiation detection yields much higher counts per fission than the delayed radiation, many active assay techniques rely on the measurement of the delayed radiation. This is due to the problems arising from the need to distinguish between the interrogating probe's radiation and the emitted radiation that is induced by the probe. For example, the use of a neutron source as the radiation probe renders detection of prompt neutrons difficult as distinguishing between these neutrons is complicated. Similarly, it is difficult to detect emitted prompt photons if a photon probe is used. Adding to the difficulties is the fact that interrogating radiation can be scattered into the detector by shielding materials, the environment

or the SNM. For this reason, identification of the emitted radiation is done based on different energies of the interrogating and induced fission radiations. Coincidence counting may also be used to distinguish between the probe and induced fission radiations.

1.3.3 Review of the Current State of Nuclear Material Assay Systems

Both passive and active assay systems find use today, depending on the situation at hand. An example of a passive neutron detection technique involves the deployment of activation foils. When exposed to a neutron flux, the atoms in the foil undergo several nuclear reactions including, but not limited to (n,γ) , (n,α) , and (n,p) . When the atoms in the foil undergo one or more of these reactions, the nucleus excites, the atom becomes radioactive and the foil is said to be activated. In an attempt to de-excite, the radioactive nucleus often gives off a gamma ray. This gamma ray is unique to the daughter isotope from which it emitted and can be studied using the appropriate radiation detector. Gamma spectroscopy can then be used to determine the radioactivity of the foil.

Neutron activation is a non-destructive bulk analysis process often used to determine the elemental composition of a sample material. Neutron activation analysis (NAA) has seen widespread use across various disciplines, including African mineral dust transport studies [9], the determination of scandium and gold in meteorites [10] and understanding bullet fragment concentrations from the 1963 assassination of United States President John F. Kennedy [11, 12]. Neutron activation can also be used to understand the spatial distribution of neutron fluxes within a radiation environment by determining the radioactivity induced within dosimeters due to neutrons within the radiation field. Once the radioactivity of the foils has been determined, information about the neutron spectra that activated the foils can be obtained through use of gamma spectroscopy and spectrum unfolding methods. Activation foils have been used to

determine the neutron fluxes and for several different high energy linacs, including the 18 MeV Elekta Precise [13], the 18 MeV Varian Clinac DHX [14], the 18 MeV Siemens Oncor [15], and the 15 MeV Siemens Primus [16]. Activation foils have also been used to study neutron fluxes within the JET tokamak torus [17], the Test Blanket Module [18, 19], and the Tsin Hua Open-Pool Reactor [20] core.

Passive detection has also been used to characterize nuclear waste packages [21] in addition to being used for the detection of SNM. Radiation portal monitor (RPM) systems have been studied to detect hidden radioactive materials. Investigations involving the use of detector arrays consisting of polyvinyl toluene plastic scintillators for gamma ray and ^3He tubes for neutron detection were carried out [22]. It was determined that these detector arrays were suitable in detecting radiation from SNM, but the key issue was the successful managing of neutron background measurements.

The feasibility of integrating time correlation into RPM screening was investigated and it was found that source strengths could be determined even for slightly shielded materials [23]. A theoretical study for the detection of hidden SNM within storage containers using neutron activation foils for the purpose of treaty monitoring was performed and compared to experimental data. The results demonstrated that the foils weren't able to detect neutron flux at the specified sensitivity limit, but were able to detect if the sensitivity limits were reduced by a factor of 4 [24].

Passive detection and identification of gamma rays as an indicator of nuclear fuel burnup without any knowledge of initial enrichment or cooling time was studied using a new Mesh-Adaptive Direct Search (MADS) algorithm. It was found that the uncertainty space associated with the predicted values for enrichment, burnup or cooling time were narrowed [25].

In recent years, there have been investigations involving active interrogation techniques for the assay of containers with the possible presence of illicit materials. Several studies have investigated neutron interrogation for the discovery of conventional explosives [26, 27] as well as other hazardous materials (biological, chemical, explosives) [28].

In attempts to increase the amount of shipping containers that are scanned for SNM without slowing down the flow of commerce, Lawrence Livermore National Laboratory (LLNL) has developed technology that has been dubbed the "Nuclear Car Wash" [29-31]. Named for its resemblance to a typical automated car wash system, the nuclear car wash uses the interrogation probe (4 MeV collimated neutron beam) directed upwards into a shipping container as it rolls along a conveyor belt (Figure 2). Two large, flat arrays of detectors containing ^3He proportional counters flank both side sides of the conveyor belts and detect any delayed neutrons created from fission. Experiments using a stationary cargo in close proximity were successful in detecting 376 g of uranium despite being shielded by over 4 feet of steel. It was found that even for samples of low mass (5 kg), the research goals of low false probability ($< 0.1\%$) and high detection ($> 95\%$) were met. The study of the coincident detection of multiple prompt gamma rays following neutron interrogation of cargo containers was investigated [32-35] and met with favorable results.

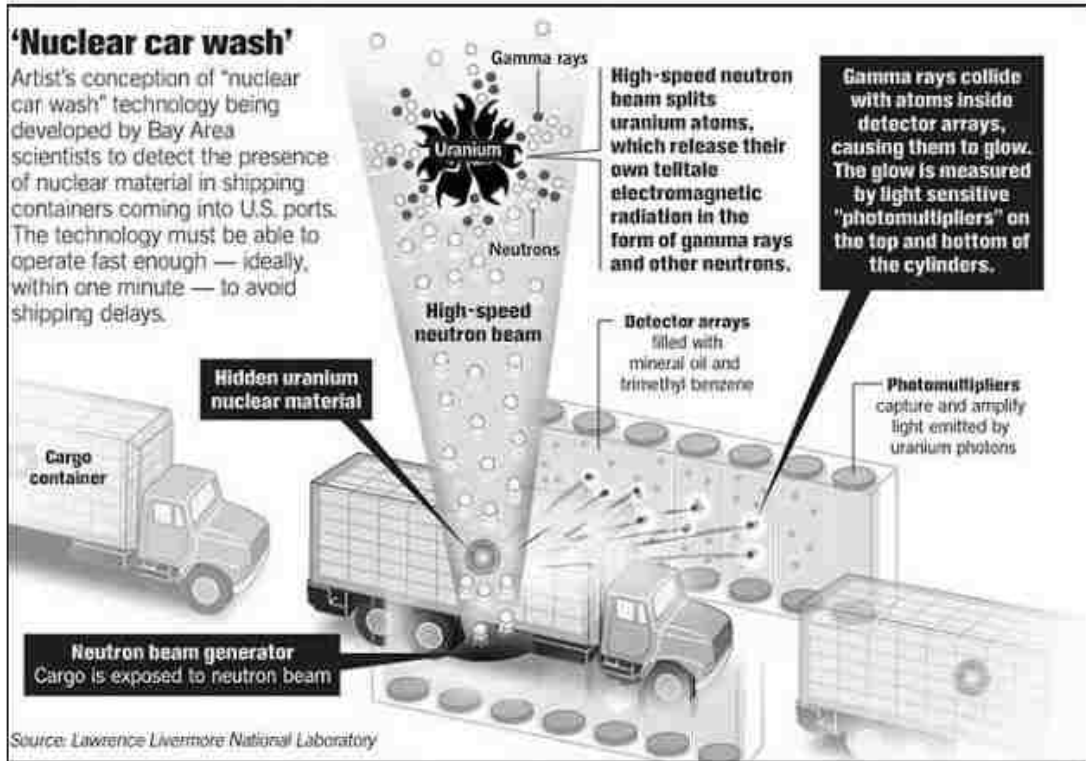


Figure 2. Nuclear car wash [36]

The Los Alamos National Laboratory's (LANL) Mobile Nondestructive Assay Laboratory (MONAL) was developed to measure materials contained in unpacked drums [37]. Originally used for examination of LANL transuranic waste (TRU) in the mid-1990s, new applications for its use have arisen including the use of active neutron assay. Refurbishments to a mobile, second generation LANL Mobile Passive/Active Neutron (M-PAN) system allow for production of an interrogating neutron probe (14 MeV neutrons, 2.5×10^{11} neutrons per second yield) through a deuterium-tritium (DT) neutron generator which can be used to detect and quantify SNM. The delayed neutrons are detected by the ^3He slab detectors. Normalization to reduce the effects of matrix material neutron moderation is performed by a fission counter. The large cavity size allows for samples of many sizes (up to 55 gal. drums) to be assayed. MONAL can also be used in a "passive" state, allowing for the counting of spontaneous fission neutron emissions. In

addition, MONAL possesses the capability to determine the number of emitted γ -rays from radioisotopes in waste packages.

The ^{235}U assay in small samples (0.1 - 10 g) is performed using the Van de Graaff accelerator [38]. In this system, the Van de Graaff accelerated protons into a ^7Li target producing a 3.75 MeV neutron probe that was used to irradiate samples with an operating cycle of 100 ms (35 ms irradiation, 25 ms delay, 40 ms counting, 10 sec delay). These neutrons provide deep penetration, resulting in fission produced neutrons which in turn are measured by a high efficiency slab of ^3He counters. To deal with larger sizes of fissile content (1 - 1000 g), medium and large size assay systems have been developed that use the Van de Graaff-based neutron source.

Developed to deal with the reliability problems experienced by Van de Graaff accelerators, a shuffler uses a ^{252}Cf spontaneous fission neutron source as an interrogating probe [38]. A ^{252}Cf source irradiates a sample for typically 1-10 seconds. The neutron source is then placed in a shield, and the delayed neutrons are counted by neutron detectors (polyethylene moderated ^3He gaseous detectors). The process is repeated until the desired counting statistics have been achieved. They are called “shufflers” due to the rapid motion of the source between the shield and beam. It is primarily used as an active interrogation source for 200 L drums. Shufflers are expensive due to the high cost of Cf sources and the required shielding. Cf shufflers provide the best potential accuracy for cans or drums thought to contain uranium bearing products greater than 1 mg. The delayed neutron signal is directly proportional to the Cf source strength and the background is low [39].

The differential die away technique (DDA) is used by waste generator sites in the U.S. and Europe to assay and characterize transuranic waste drums before disposal [40]. A 14 MeV neutron generator is used to interrogate the container. After each pulse, neutrons scatter,

thermalize (slow down to thermal energies) and induce fissions in the fissile material. An array of both bare and cadmium covered ^3He detectors surrounds the material and is used to detect the resulting fission induced neutrons. DDA systems can count both prompt neutrons (1-4 ms after fission) and delayed neutrons (5 ms after fission and onward). In addition, DDA systems are very sensitive: limits of detection for ^{235}U are between a few mg to 100s of mg in a 208 L drum. Lastly, despite the high passive neutron background; the intense interrogating beam ($\sim 10^8$ n/s) allows for active assay of remotely handled waste containers. The use of matrix material correction factors is needed to obtain measurement accuracy due to the high neutron moderation and absorption of the matrix material.

The combined thermal-epithermal neutron (CTEN) system uses ^4He detectors and substitutes graphite for the polyethylene chamber in an effort to detect both thermal and epithermal neutrons [40]. Epithermal neutrons are used to mitigate the effects of self-shielding in SNM (they penetrate further than thermal neutrons) and in some cases may even be able to detect self-shielding and provide a correction factor. Large waste boxes at the Y-12 Plant in Oak Ridge, TN are assayed using CTEN technology.

LANL researchers at the TRIDENT facility have recently demonstrated that neutrons can be generated by using a short-pulse laser [41]. An extremely short, intense laser pulse was focused onto an ultra-thin foil of deuterated plastic. Upon impact of the laser on the plastic, the deuterated particles are accelerated into a metal target located five millimeters beyond the foil. Neutrons are then produced by activation of the foil in a 30 degree angle cone. The TRIDENT experiment broke the previous world record for number of neutrons produced by a laser. Further experiment was successful in using these newly generated neutrons to detect and quantify the SNM inside an empty container. The results from the TRIDENT laser (while still preliminary)

provide an exciting opportunity for the development of small, portable, neutron probes with hopes that they can be used at border crossings and seaports.

Active and Passive Computed Tomography (A&PCT), developed by LLNL, uses gamma ray nondestructive assay (NDA) to identify and accurately quantify radioisotopes in closed waste containers, regardless of their classification type [42]. Two separate measurements are performed - the first being the photon interrogation of the waste container and the second being the passive measurement of the unknown radioactive source within the barrel. This method involves data acquisition, image reconstruction and gamma spectral analysis. The errors associated with traditional gamma measurements are related to unknown sources and non-uniform spatial measurements due to shielding material distributions. It was shown that these errors were reduced by the application of tomography based methods combined with active techniques.

1.4 Research Goals

The first objective of this research was to determine properties of the photon radiation probe based on the UNLV linear accelerator (linac). This linac (M6 model by Varian) produces photons with endpoint energy of 6 MeV. Computational models were developed using MCNP5 radiation transport code to study the operation of the M6. These models were used to determine the spectral distribution of photons as well as to compute dose rate contour maps of the accelerator facility during the linac operation. These models were validated through comparison with experimental measurements of photon dose rates. The feasibility of the M6 system to serve as a linac based source of photoneutrons was also studied. MCNPX was used to develop a computational model of the 15 MeV linac (K15 model by Varian). The K15 system was chosen

because it produces photons with the endpoint energy within the giant dipole resonance (GDR) region of nuclear materials, leading to a greater probability of inducing photofission in SNM targets. In addition, the probabilities of producing neutrons via the competing photonuclear reactions are low at 15 MeV. This allows for the interrogation of SNM with maximized number of neutrons produced through fission while minimizing the production of neutrons through competing reactions.

The second objective of the dissertation is to determine the radiation output from photon interrogated SNM targets of various compositions and different shielding matrices. The fluxes of neutrons and gamma rays produced by the photon irradiation of shielded SNM must be characterized before the appropriate detection technique can be designed.

The third objective is to determine a method of detection of the radiation output from interrogated SNM. During the photofission, both fast neutrons and photons are produced. Plastic scintillators have recently shown promise in replacing ^3He gas detectors as the "gold standard" in radiation detection as they are able to detect fast neutrons without a moderator and have a quicker response time than ^3He . For this study, the EJ-299-33A plastic scintillator was chosen due to its ability to discriminate between neutrons and photons. The array of such detectors allows to perform neutron coincidence measurements. Multiple detectors can be used to measure neutron multiplicity, helping to discriminate between fission neutrons and photoneutrons produced through (γ, xn) reactions. Photon and neutron sources (i.e. $^{239}\text{PuBe}$, ^{60}Co) at UNLV were used to test the detection of radiation emissions of fissioned SNM as they are capable of producing radiations in the same energy range, without construction of SNM systems.

1.5 Dissertation Outline

This dissertation consists of 7 chapters. Chapter 1 features the project introduction and research goals, with attention paid to the current state of the art. Chapter 2 details the relevant nuclear physics background. Linear electron accelerator fundamentals and the safety measures at the UNLV accelerator facility are presented in Chapter 3 while Chapter 4 discusses the characterization of the radiation emissions generated by the accelerators. Chapter 5 details results of the computational study of the active assay of SNM using the K15 linac. Chapter 6 presents the computational results of neutron coincidence simulations as well as experimental measurements. Chapter 7 concludes the dissertation and presents opportunities for future research.

Chapter 2: Background

2.1 Fundamentals of Nuclear Physics

The atom is the smallest unit of matter that retains properties of a chemical element. The subatomic particles within a non-ionized atom include the nucleus (composed of tightly bound nucleons - positively charged protons and neutrally charged neutrons) surrounded by an electron cloud with the number of electrons equal to that of the number of protons within the nucleus. The properties of these subatomic particles are shown in Table 2 [43].

Table 2. Subatomic particle data

Subatomic Particle	Mass (u)	Elementary Charge (C)
Proton	1.007276	1.60218E-19
Neutron	1.008665	0
Electron	0.00054858	-1.60218E-19

The atomic number, Z , of an element is equal to the number of protons in the nucleus. The mass number of an isotope, A , is equal to the sum of the number of protons, Z , and neutrons, N . Atoms with the same number of protons belong to the same chemical element. Atoms with the same number of protons but differing numbers of neutrons are called isotopes of the same element. An isotope is designated by its chemical symbol, X , along with its proton number, Z , and mass number, A : A_ZX . Isotopes behave similarly in chemical reactions (due to having the same number of electrons, which largely determines the chemical behavior), but may have different nuclear characteristics. A sample of an element often contains several isotopes with different atomic percentages. The percentage of an isotope in its natural occurring mixture is

known as its abundance. Enrichment describes an increase in an isotope's abundance by artificial means.

An atom is electrically neutral. As neutrons have no charge, the net charge of the tightly packed nucleus is positive. Similar charges repel each other; in a nucleus, the strong nuclear force overcomes the electrostatic repulsion between protons. This force holds the nucleus together and is attractive between the nucleons at distances of about 10^{-15} m (1 femtometer), repulsive at distances less than 1 fm, and decreases to zero at distances beyond the nuclear size [44]. The nuclear binding energy is the energy required to dissociate the nucleus of an atom into its components. An isotope that has sufficient binding energy to hold the nucleus together is referred to as stable. When the binding energy is not enough to hold the nucleus together, it becomes unstable. Unstable atoms release energy (or matter) in attempts to become stable. This process is known as radioactive decay. When material spontaneously emits radiation, it is classified as radioactive, and when isotopes are radioactive, they are considered radioisotopes. The nucleus that undergoes radioactive decay is known as the parent, while the nuclides remaining after radioactive decay occurs are known as daughter products.

The three most common types of radioactive decay process are alpha (α), beta (β), and gamma (γ) decays with a fourth, spontaneous fission, occurring much less frequently. Alpha decay occurs when an unstable nucleus ejects a helium-4 nucleus (2 protons and 2 neutrons), also known as an α -particle. Alpha radiation does not penetrate matter deeply and can be stopped by a piece of paper.

During beta decay, one of the protons in the nucleus is converted to a neutron (or vice versa) by the emission of either a positron (β^+) or electron (β^-), which are positively or negatively

charged particle of the electron mass. Beta radiation is slightly more penetrating than alpha radiation and can be stopped by wood or plastic.

Oftentimes during alpha or beta decay, the daughter nucleus is left in an excited state and must also release energy in order to transition into the ground state. This energy released is in the form of a photon (an electromagnetic wave) called a gamma ray due to its belonging to the gamma portion (wavelengths shorter than 10^{-11} m) of the electromagnetic spectrum Figure 3.

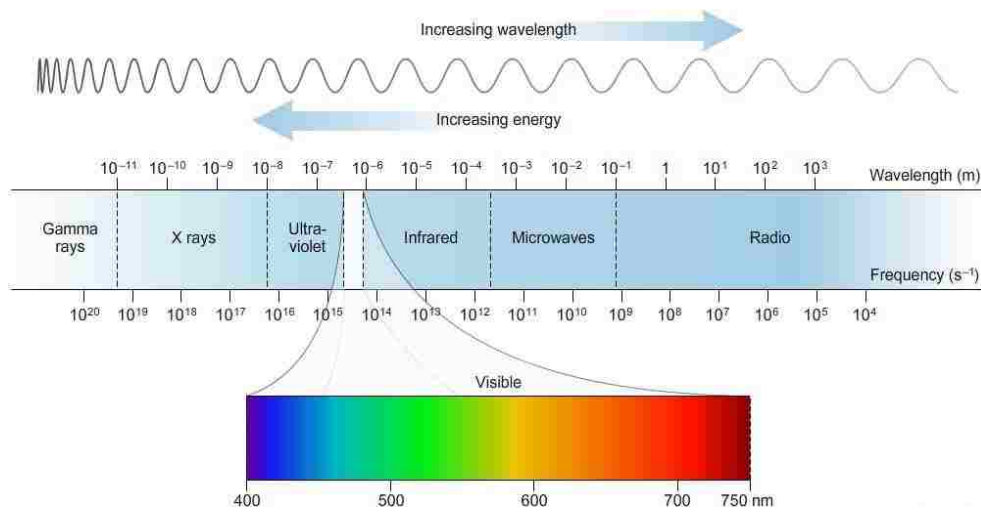


Figure 3. Electromagnetic spectrum [45]

X-rays are produced when orbital electrons transition within the atom or when electrons interact with a heavy metal target while gamma rays are produced in the nucleus transitions. Gamma rays are stopped by several feet of concrete or a few inches of lead.

Fission is the splitting of a heavy nucleus into two lighter fragments (known as fission products) along with the ejection of several high velocity neutrons and gamma rays. Neutrons that have been liberated from a nucleus are considered free neutrons and are classified according to their energies (Table 3).

Table 3. Neutron energy ranges [46]

Neutron Energy	Neutron Classification
0.0 - 0.025 eV	Cold
0.025 eV	Thermal
0.025 - 0.4 eV	Epithermal
0.4-0.6 eV	Cadmium
0.6 - 1.0 eV	EpiCadmium
1-10 eV	Slow
1 - 300 eV	Resonance
300 eV - 1 MeV	Intermediate
1 - 20 MeV	Fast
> 20 MeV	Ultrafast

Spontaneous fission only occurs in very heavy isotopes such as uranium, plutonium, and californium. Fission can be also induced when a nucleus (and thus considered a nuclear reaction and not radioactive decay) interacts with a neutron of sufficient energy. An isotope that is capable of undergoing fission spontaneously by the capturing of a thermal neutron is considered fissile, while isotopes that undergo fission by the incident neutrons are considered fissionable.

2.1.1 Nuclear Reactions

A nuclear reaction occurs when an incident particle of sufficient energy interacts with a parent nucleus, resulting in the creation of short-lived (up to 10^{-14} seconds) excited compound nucleus promptly followed by its decay, and ultimately the production of a daughter product and outgoing particle. Nuclear reactions are governed by the laws of the conservation of charge, nucleons, momentum, spin, and parity. Mass and energy are conserved, albeit through conversion of one to the other according to Einstein's mass-energy equivalence. Following a nuclear reaction, the rest mass of the product particles (daughter product and other emitted

products) may be different than that of the parent nucleus and incident particle. This difference in rest mass energies is known as the Q-value, and it is the energy required for the reaction to occur.

2.1.2 Types of Radiation

Radiation is classified as being either ionizing or non-ionizing, depending on how it interacts with matter. Non-ionizing radiation does not have sufficient energy to break molecular bonds or liberate (remove or displace) electrons from atoms in the matter with which it interacts. Examples of non-ionizing radiation include microwaves, heat, visible light and radio waves. In contrast, ionizing radiation has sufficient energy to break molecular bonds and liberate electrons when it passes through matter. The main types of ionizing radiation are alpha particles, beta particles, photons, and neutrons. Ionizing radiation has the potential to induce harmful effects in the living cells of plants and animals and for this reason, is considered more dangerous than non-ionizing radiation. For a complete discussion of the biological effects of ionizing radiation, please refer to [46].

2.2 Radiation Interactions with Matter

Different types of radiation interact with matter in different ways. The interaction methods of the radiation pertinent to this dissertation are discussed below.

2.2.1 Photon Interactions

Although gamma rays interact with matter in several ways; three processes - photoelectric effect, Compton effect, and pair production - are typically taken into consideration in nuclear engineering applications. The type of interaction that may occur depends upon the energy of the

gamma ray as well as the atomic number of the atom that the gamma ray is interacting with (Figure 4).

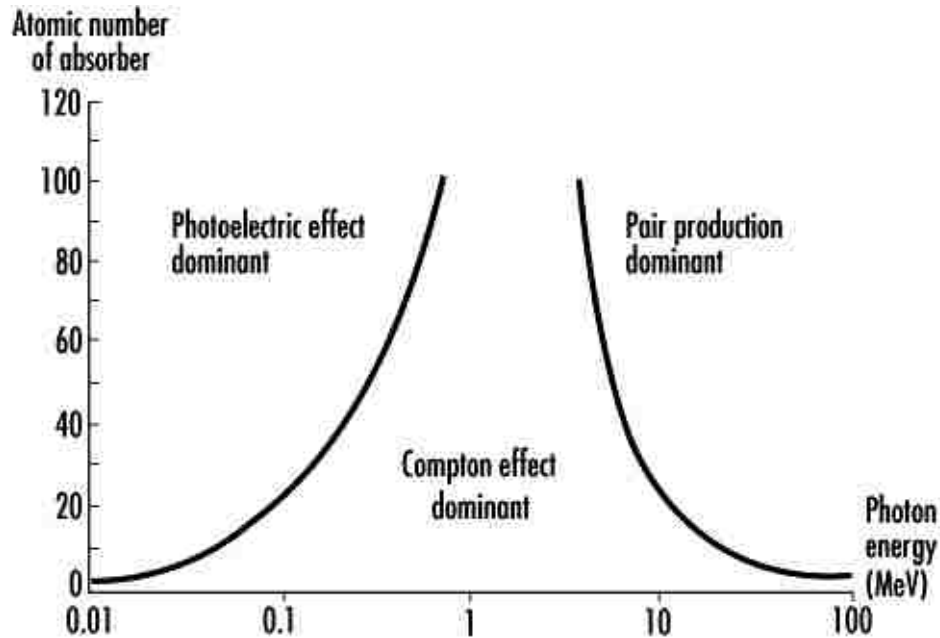


Figure 4. Photon interactions with matter [47]

The photoelectric effect describes the production of electrons by photon interactions with a material. If the incident energy of a gamma ray is greater than the electron binding energy of the atom it is interacting with, the photon will be completely absorbed within an atom, causing it to become unstable. The unstable atom releases energy through the emission of an electron. The photoelectric effect is the dominant mode of photon interaction at low photon energies.

The Compton effect (or scattering) describes the inelastic scattering (kinetic energy is not conserved) of a photon by an electron. Compton effect is the dominant mode of photon interaction with matter for mid energy photons. During the pair production, a photon is converted into an electron pair (positron and negatron, with a 1.022 MeV threshold). At high energy, pair production is the dominant mode of photon interaction with matter.

2.2.2 Neutron Interactions

Neutrons are electrically neutral and are not affected by the negative charge in the electron cloud or the positive charge in the nucleus. As a result, neutrons typically interact with matter by passing through the electron cloud and directly impacting the nucleus. Upon impacting the nucleus, there are several possible interactions that a neutron may experience, with the extent of each interaction being probabilistic in nature. When neutrons transport through matter, some neutrons may pass through the matter and not interact at all. The probability of a neutron interacting with matter through a specific event type is known as its cross section. The probability of a neutron interacting with matter depends on the energy of the neutron and the type of atom it is interacting with.

The major neutron interaction types are scattering (elastic and inelastic), radiative capture, and fission. Elastic scattering occurs when an incident neutron is absorbed by a nucleus, and another neutron is expelled by the nucleus, leaving the nucleus in its ground state. Inelastic scattering occurs when an incident neutron is absorbed by a nucleus, and a neutron is expelled by the nucleus, but the nucleus is left in an excited state. Radiative capture occurs when an incident neutron is absorbed by a nucleus, resulting in the emission of one or more gamma rays. Finally, fission occurs when a neutron induces the splitting of heavy nucleus. Cross sections for many isotopes of many chemical species have been determined.

2.2.3 Photoabsorption Reactions

If the incident particle in a nuclear reaction is a photon (either a gamma- or x-ray); the resulting reaction is known as a photoabsorption reaction. When a neutron is the emitted particle in a photoabsorption reaction, it is said to be a photoneutron. For a photoneutron to be produced, the energy of the incident photon must be larger than that of the neutron binding energy for a

specific nucleus. The Q-value represents the threshold energy that an incident photon must possess in order for photoneutron production to occur. A table of common binding energies (BE_n) for several typical photoneutron reactions is presented in

Table 4.

Table 4. Common Neutron Binding Energies [48]

Target Nucleus	m_{Target} (u)	Daughter Nucleus	m_{Daughter} (u)	BE_n (MeV)
^2H	2.01	^1H	1.01	2.22
^6Li	6.02	^5Li	5.01	5.67
^7Li	7.02	^6Li	6.02	7.25
^9Be	9.01	^8Be	8.01	1.66
^{12}C	12.00	^{12}C	11.01	18.72
^{16}O	15.99	^{15}O	15.00	15.66
^{23}Na	22.99	^{22}Na	21.99	12.42
^{24}Mg	23.99	^{23}Mg	22.99	16.53
^{27}Al	26.98	^{26}Al	25.99	13.06
^{28}Si	27.98	^{27}Si	26.99	17.18
^{40}Ar	39.96	^{39}Ar	38.96	9.87
^{40}Ca	39.96	^{39}Ca	38.97	15.63
^{55}Mn	54.94	^{54}Mn	53.94	10.23
^{56}Fe	55.94	^{55}Fe	54.94	11.20
^{63}Cu	62.93	^{63}Cu	61.93	10.86
^{184}W	183.95	^{183}W	182.95	7.41
^{235}U	235.04	^{234}U	234.04	5.30
^{238}U	238.05	^{237}U	237.05	6.15
^{239}Pu	239.05	^{238}Pu	238.05	5.65
^{232}Th	232.04	^{231}Th	231.04	6.44

The likelihood of a photon inducing a specific photonuclear reaction (either (γ,n) , (γ,a) , (γ,p)) is known as the cross section of that reaction type. Photofission (γ,f) is a nuclear reaction by

which a high energy photon is absorbed by a nucleus causing it to fission. The photofission cross section is the probability that a photofission reaction will occur. A larger cross section equates to a higher probability of the reaction occurring. The ENDF/B-VII.I cross sections for ^{239}Pu are shown in Figure 5. It is seen that photofission (γ, f) within ^{239}Pu will not occur if photon energies are less than 5.65 MeV. Whereas a 6 MeV linac produces photons with endpoint energy of 6 MeV, the majority of these photons have energies less than the 5.65 MeV photofission threshold of ^{239}Pu . Furthermore, the photofission cross section is lower at around 6 MeV than at higher energies. From Figure 5, it is seen that the (γ, f) cross section of ^{239}Pu sharply rises around 10 MeV and creates two peaks which eventually decrease around 16 MeV. The total photoabsorption ($\gamma, \text{absorption}$) cross section is the sum of the fission (γ, f) and all other photonuclear (γ, xn) cross sections. This energy range where the cross section is the highest is known as the giant dipole resonance (GDR) and is caused by the high frequency collective oscillation of protons against neutrons within the nucleus [44].

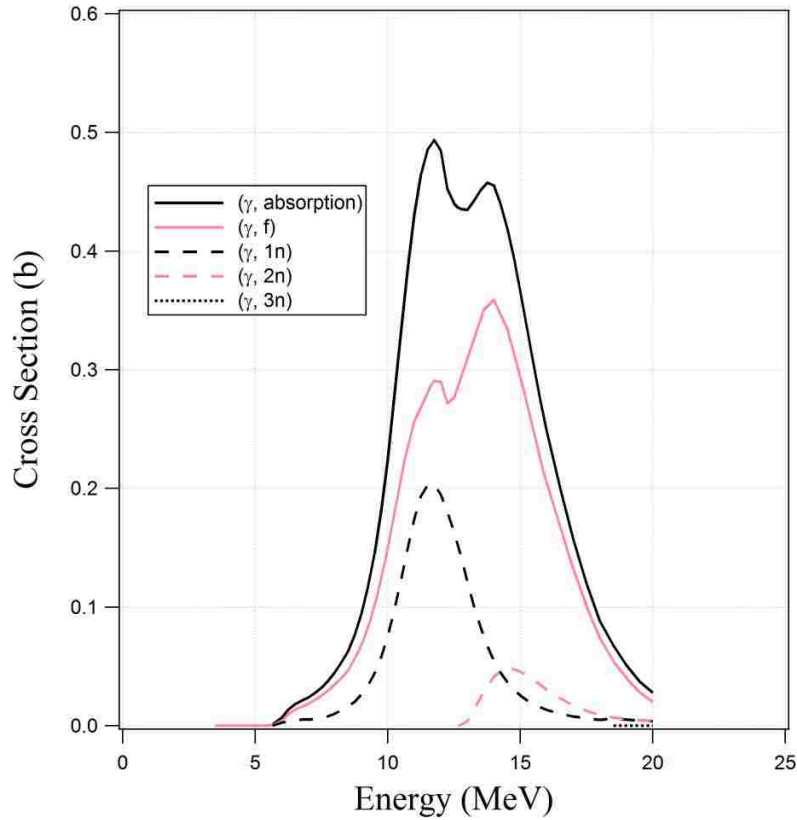


Figure 5. Photonuclear cross sections (ENDF/B-VII.1) of Pu-239 [49]

The K15 linac was chosen as the source for the photon probe because it produces photons with endpoint energy within the GDR region, leading to a greater probability of inducing photofission in SNM targets. In addition, the probabilities of producing neutrons via the competing photonuclear reactions (γ, xn) are low at 15 MeV. This allows for the interrogation of SNM with maximized neutron yield produced through fission while minimizing the production of neutrons through competing reactions.

Chapter 3: Computational Modeling of Electron Linear Accelerators

3.1 The Electron Linear Accelerator

The electron linear accelerator is a particle accelerator that uses electromagnetic forces to accelerate bunches of electrons to high electric potentials over a short distance. Within a few meters, it is possible for 10 keV electrons to be accelerated to up to 20 MeV [50]. Linacs have found use in a wide variety of applications including radiotherapy [51, 52], particle physics studies [53-55], medical isotope development [50,56] and cargo inspection [34-36, 57].

3.1. Production of Bremsstrahlung Photons

The accelerated electrons are bombarded onto a target composed of high-Z material to create bremsstrahlung photons. The incident electrons are deflected by the electron cloud of the atomic nuclei of the target material, losing kinetic energy in the process. This loss in kinetic energy is converted into bremsstrahlung (or *braking radiation*) photons (or x-rays).

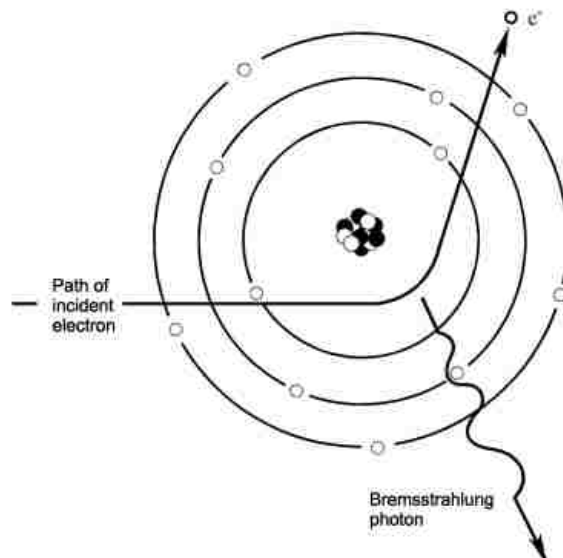


Figure 6. Production of bremsstrahlung photons [58]

The bremsstrahlung photons produced by a linac are characterized by their energy distribution, that is to say, by the quantity of photons produced at specific energies. Linacs produce bremsstrahlung photons which have an endpoint energy equal to the maximum energy of the electrons in the beam impinging on the target. In a 10 MeV linac, photons will have energies from 0 MeV up to 10 MeV. The number of photons passing through a defined area (commonly 1 cm²) is known as the photon flux. These photons are typically focused into a desired beam shape by the use of collimators. The beam of collimated photons is then used for a variety of applications including imaging, radiotherapy, the production of medical isotopes, or to perform an active assay on a sample on unknown material.

As discussed in section 2.2.1.4, if the energy of an incident photon is greater than that of the neutron binding energy of material it interacts with, a neutron can be produced through the (γ ,n) reaction. At energies greater than 10 MeV, the (γ ,n) reaction will take place within materials that commonly compose accelerator bunker structures [59].

3.2 Dose and Biological Dose Equivalent

To describe the effects of ionizing radiation on materials, it is necessary to quantify the amount of energy deposited by radiation when it interacts with matter. The term *dose* describes the amount of energy deposited by radiation within the material, while the term *biological dose* or *biological dose equivalent* describes the energy deposited in a living tissue. The biological dose equivalent is the dose multiplied by a quality factor used to express the biological damage variation between the different radiation types.

Table 5. Radiation quality factors [60]

Radiation Type	Quality Factor (Q)
Photons (x-rays, γ -rays) or β -particles	1
Neutrons of unknown energy	10
High-energy protons	10
α -particles, fission fragments, unknown charge heavy particles, multiple charged particles	20

The international system (SI) unit of dose is the *Gray* (Gy) and is equal to the absorption of 1 joule of energy by 1 kg of material. The *Rad* is equal to 1/100 Gy. The *Rem* is equal to the product of the *Rad* and the quality factor. The terms *dose rate* and *biological dose rate equivalent* are used to describe the respective doses received per unit time.

Once radiation fluxes in an environment have been characterized, the dose rates can be determined through the use of the energy-dependent flux-to-dose conversion factors for a specific radiation type. Several flux-to-dose conversion factors have been established (i.e. ANSI/ANS 6.1.1 1997, ICRP-21) but do not differ significantly above 0.7 MeV and maintain an accuracy of $\pm 20\%$ [61].

3.3 UNLV Accelerator Facility

The accelerator facility is located on the north end of the UNLV campus, between the Lied Athletic Complex and the Robert Miller Soccer Building. It houses a Varian M6 linac as well as having been prepared to host a K15 linac. The facility itself is built into a large earthen berm which envelops the facility on the east and northern walls (see Figure 6). The berm extends at least 5 m east and greater than 15 m north. An exclusion area is located atop the building to prevent roof access during linac operation. Both the earthen berm and exclusion area on the roof serve to minimize the radiation doses outside the facility, ensuring the dose rate stays below the

10 Code of Federal Regulation (CFR) 20 established guideline of 2 mrem/hr from external radiation in an unrestricted area [62].

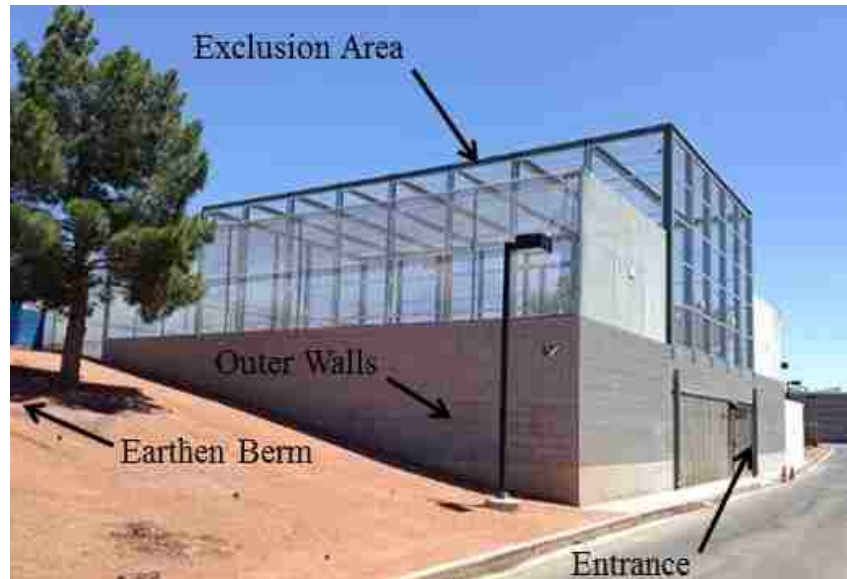


Figure 7. UNLV accelerator facility

The facility consists of an entry room, a shielding maze, and an accelerator bay. The control room is located south of the facility building itself, and is home to the operating controls of the linac as well as radiation detection equipment. The ceiling in the facility is 20 cm thick concrete, with the walls and floors being 15 cm thick, also composed of concrete. The entry room is a large open space that measures approximately 11 meters \times 10 meters. The shielding maze is formed by two walls of concrete bricks that serve to minimize the radiation doses in the entry way that are due to radiation emitted from the linac in the accelerator bay. The southern shield maze wall is 4 m long, 87 cm thick and the north wall is 7.5 m long and 117 cm thick. Both shielding walls are 2.5 m tall and extend almost completely to the ceiling (Figure 8).

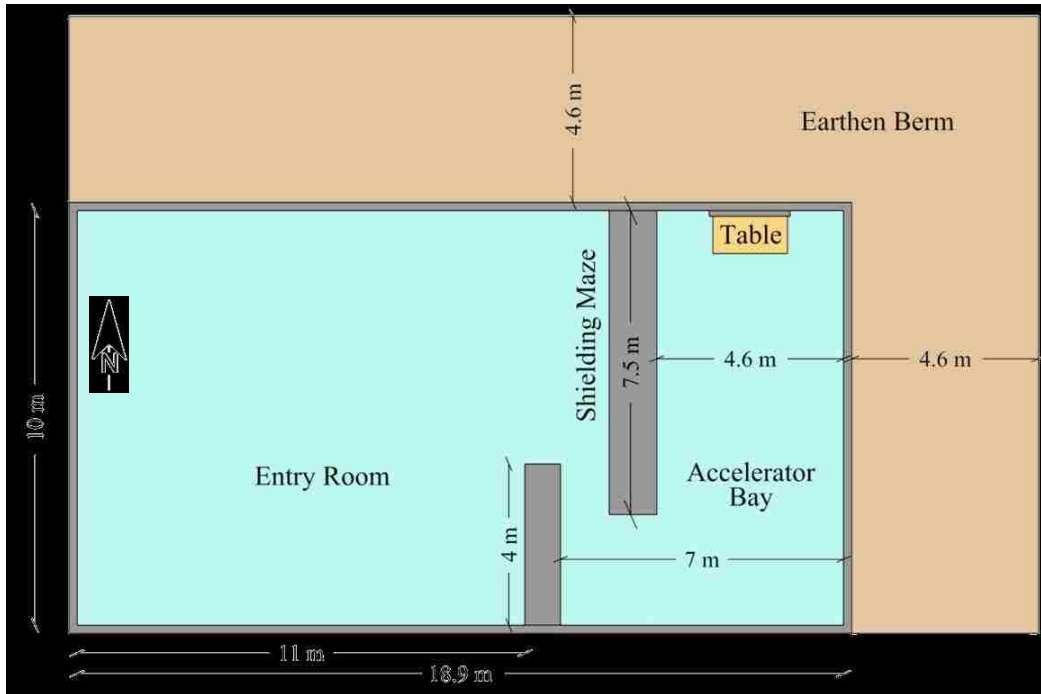


Figure 8. Accelerator facility layout

3.3.1 Varian M6 Linac

The Varian M6 linac [63] is used to produce bremsstrahlung x-rays with endpoint energy of 6 MeV (Figure 9). The M6 is approximately 106 cm long by 61 cm wide by 93 cm high and contains high-Z material shielding to minimize unwanted photon fluxes and dose rates outside the linac. The M6 system at UNLV contains collimator pieces designed to contour the emitted x-rays into a fan beam shape. In addition to the normal operation at 6 MeV, the M6 can be operated in the low energy mode as well. In this configuration, a 3 MeV incident electron beam is used to produce x-rays with an endpoint energy of 3 MeV.



Figure 9. Varian M6 linac [64]

The M6 linac is located approximately 3 m from the southern facility wall in the center of the accelerator bay (Figure 10). The bay is 4.6 m wide and a wooden table and concrete backstop sit approximately 5 meters north of the linac (Figure 11). The M6 linac rests on a table such that the collimated fan beam of the linac is at 1.2 m above the floor.



Figure 10. Varian M6 inside accelerator facility



Figure 11. Accelerator facility sample table

3.3.2 Varian K15 Linac

UNLV is in the process of receiving a Varian K15 linac [65], capable of producing high energy x-rays with an endpoint energy of 15 MeV (Figure 12). It can also be operated in a low energy mode, producing x-rays with endpoint energy of 9 MeV. It is primarily used for inspection and non-destructive testing.



Figure 12. Varian K15 linac [66]

A set of lead jaws placed directly behind the linac can be used to collimate the high energy photon beam. The geometry of the linac's core shields is such that the photon beam without collimation resembles a cone. The K15 will be placed sit on a stationary cart in the accelerator bay such that the height at the center of the conic photon beam is 43.75 inches above the ground. The cart will be placed in approximately the same location as where the M6 is located.

3.4 Computational Modeling of the Linacs

Computational modeling is used to study the behavior of complex systems using computer science, math and physics. Models typically use numerous variables that characterize the system being studied. Simulation is performed by the adjustment of these variables and the subsequent observation of the outcome of the system [67]. Computational modeling is often used as a first step in providing an estimation of parameters for a proposed experiment. When possible, model results should be validated against experimental measurement in order to determine the accuracy of simulations. Computational modeling is a valuable tool that allows for studying the effects of changing experimental parameters prior actually performing these experiments.

3.4.1 Monte Carlo Methods

The Monte Carlo methods form a broad class of stochastic algorithms that proved successful in a variety of disciplines including genetics [68,69], fluid dynamics [70,71] and economics [72,73]. While problems might be solvable through deterministic methods, Monte Carlo methods use repetition of random sampling to arrive at a numerical result. With respect to nuclear science and radiation transport, Monte Carlo codes are used to track particle interactions with matter through their lifetimes over a wide range of energies. The computational models in this study

used the Monte Carlo technique and were created using the general purpose Monte Carlo N-Particle Transport (MCNP) software suite developed and maintained by LANL.

3.4.1.1 MCNP software suite

MCNP codes are used for 3-D radiation transport of any combination of over 40 particles (i.e. neutrons, photons, electrons, etc.). The suite consists of three codes - MCNP5 [74], MCNP6 [75], and MCNPX [61]. MCNP5 was the original software produced and designed to handle arbitrary three-dimensional radiation transport code. MCNPX has several features and updates not present in MCNP5, including the ability to simulate photonuclear interactions with the appropriate photonuclear cross section libraries. MCNP6 was created to merge MCNP5 and MCNPX codes. Additionally, MCNP6 has features not found in either MCNP5 or MCNPX, including the ability to import unstructured mesh geometries from the finite element code Abaqus and to handle photon transport at low energies (1.0 eV) [75]. All MCNP codes use evaluated cross section data to determine particle interactions with matter based on a user created input file. MCNP calculations simulate individual particle reactions with matter, from birth until death (i.e. loss of kinetic energy or leaving the simulation boundary). These reactions are determined according to the energy of the incident particle and the reaction cross section of the specific matter with which it is interacting. Once an MCNP simulation has been completed, an output file is generated from whence the results can be analyzed.

Chapter 4: Characterization of Radiation Generated by a Linac

The UNLV accelerator facility was modeled using MCNP codes in an effort to characterize the radiation environment during by the operation of the Varian linacs. To accurately determine the dose rates within the facility, it was necessary to properly characterize the bremsstrahlung photons generated by the linac in addition to simulating the photon interactions within the building environment.

4.1 Accelerator Facility Dose Rate Modeling

It is important to understand the radiation yields produced during linac operation and how that radiation is transported throughout the building in order to determine location specific doses. Understanding the location specific dose rates within the building allow for verification of building safety measures, as well as help to understand expected dose rates at different distances from the linac structure which is vital concerning future research projects which may involve the irradiation of different sample materials.

MCNP software has been used to perform computational studies for the determination of photon fluxes produced by several medical linacs including the Varian 2300 [76,77], the Varian 2100 [78,79], and a few Phillips models [80-82]. Computational studies involving the undesired production of photoneutrons in high energy linacs have been performed for incident electron energies of 10 MeV [83], 14 MeV [84], 15 MeV [85,86], 18 MeV [87,88], and 25 MeV [89]. Additionally, the determination of dose rates within radiation therapy rooms have been studied for several different facilities [90-93].

The geometry of the accelerator facility was modeled in 3-D according to the previously discussed building dimensions. The material compositions of the internal facility structures were taken from *Compendium of material composition data for radiation transport modeling* [94] and the ENDF/B-VII cross sections (denoted by the “.70c” identifier in MCNP5) at room temperature were used. The M6 linac and K15 linac were modeled using different MCNP codes. The M6 model was run using MCNP5 while the K15 model used MCNPX. The M6 model could also be run in MCNPX, but the K15 model could not be run in MCNP5 due to its lacking of photonuclear physics and the proper cross section library.

4.1.1 Accelerator Facility Layout

The accelerator facility structures were modeled the same for all calculations regardless of which linac (M6 and K15) was being studied. The only difference between the two models was the representation of the linacs themselves. In order to ensure the proper characterization of the radiation environment within the facility, the linac target button and shielding materials within each linac were modeled according to Varian proprietary drawings.

4.1.2 Radiation Source Term

In order for a computational model to produce precise results, it is necessary to accurately describe the source term. The source definition (SDEF) card is used to define the particle transport required within the MCNP model. The M6 and K15 computational models start with the simulation of an electron beam impinging upon the linac target head. The target head geometries and comprising material differ between the two linacs, and were each modeled according to Varian proprietary designs. An example of the MCNP5 code used to define the electron source term is shown in Figure 13.

```

c ----- Source Definition -----
sdef x d1 y 0 z d2 erg=d3 par 3 vec 0 1 0 dir 1
sp1 -41 0.065 0
sp2 -41 0.065 0
sp3 -4 0.120 6
c -----

```

Figure 13. Source term for M6 linac model

The "mode p e" card was used to include photon and electron transport in the model. The default "phys:p" card was used to include the production of bremsstrahlung by electrons. The source was defined to be a 1.3 mm electron pencil beam traveling in the y-direction. The x- and z-directions of the source term location followed distributions 1 ("d1") and 2 ("d2") to use a built-in Gaussian probability (denoted by -41) for spatial coordinates extending 0.65 mm in both directions. The "erg" card specified the energy of the source term using distribution 3 ("d3") to set a Gaussian fusion spectrum centered around 6 MeV. The "par" card was set to 3 to specify an electron source and the "vec" and "dir" cards were set to <0 1 0> and 1 respectively, to specify the direction of travel of the electron beam (along the y-axis). The source term was checked to ensure the Gaussian nature of both the spatial coordinates (Figure 14) and energy values (Figure 15).

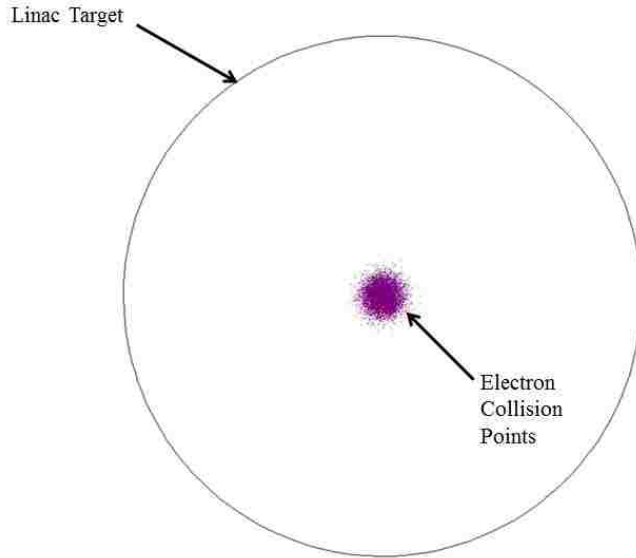


Figure 14. Gaussian spatial distribution of electrons on M6 target

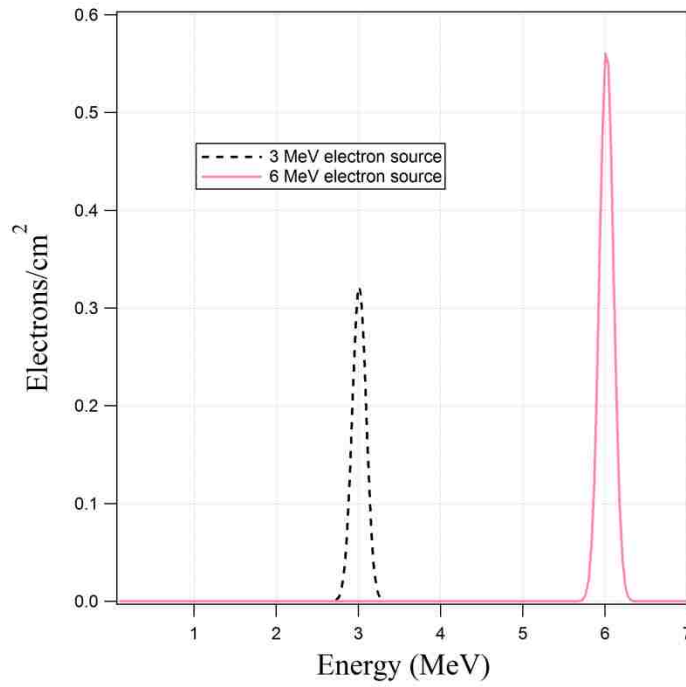


Figure 15. Gaussian energy distribution of incident electrons on M6 target

The K15 source term was defined similarly, except neutrons were be added to the "mode" card and the average energy in the sp3 line was changed from 6 to 15 MeV. The "phys:P" card default values must be modified to account for photonuclear production in the model. The *ispn* value (4th entry) on the "phys:p" card must be changed from 0 (default) to either -1 (analog photonuclear particle production) or 1 (biased photonuclear particle production). Additionally, the *fism* value (7th entry) of the phys:p card was set to 1 to enable the LLNL fission model (as opposed to the default ACE model). The LLNL model was chosen as the ACE model does not account for prompt photofission gamma rays [95].

4.1.3 Flux Tallies and Dose Rate Conversions

To evaluate the source term for the bremsstrahlung photons produced within the respective linac target heads, it was necessary to determine their angular distribution and energy spectra. Thin (0.01 cm), concentric ring surfaces were placed 1 cm behind the linac target head. F4 tallies (track length estimate of the cell flux) were placed within each ring surface allowing for the determination of the x-ray flux at 10 degree increments off centerline (Figure 16). Two hundred equally spaced energy bins were used at each tally in order to determine the energy distribution of the x-ray spectra. The relative error associated with each bin in an MCNP tally (corresponding to one standard deviation) is given by the inverse square root of the number of source particles contributing to that tally. The MCNP suggestion for tally result reliability is below 10% error for F4 tallies.

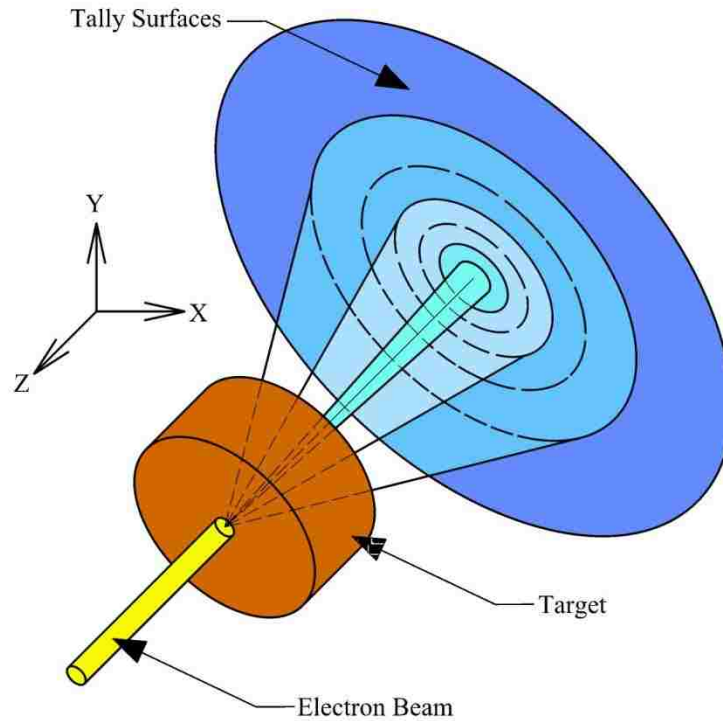


Figure 16. Bremsstrahlung angular distribution

A mesh tally was used to determine the x-ray fluxes and dose rates due to operation of the M6 within the accelerator facility at the height of the fan beam (1.2 meters above the floor). The FMESH card was used to determine the photon fluxes at 7.54 cm (3 inches) intervals in the x- and y-directions throughout the building. The dose energy (DE) and dose function (DF) cards were used to convert the computed photon fluxes into dose rates by using the ANSI/ANS 6.1.1-1977 photon flux-to-dose rate conversion factor [96]. In addition to the FMESH tally, F5 tallies (flux estimators at a point) surrounded by *dextran* spheres were used to determine the dose rates at specific points within the facility for M6 operation. These points are represented by the yellow and red dots in Figure 17. Additionally, the red dot indicates where the dose rate was measured by an ion chamber intrinsic to the M6.

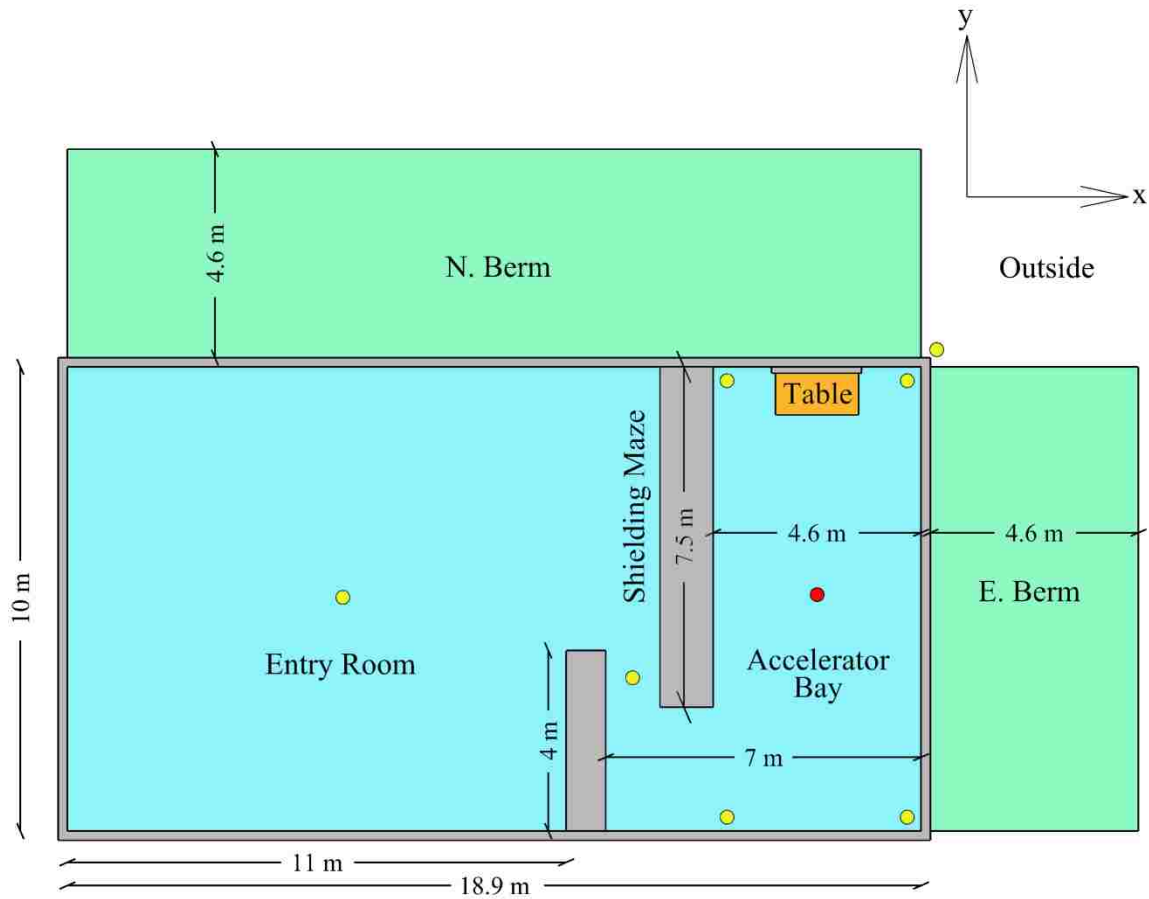


Figure 17. F5 tally locations, M6 characterization

A mesh tally was similarly used to determine the photon and neutron dose rates within the accelerator facility for operation of the K15, but the mesh tally syntax used in MCNPX differs from that used in MCNP5. In MCNPX, the TMESH tally with RMESH (denoting a rectangular mesh) was used to determine the dose rates throughout the building at the same spatial intervals as used with the M6. Additionally, in MCNPX, the DE and DF cards were not needed as the dose rate conversions are handled within the RMESH by using the keyword DOSE and specifying the *ic* value to be 20 (corresponding to the ANSI/ANS 6.1.1-1977 flux to dose factors) for both photons and neutrons.

4.1.4 Particle History

In this study, the "NPS" card was used to set the particle history cutoff and establish when MCNP models would complete their runs. Once the number of simulated particles lifetimes exceeds the number specified by the NPS card, the MCNP model stops running and generates an output file, from which the results can be analyzed. Some models can take several days or weeks to complete depending on the intricacies of the model physics, the NPS cut off value, and the type and energy of particles used in the simulation.

Charged particles (i.e. electrons) have large numbers of interactions due to long-range Coulomb forces whereas neutral particle interactions are defined by infrequent isolated collisions. As such, simulations involving charged particle transport take longer to complete than those without charge. For example, an electron slowing down (from 0.5 MeV to 0.0625 MeV) in aluminum will experience 10^5 interactions whereas a photon will experience less than 10 [97].

4.1.5 Determination of the Electron Current on the Linac Targets

MCNP tally results are normalized per starting particle. As the MCNP linac models in this study began with the simulation of electron transport, it was necessary to determine the actual number of electrons per second in order to acquire quantifiable values for photon flux and dose rates. The M6 and K15 linacs use pulsed electron bunches to produce bremsstrahlung. As the electron current is not constant, it is required to determine the DC averaged current for each linac.

The voltage of a single pulse of the electron beam on the M6 linac target head was measured using a Teledyne Lecroy oscilloscope (Figure 18). The single pulse voltage was converted to single pulse current (Figure 19) by dividing by the resistance (50Ω), determining the total area

under the curve and multiplying by the frequency (156.555 Hz) to obtain a total DC averaged electron current of 3.4×10^{14} electrons per second.



Figure 18. M6 electron voltage, single pulse

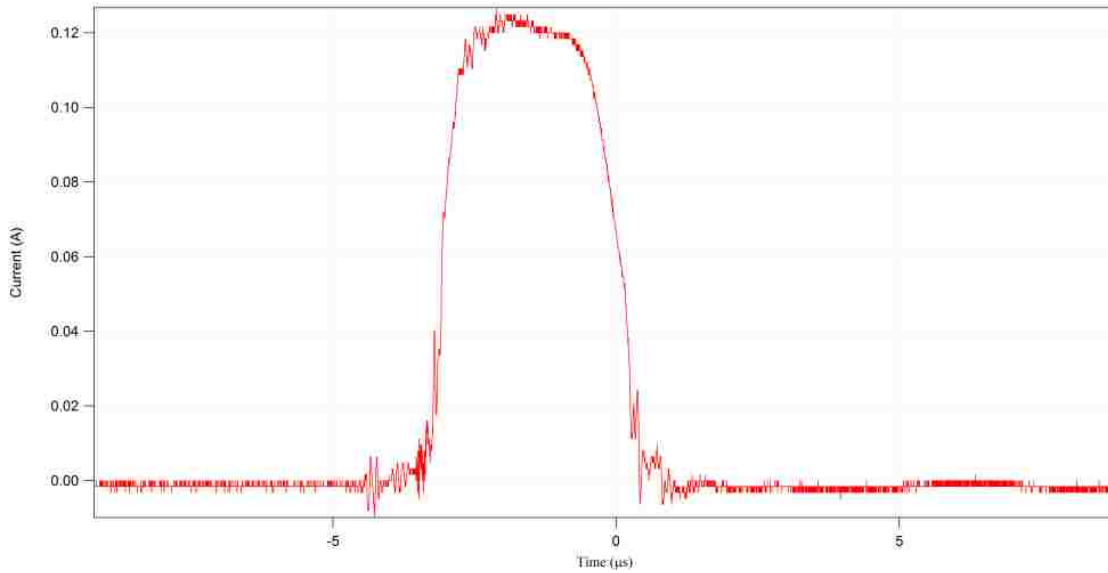


Figure 19. M6 electron current, single pulse

The K15 electron current was determined according to the following

$$Electron\ Current = \frac{Current\ Voltage}{Current\ Resistance} * Pulse\ Width * Rep\ Rate$$

Proprietary values for each parameter were acquired from Varian Medical Systems with the final currents being 7.14×10^{14} , and 6.73×10^{14} electrons per second, for K15 operation in 9 MeV and 15 MeV, respectively.

4.2 Facility Dose Rates - Results

4.2.1.1 M6 Bremsstrahlung Characterization

The spectra of bremsstrahlung x-rays flux within the M6 were determined for low (3 MeV) and high (6 MeV) energy operation modes with the results shown in Figure 20 and Figure 21. The largest photon fluxes occur within 10 degrees of the center of the linac target and decrease with increasing the angle. The trend of decreasing flux with increasing energy is apparent in both of the computed spectra. There is typically an order of magnitude difference between the fluxes at each angular interval between the two M6 operation modes. This is due to the greater likelihood that higher energy electrons will produce bremsstrahlung radiation with higher energy within the linac target. The error associated within each energy bin in the bremsstrahlung spectra results are less than the MCNP recommended value of 10% for F4 tallies.

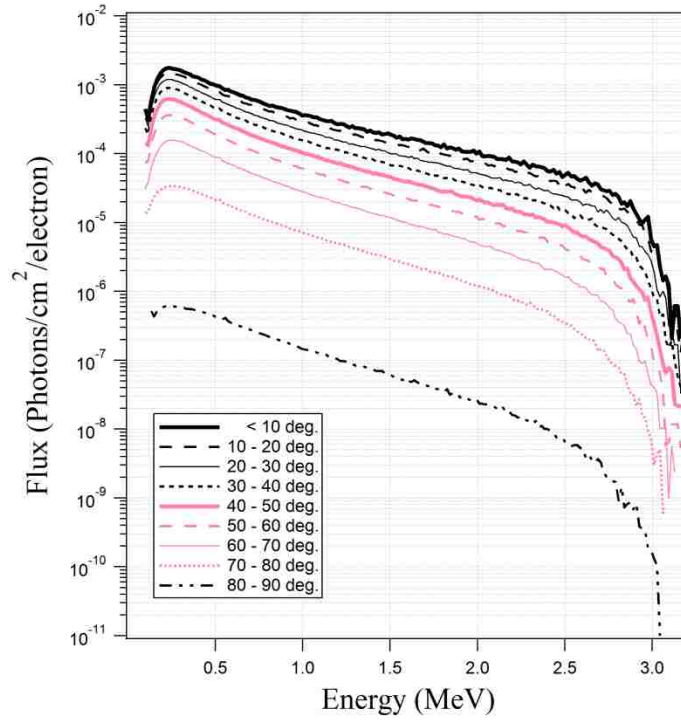


Figure 20. M6 bremsstrahlung spectra for 3 MeV incident electrons

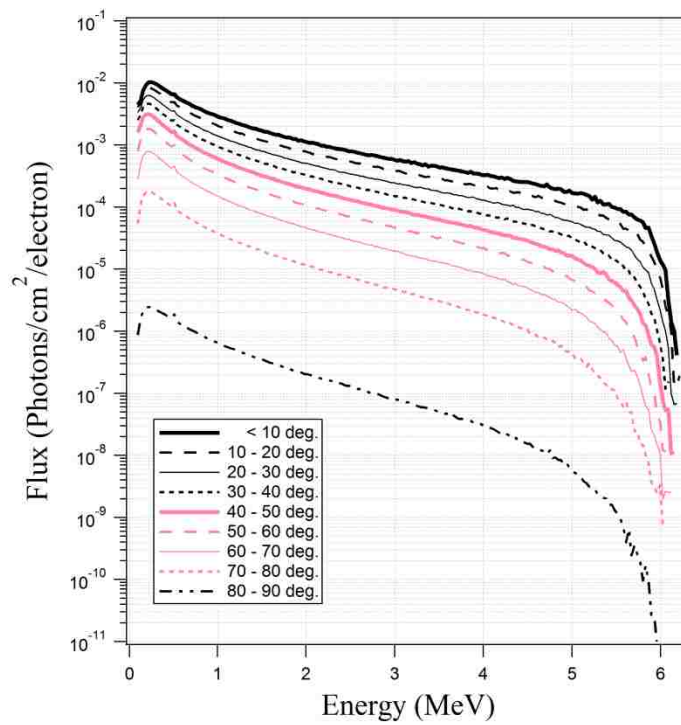


Figure 21. M6 bremsstrahlung spectra for 6 MeV incident electrons

The radial variation of the photon flux within a conical segment of 35 degrees was tested. Thin cylindrical surfaces were placed radially at 30 degree intervals throughout the conic segment. F4 tallies were placed on each of these surfaces with the results showing that the flux at each radial location had similar spectral distribution (Figure 22). The x-ray source was thus concluded to exhibit radial symmetry within each conic segment.

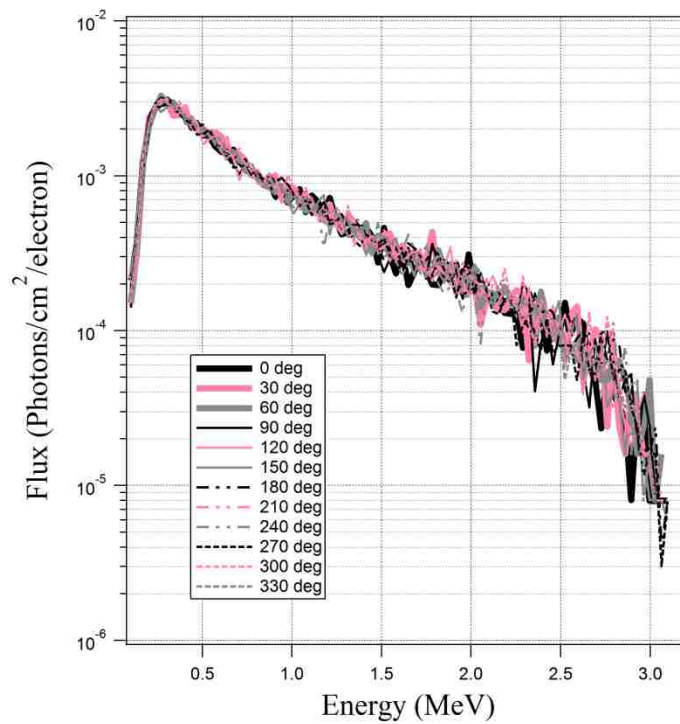


Figure 22. Radial fluxes, 35 degree conical segment

As the computational results are normalized to one starting particle (electron), they must be multiplied by the actual number of particles (described previously in 4.1.5) in order to evaluate the photon flux.

4.2.1.2 Electron Energy Cutoff

The MCNP5 models used to determine the M6 photon spectra were run using an NPS value of 1×10^8 starting electrons in order to minimize the error in each energy bin. Difficulty exists in determining the proper balance between minimizing computational time while maintaining satisfactory results. In order to reduce the computational time associated with the research in this study, the suitability of using energy cutoff cards was investigated. Care must be taken when using energy cutoff cards as their use modifies the underlying model physics, resulting in the halting of particle interactions occurring under this energy threshold. In some instances, this may remove certain reactions from happening in the model or may modify results incorrectly beyond that which was originally determined. Results obtained from models using energy cutoffs should be compared against those without using energy cutoffs in order to make an accurate assessment as to whether their use is acceptable. The M6 bremsstrahlung spectra was determined using electron energy cutoffs of 0.001 (default), 0.01, 0.1 and 1.0 MeV with an NPS of 1×10^7 electrons. The results of the photon fluxes using the default and 1.0 MeV energy cutoffs for the first four energy bins are shown in Table 6.

Table 6. Photon flux results, electron energy cutoff study

	E (MeV)	< 10 deg.	10-20 deg.	20-30 deg.	30-40 deg.	40-50 deg.	50-60 deg.	60-70 deg.	70-80 deg.	80-90 deg.
default	0.1	4.47E-03	4.11E-03	3.39E-03	2.52E-03	1.59E-03	7.91E-04	2.76E-04	5.31E-05	8.56E-07
cut-off	0.1	3.58E-03	3.28E-03	2.68E-03	1.97E-03	1.24E-03	6.00E-04	2.02E-04	3.70E-05	6.24E-07
default	0.16337	1.29E-02	1.12E-02	9.29E-03	7.04E-03	4.87E-03	2.75E-03	1.15E-03	2.57E-04	3.58E-06
cut-off	0.16337	1.14E-02	9.99E-03	8.17E-03	6.22E-03	4.17E-03	2.34E-03	9.64E-04	2.13E-04	2.95E-06
default	0.22673	2.00E-02	1.60E-02	1.24E-02	9.29E-03	6.25E-03	3.65E-03	1.56E-03	3.48E-04	4.70E-06
cut-off	0.22673	1.88E-02	1.51E-02	1.17E-02	8.50E-03	5.66E-03	3.25E-03	1.40E-03	3.07E-04	4.12E-06
default	0.2901	2.05E-02	1.59E-02	1.18E-02	8.56E-03	5.78E-03	3.35E-03	1.48E-03	3.37E-04	4.53E-06
cut-off	0.2901	2.00E-02	1.51E-02	1.13E-02	8.07E-03	5.35E-03	3.10E-03	1.35E-03	3.05E-04	4.07E-06

The percent similarity between the results of the two models for each bin were determined by dividing the results from the models using a cutoff energy by those obtained without using a cutoff energy (Table 7). The percent similarity between the two flux values helped to understand how much the results varied when the MCNP5 model terminated individual electrons at the energy cutoff of 1.0 MeV.

Table 7. Flux value similarity percentage

E (MeV)	< 10 deg.	10-20 deg.	20-30 deg.	30-40 deg.	40-50 deg.	50-60 deg.	60-70 deg.	70-80 deg.	80-90 deg.
0.1	80.21%	79.86%	79.19%	78.18%	77.88%	75.87%	73.23%	69.55%	72.94%
0.16337	88.63%	89.25%	87.91%	88.24%	85.72%	85.34%	84.05%	83.02%	82.39%
0.22673	93.68%	93.84%	94.20%	91.43%	90.44%	88.87%	89.98%	88.11%	87.57%
0.2901	97.27%	95.32%	95.21%	94.26%	92.61%	92.55%	91.16%	90.48%	89.77%

The results showed that using an electron cutoff energy of 1.0 MeV in the MCNP5 model resulted in photon flux values of above 70% similarity to the original results at all angle intervals within the first energy bin (below 0.1 MeV). In the second bin (between 0.1 and 0.16337 MeV), the average similarity rose to around 85% and by the third bin 90%. Above the third bin, average similarities between the two models rose to 95%. It was found that as the energy increased, so too did the similarity between model results for photon fluxes. Above the 1.0 MeV electron cutoff energy, the photon fluxes were identical. The computational time requirement (rounded to the nearest minute) for running the MCNP5 model with each energy cutoff is shown in Table 8.

Table 8. Time savings using electron cutoff energies

Energy Cutoff (MeV)	0.001 (default)	0.01	0.1	1
Simulation Time (min)	8876	866	134	43

Using an electron energy cutoff of 1.0 MeV reduces the time required to complete the MCNP5 model by 99.5%. The only photon flux results that are affected by this cutoff are those below 1.0 MeV and of those results, fluxes above 0.22 MeV are approximately 90% of the original value. The time savings combined with the percent similarity between results due to energy cutoff usage lead to the conclusion that using an electron cutoff energy of 1.0 is justified for this study.

4.2.2 Radiation Environment During Operation of the M6

While it is important to understand the dose rates within the facility due to operation of the M6 linac under normal operating conditions, it is also important to understand the dose rates for

other possible scenarios. As future research activities may require M6 usage without the fan beam collimators, it is necessary to evaluate the dose rates within the building under such operating conditions. Further, an understanding of the maximum dose rates achievable due to the M6 operation helps to characterize safety features within the building as well as judge the effectiveness of the linac shielding (Table 9).

Table 9. Linac configuration data

M6 Linac Configuration	Conditions	Collimators	Shielding
1	Normal Operation	Yes	Yes
2	Without Collimators	No	Yes
3	Maximum Dose Rate	No	No

For each linac operating configuration, the FMESH tally was used to determine the overall dose rate footprint while F5 tallies were used to determine the dose rates at specific building locations. Comparison of the specific dose rates under differing M6 configurations allowed for determination of the effectiveness of collimator pieces and linac shielding in reducing dose rates throughout the building. The MCNP5 models do not incorporate the earthen berm to the north east of the facility. This allows for studying the shielding effectiveness of the concrete wall alone. In actuality, the earthen berm completely envelops the northern, northeastern and eastern walls of the facility.

4.2.2.1 M6 Configuration 1

The M6 normal operation mode includes the use of tungsten collimator pieces to shape the emitted x-ray photons into a horizontal fan beam at a height of 1.2 meters above the floor. Lead shielding exists within the linac assembly to minimize dose rates to the sides and rear. The

computed dose rates due to M6 operation under normal configuration, in both high and low energy mode are shown in Figure 23 and Figure 24.

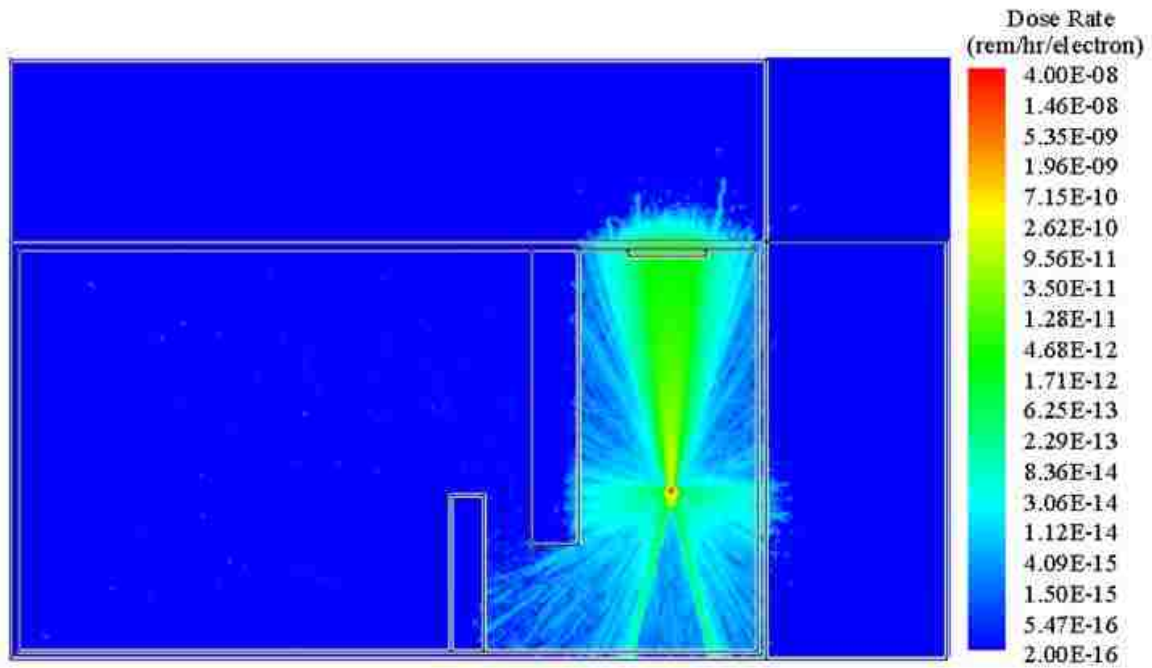


Figure 23. M6 Configuration 1 dose rates, 6 MeV electrons

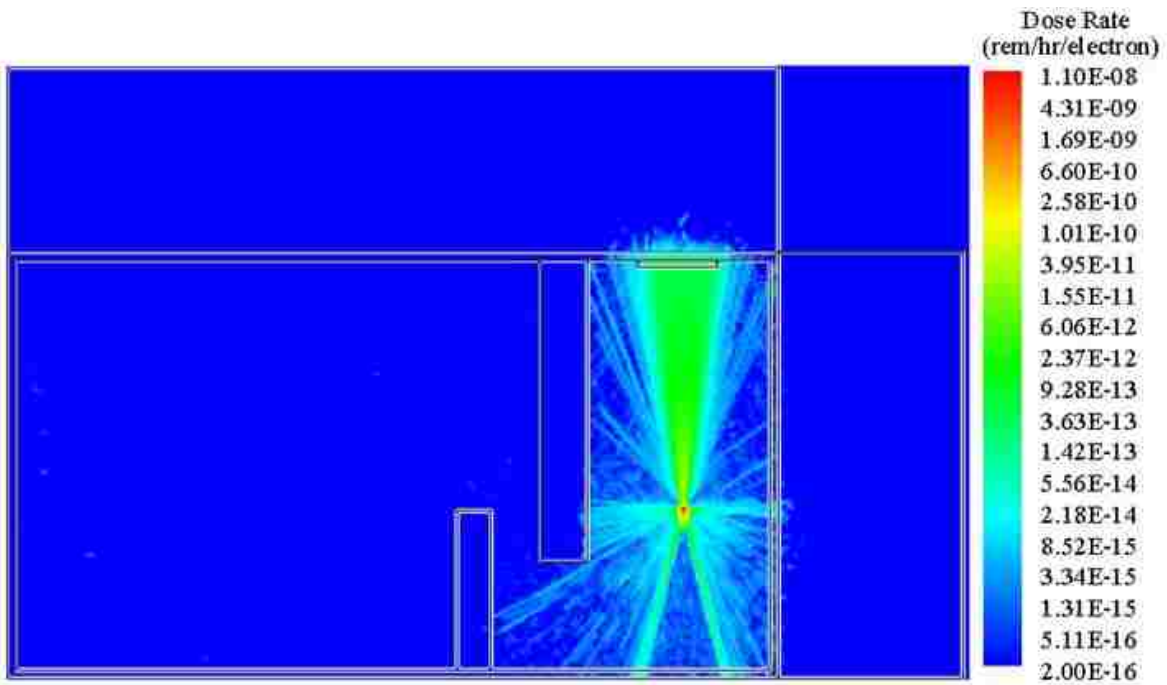


Figure 24. M6 Configuration 1 dose rates, 3 MeV electrons

It was found that dose rates within the accelerator facility are higher when the M6 is operated in high energy mode than when it is operated in low energy mode. This is due to higher energy photons being produced (endpoint energy of 6 MeV as opposed to 3 MeV) as well as larger fluxes of lower energy photons. For example, inspection of the computed photon spectra (shown in Figure 20 and Figure 21) reveals that the flux of 1 MeV photons produced in high energy mode is an order of magnitude larger than when in low energy mode. From Figure 23 and Figure 24 it is shown that the dose rates are largest directly in front of the linac, where the collimated beam is located. The fan shape is visible in both energy modes, with dose rates being higher in high energy mode. In both energy modes, the shielding maze minimizes the dose rates within the accelerator entry way.

4.2.2.2 M6 Configuration 2

Under certain conditions (i.e. production of photoneutrons using a neutron converter), the M6 may be used without the tungsten collimator pieces. As these collimator pieces attenuate the majority of emitted photons in all but the specific beam shape, the removal of these pieces leads to an increase in the photon fluxes and dose rates expected not only in the northern half of the facility, but throughout. The emitted photons will no longer take the shape of a fan beam, but rather a cone with dimensions according to the collimator cavity. The expected dose rates due to M6 operation without collimators are shown in Figure 25 and Figure 26.

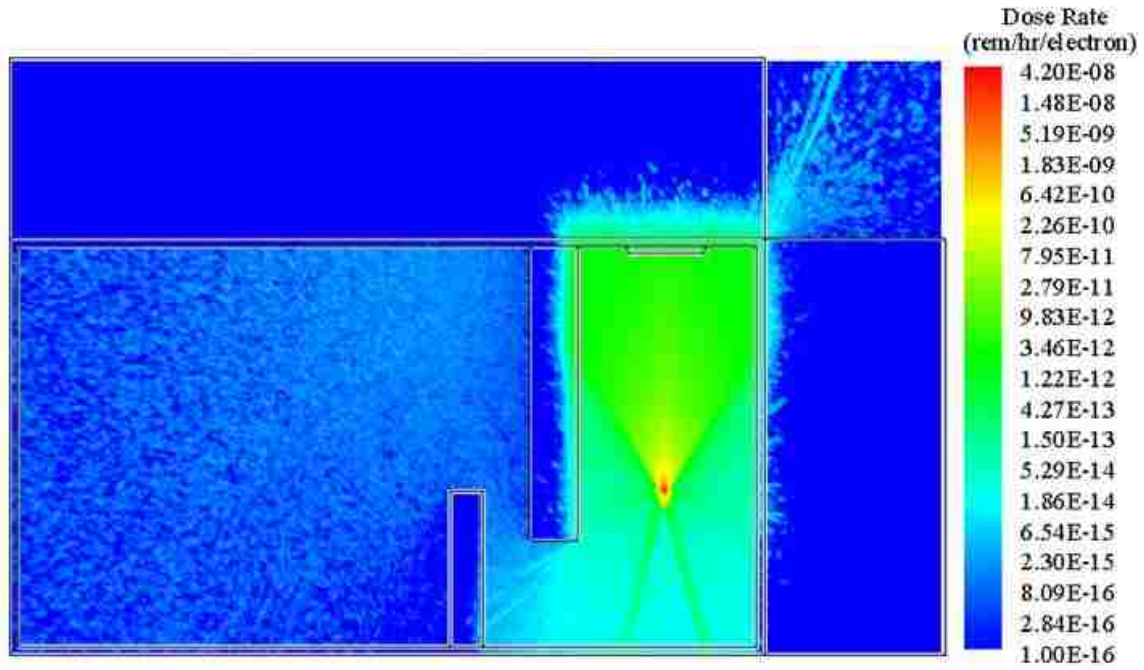


Figure 25. M6 configuration 2 dose rates, 6 MeV electrons

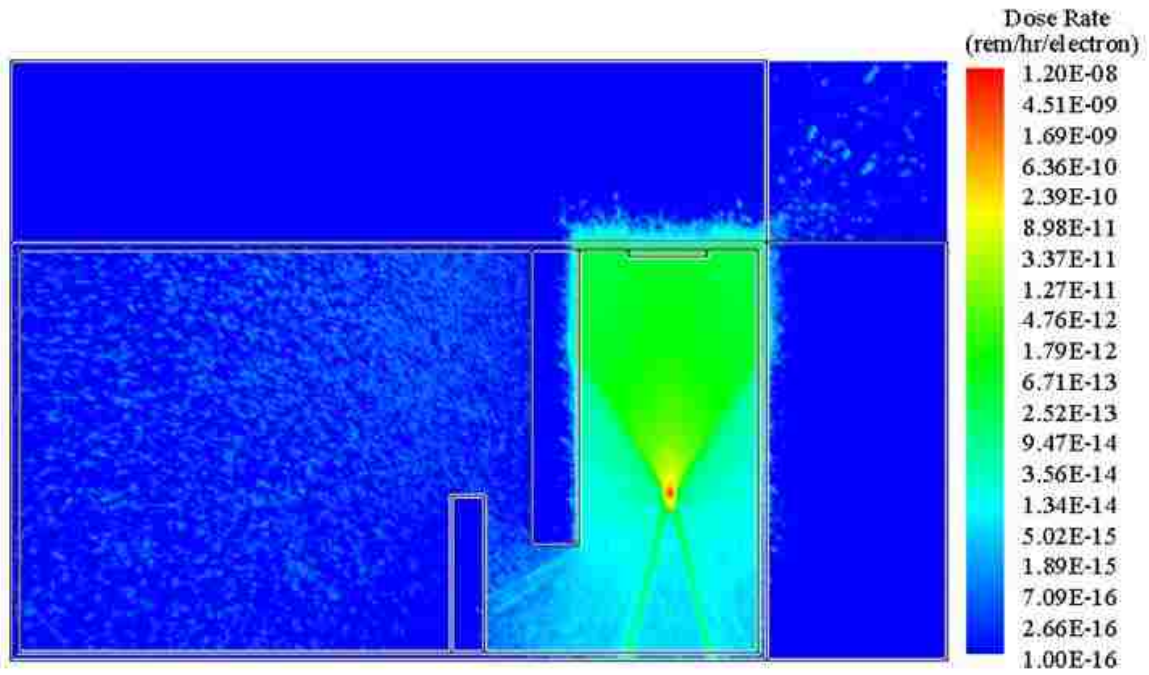


Figure 26. M6 configuration 2 dose rates, 3 MeV electrons

Similar to the configuration 1, the dose rates in the accelerator facility when the M6 linac is operated without collimators are higher when it is operated in the high energy mode. It was found that the dose rates within the northern half of the accelerator bay are greatly increased when the collimators are removed. In addition, it was determined that the dose rates in the entry way (0.259 ± 0.0020 rem / hr) were larger than they were in the configuration 1 (0.0004 ± 0.00002 rem / hr).

4.2.2.3 M6 Configuration 3

Determination of the dose rates within the accelerator facility for operation of the M6 without any shielding or collimator materials constitutes the "worst case scenario," or maximum possible dose rates achievable (Figure 27 and Figure 28). It is important to evaluate these dose rates in order to help validate facility safety measures.

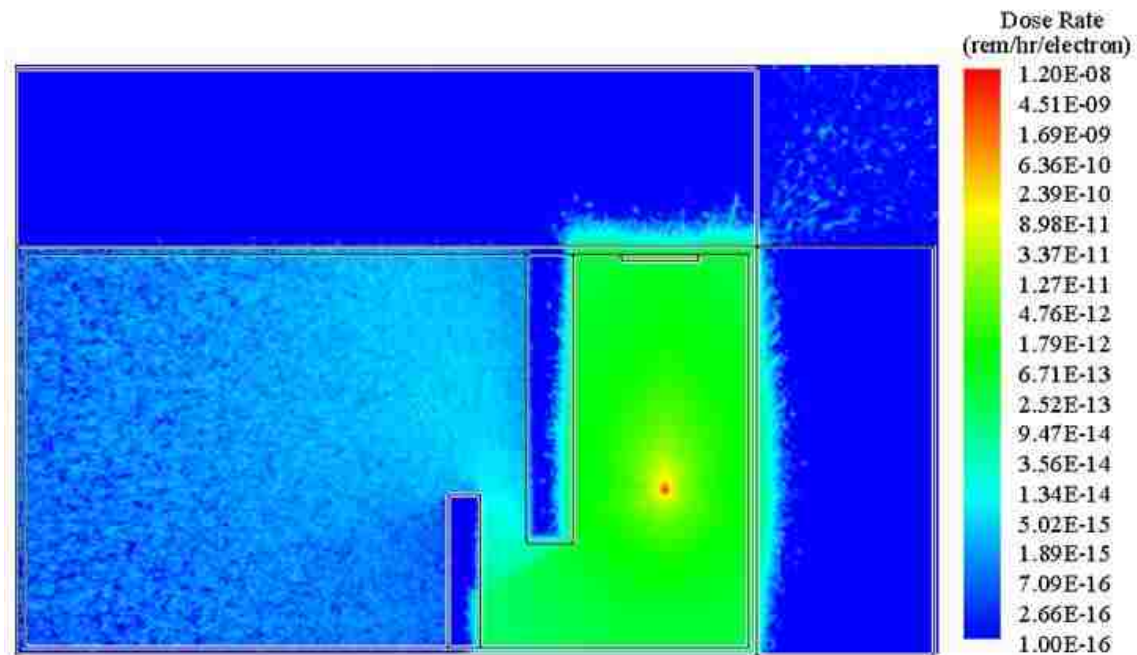


Figure 27. M6 configuration 3 dose rates, 3 MeV electrons

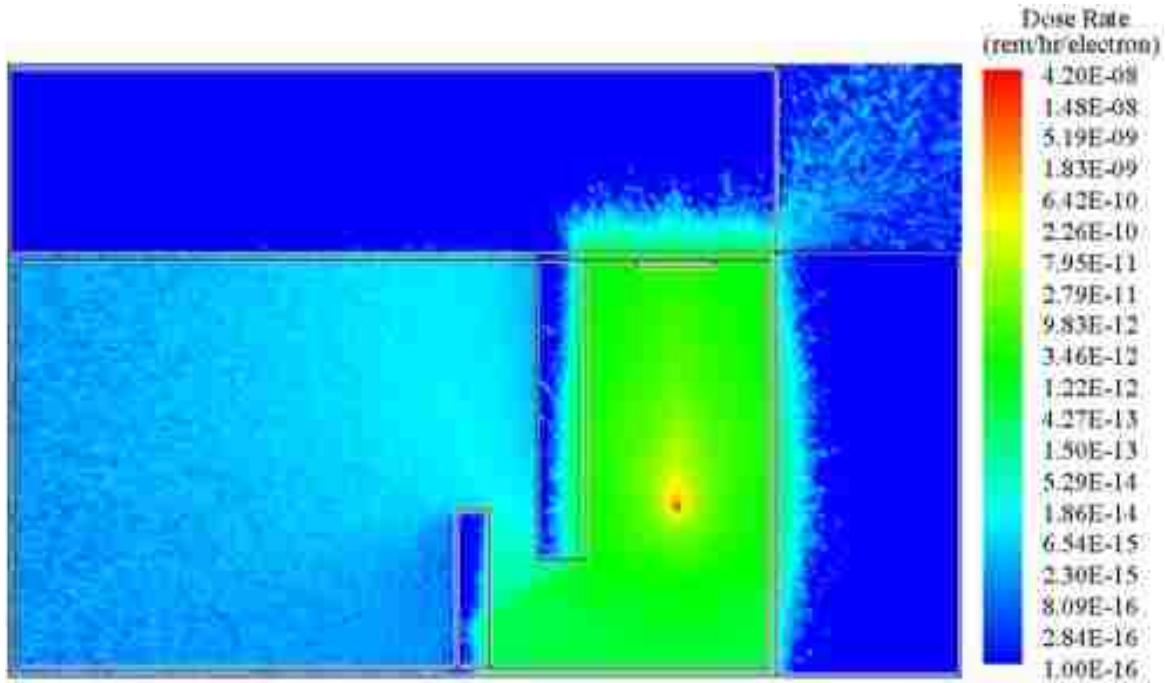


Figure 28. M6 configuration 3 dose rates, 6 MeV electrons

Removing the shielding and collimators results in an increase in the dose rates throughout the facility. When compared to the results from configurations 1 and 2, it was found that the dose rates in the accelerator bay to the rear and sides of the linac increased by an order of magnitude. This is due to the removal of the lead shielding in the rear of the M6 linac. In addition, the dose rates increased within the shielding maze (8.9 ± 0.05 rem / hr) as well as the entry way (1.4 ± 0.005 rem/hr).

4.2.2.4 Dose rate tallies summary

A summary table of results detailing the product of the F5 dose rate tallies with the M6 electron current for all three configurations of M6 operation is shown in Table 10. These results quantify the trends from the dose rate contour maps (shown in Figure 23 through Figure 28) at specific building locations (depicted in Figure 17 as the yellow and red dots).

Table 10. Accelerator facility dose rates due to M6 operation

Facility Location	Dose rate (rem hour ⁻¹)		
	Normal Operation	Without Collimators	Maximum Doses
Entry Room	0.0004 ± 0.00002	0.259 ± 0.0020	1.4 ± 0.005
Shielding Maze	0.002 ± 0.0001	0.317 ± 0.0046	8.9 ± 0.05
Northern Corners	3.29 ± 0.16	556 ± 1.3	583 ± 1.2
Southern Corners	0.037 ± 0.0008	6.3 ± 0.07	206 ± 0.5
At 1 meter	27571 ± 69	42081 ± 93	41986 ± 88
Sample Table	741 ± 1.93	1359 ± 2.7	1396 ± 2.8
Outside (No Berm)	n/a	n/a	2.9 ± 0.08

At all tally locations, the lowest dose rates occur under the normal M6 linac operation mode while the maximum dose rates occur when the collimators and shielding have been removed. When the location specific dose rates under normal operating conditions are compared with the maximum dose rates, the effectiveness of the shielding is determined. When M6 collimators and shielding are present, the dose rates in the corners of the northern bay are reduced by a factor of 265 while the dose rates in the southern corners are reduced by a factor of 105. The entry way dose rates are reduced by a factor of 350 while the dose rate in the center of the shielding maze is reduced by a factor of 180. In the absence of the berm outside the northeast corner of the building, the dose rate was found to be just under 3 rem/hr. When the berm is present, the dose rates outside fall below the 10 Code of Federal Regulations (CFR) 20 limit, for the dose rate in an unrestricted area (2 mrem/hr). At 2 m north of the linac, F5 tallies were used to determine the vertical dose rate profile for all three operating configurations (shown in Figure 29).

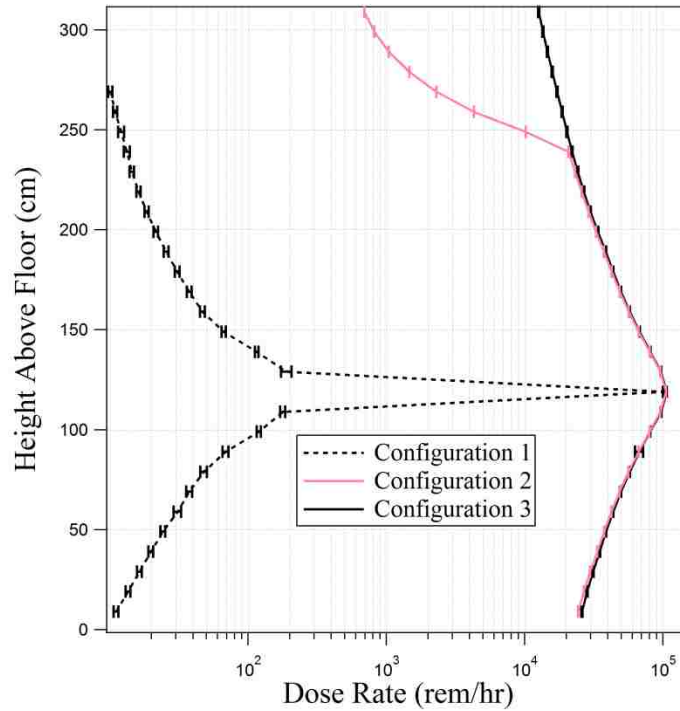


Figure 29. Vertical dose rate, M6

The results reflected large dose rates consistent with a fan beam shape at 1.2 m above the floor during normal operation. The use of collimators was shown to reduce the dose rates at all tally locations except at fan beam level. When collimators were removed, the fan beam expands to a cone shape and the dose rate increases. It was found that at dose rates near the ceiling (above 250 cm) were slightly lower (3.5×10^3 rem/hr) due to the tally locations being outside the radiation cone beam.

4.2.2.5 Validation of M6 Computational Model

During operation of the M6 linac, the dose rate is continuously measured and monitored by an internal ion chamber calibrated to a distance of 1 m north of the linac (denoted by the red dot in Figure 17). When the M6 was operated in 6 MeV mode, the dose rate was found to be 2.44×10^4 rem/hr. The computational dose rate was found by multiplying the normalized F5 tally result by

the electron current and found to be 2.76×10^4 rem/hr. The model and experimental measurement were found to be in agreement, with MCNP5 providing a conservative estimate for photon dose that is 1.13 time the measured value.

4.2.3 K15 Source Term Characterization

The bremsstrahlung spectra for the K15 linac were computationally determined for the low (9 MeV) and high (15 MeV) energy operation modes with the results shown in Figure 30 and Figure 31. A total of 500 million particle histories were used in the simulation to ensure that the error associated with each of the 100 equally spaced energy bins was below the 10% recommended by MCNP for F4 tallies.

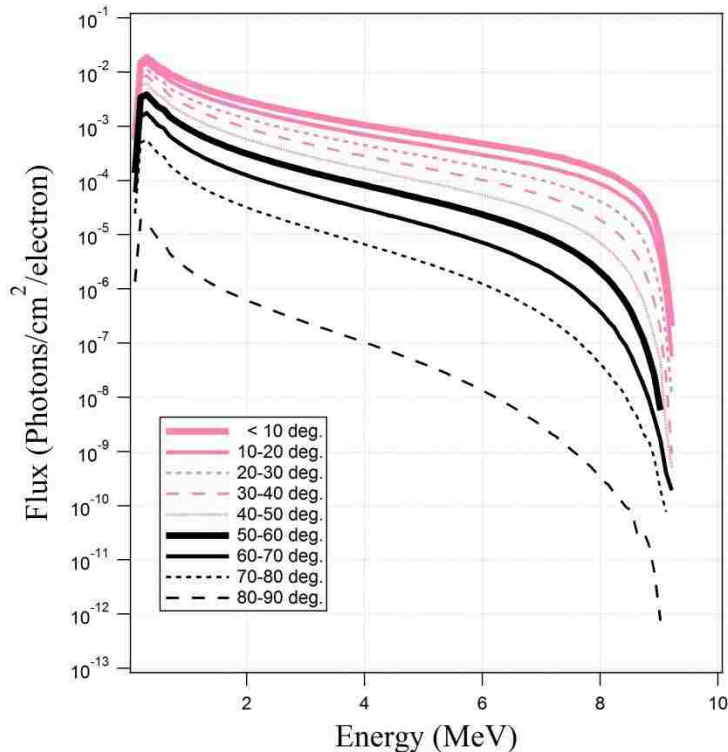


Figure 30. K15 Bremsstrahlung spectra for 9 MeV incident electrons

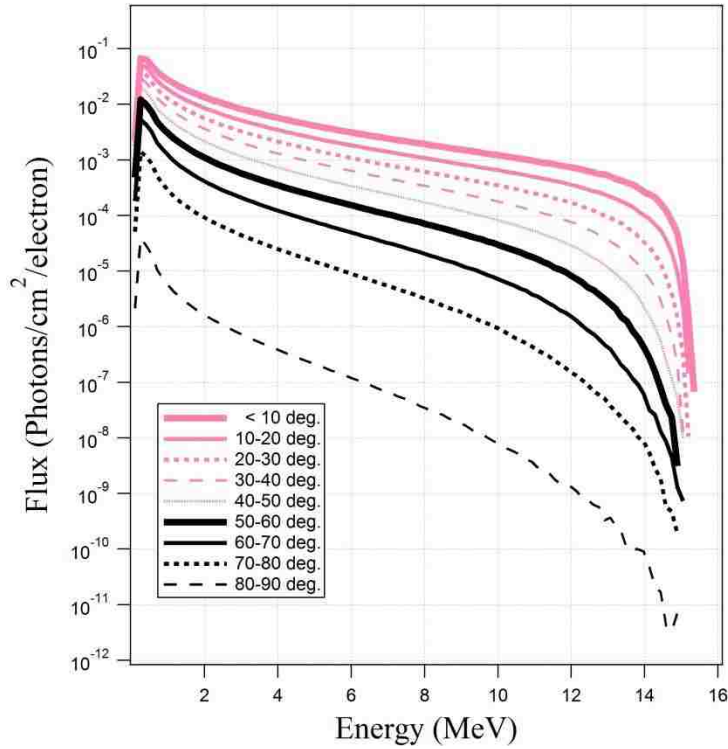


Figure 31. K15 Bremsstrahlung spectra for 15 MeV incident electrons

As was the case with the M6, the largest photon fluxes occur within 10 degrees of the center of the linac target and decrease with increasing outward angle. In both operating modes, at around 1 MeV, the fluxes of bremsstrahlung photons are generated nearly 3 orders of magnitude larger within an angle of 10 degrees, than they are at angles greater than 80 degrees. This flux ratio increases to 5 orders of magnitude for 8 MeV photons. There is typically an order of magnitude difference between the fluxes at each angular interval between the two K15 operation modes. The error associated within each energy bin in the bremsstrahlung spectra results are less than the MCNP recommended value of 10% for an F4 tally.

4.2.4 Radiation Environment During Operation of the K15 Linac

The K15 linac is not typically operated with a fan beam collimator, but rather with a 30 degree cone beam collimator. Other collimators may be used, but for the purpose of this research, only the 30 degree cone case was considered. Two scenarios were modeled for K15 operation, normal operation with the cone collimator and maximum dose rate achievable without any shielding or collimators (Table 11).

Table 11. K15 Linac configuration data

K15 Linac Configuration	Conditions	Collimators	Shielding
1	Normal Operation	Yes	Yes
2	Maximum Output	No	No

For each linac operating configuration, the TMESH/RMESH tally was used to determine the overall building dose rate footprint. Due to the energies of the photons generated in the linac target in high energy mode being greater than the neutron binding energies of several materials in the linac shielding as well as the facility room structures (Table 12), photoneutron fluxes as well as contribution to dose rate must be considered. For photon energies higher than 10 MeV, photoneutron generation in the MCNPX was expected.

Table 12. Photoneutron binding energies of common materials [98]

Z	Isotope	Threshold Energy (MeV)
5	¹¹ B	11.45
6	¹² C	18.74
7	¹⁴ N	10.56
8	¹⁶ O	15.67
11	²³ Na	12.42
12	²⁴ Mg	16.54
13	²⁷ Al	13.06
25	⁵⁵ Mn	10.23
26	⁵⁶ Fe	11.20
27	⁵⁹ Co	10.45
28	⁵⁸ Ni	12.22
29	⁶³ Cu	10.85
30	⁶⁴ Zn	11.86

4.2.4.1 K15 Configuration 1

Under normal operation of the K15 linac, the building dose rates due to photon fluxes were determined and are shown in Figure 32 and Figure 33, for low and high energy modes, respectively.

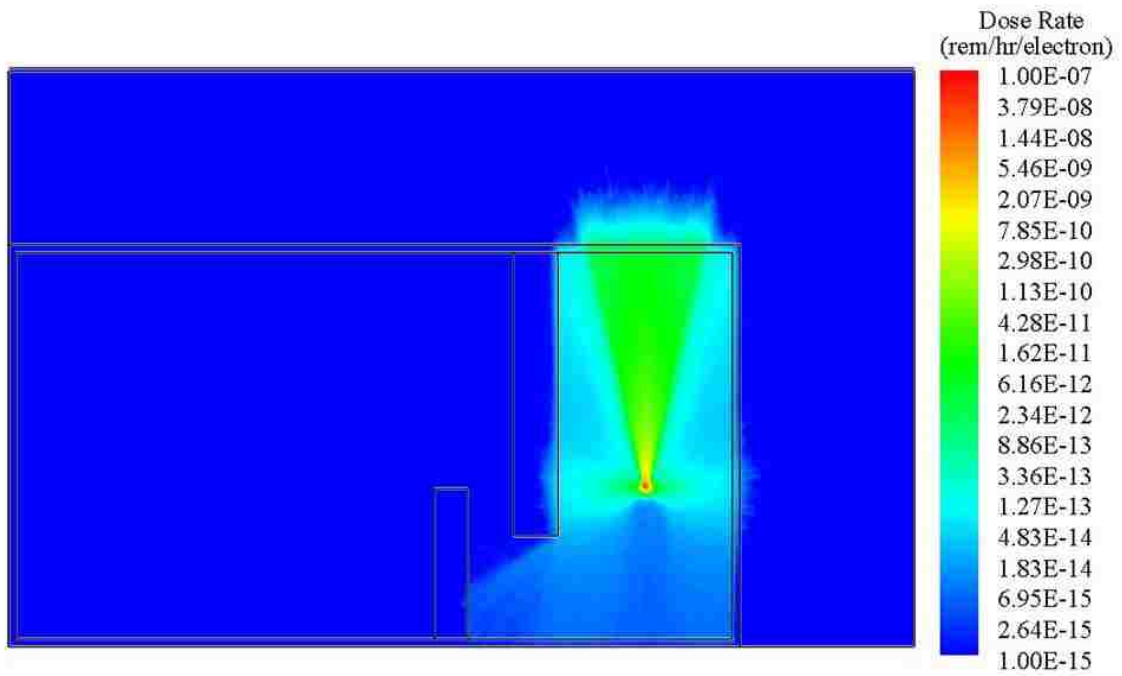


Figure 32. K15 configuration 1 photon dose rates, 9 MeV electrons

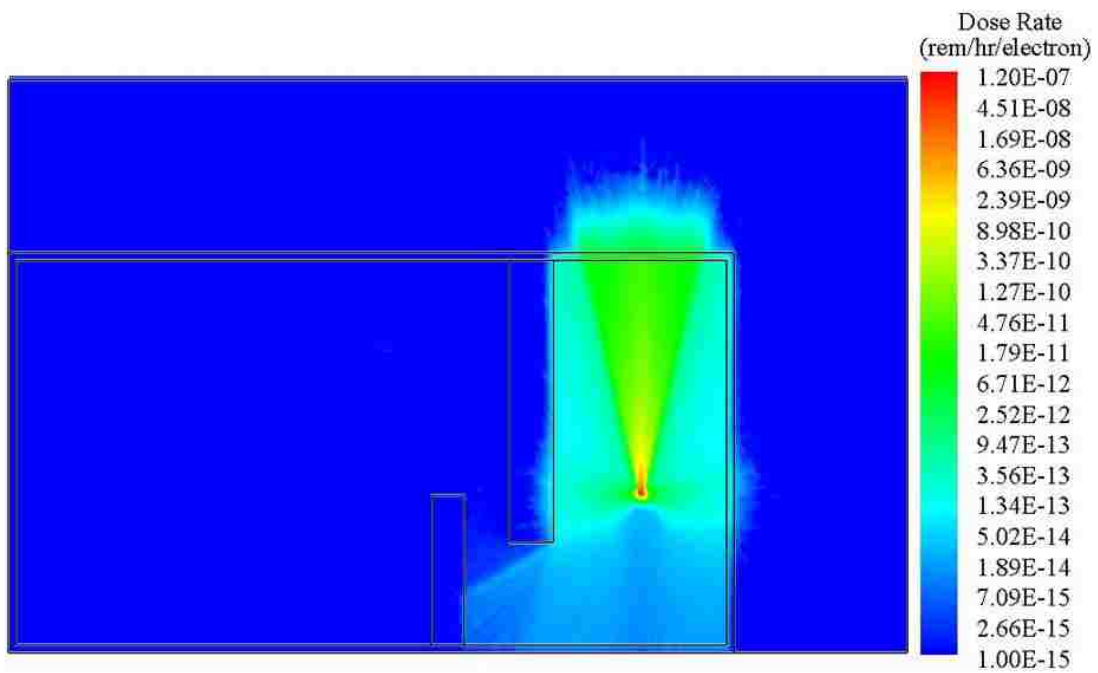


Figure 33. K15 normal operation photon dose rate, 15 MeV electrons

The trends in the computed dose rates due to the K15 operation were found to be similar to those due to the M6 operation. The dose rates in the accelerator bay were highest, while the shielding maze helped to minimize dose rates in the entry way. The earthen berm minimized the photon dose rate outside of the facility to effectively nothing. Dose rates to the sides and rear of the K15 were higher when operated in high energy mode as compared to low energy mode. The vertical profile of the photon dose rate at 1 m north of the linac was measured using F5 tallies and is shown in Figure 34. The error associated with each value is less than the 5% recommended by MCNP for F5 tallies.

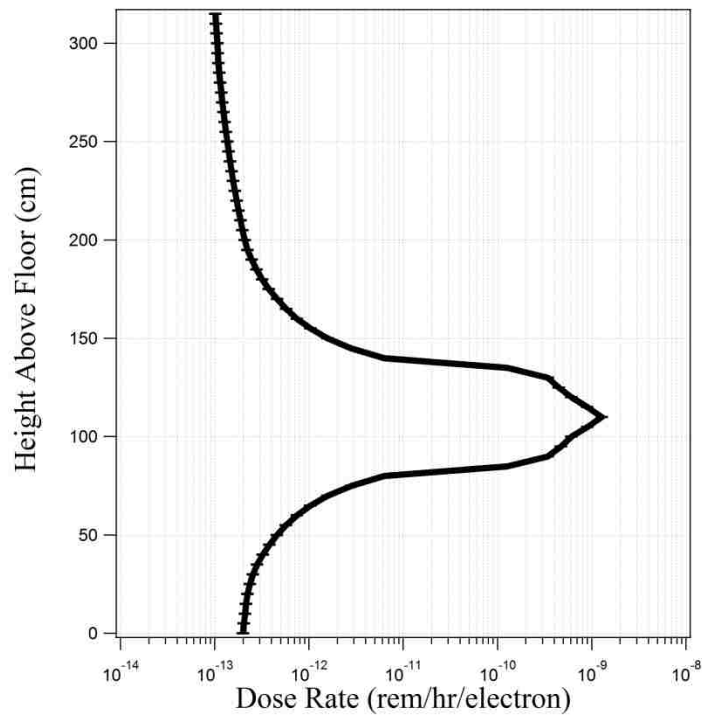


Figure 34. Photon dose rate during normal operation of the K15 in high energy mode

The computed normalized results show that the photon dose rate is largest down the center of the photon beam (9.5×10^{-8} rem/hr/electron), at a height of 1.11 m (43.75") above the floor. The

dose rates near the floor (9.0×10^{-12} rem/hr/electron) and ceiling (1.0×10^{-8} rem/hr/electron) of the building were determined to be approximately four orders of magnitude lower than the dose rate in the center of the beam. The largest dose rates were found to occur between heights of 75 and 125 cm, corresponding to the height of the conical collimated photon beam. Dose rates quickly decrease outside of the photon beam.

The neutron contribution to the dose rate during the normal K15 operation in high energy mode is shown in Figure 35. No photoneutrons were produced during operation of the K15 in low energy mode due to the endpoint energy of the bremsstrahlung spectra being below the (γ, n) reaction thresholds of the materials in the MCNPX model.

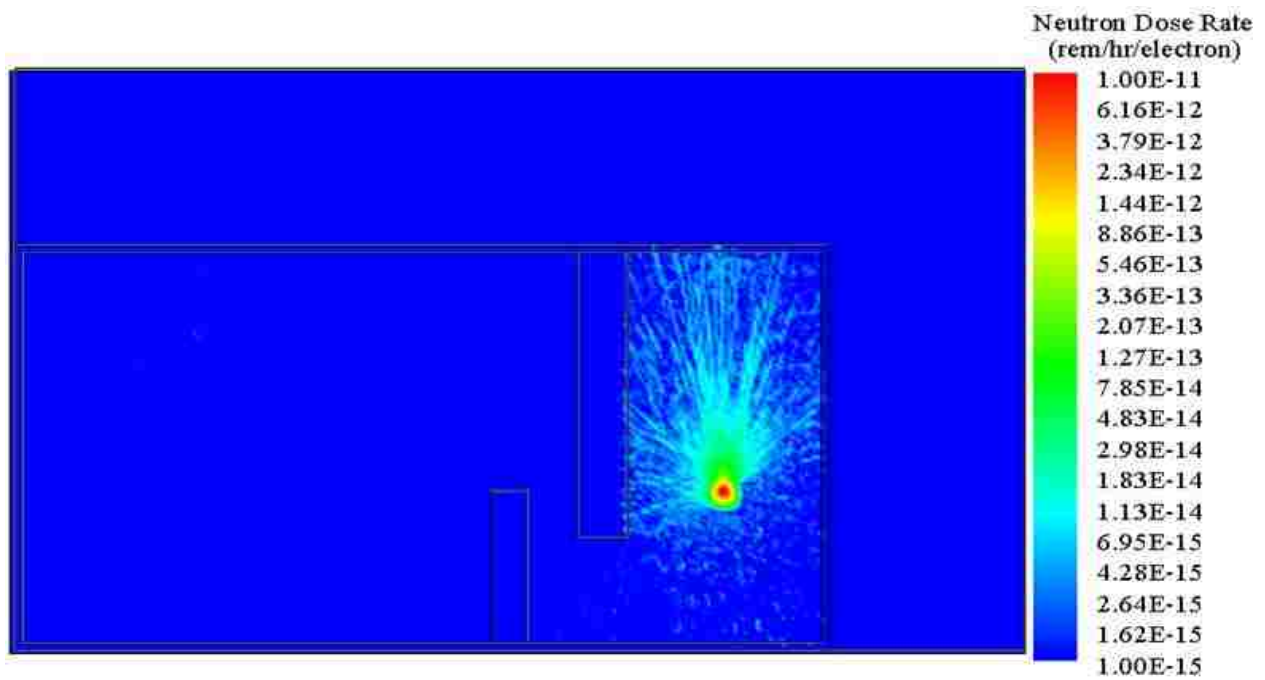


Figure 35. Dose rates, K15 configuration 1, 15 MeV electrons

The results in Figure 35 show that the neutron flux was primarily contained within the accelerator bay. Neutron contribution to dose rate was highest north of the linac primarily due to the lack of poly shielding behind the target head. The back end of the K15 contained several inches of polyethylene shielding which reduced the neutron dose rate in the southern end of the accelerator bay. The maximum dose rate due to neutron flux was determined to be several orders of magnitude lower than the photon contribution. While the profile shape of the photon dose rate corresponded to the shape of the conic collimator, the neutron dose rate does not possess the same shape. This is because neutrons were produced in the high z collimator materials rather than being shaped by it. The neutron spectrum at a distance of 1 m behind of the linac target was determined with an F5 tally (see Figure 36).

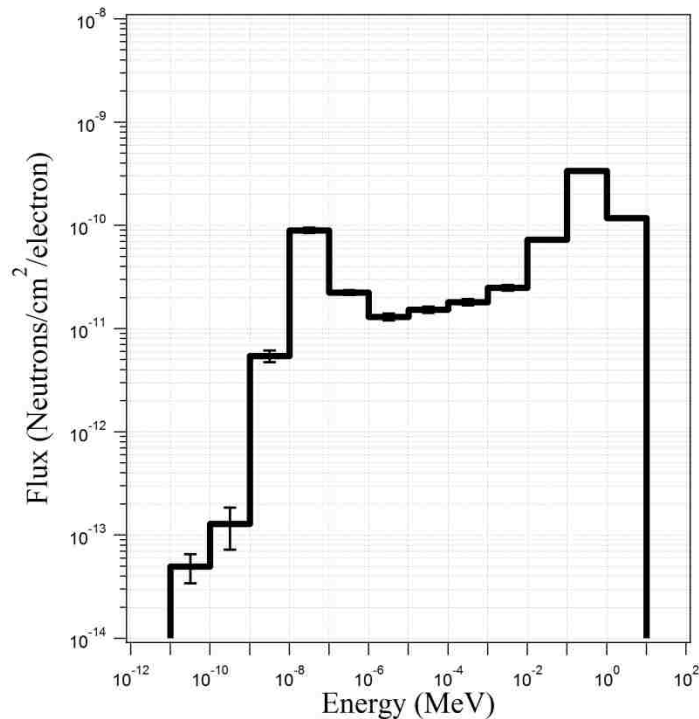


Figure 36. Photon neutron spectrum 1 m from K15 linac

The largest fluxes of neutrons were determined to be in the 0.1 to 1 MeV range with the second largest fluxes for neutrons just above the thermal range (10^{-8} to 10^{-7} MeV). The total neutron flux at the F5 tally location was found to be 4.8×10^4 neutrons/cm²/s.

4.2.4.2 K15 Configuration 2

The geometry in the MCNPX model was modified to simulate the K15 operation without shielding and collimators in order to determine the maximum dose rate output due to operation of the linac in high energy mode. Maximum photon dose rate results are shown in Figure 37 while maximum neutron dose rates are presented in Figure 38.

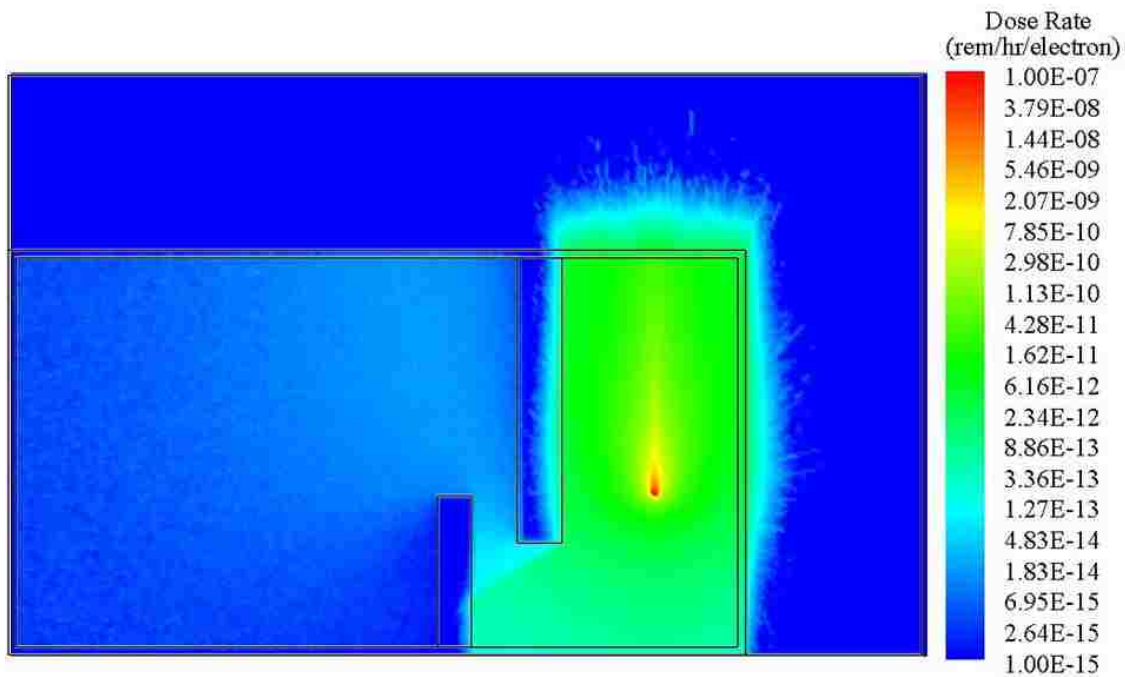


Figure 37. K15 maximum photon dose rate, 15 MeV electrons

The results show that without collimators and shielding, the dose rates due to photons increase throughout the building. Comparing the RMESH tally data between the two linac operating configurations reveals that the K15 collimator and shielding materials help to reduce photon dose

rates by factors of 238, 33 and 7.5 times for locations at 1 m north of the linac, in the center of the shielding maze and in the center of the entryway, respectively.

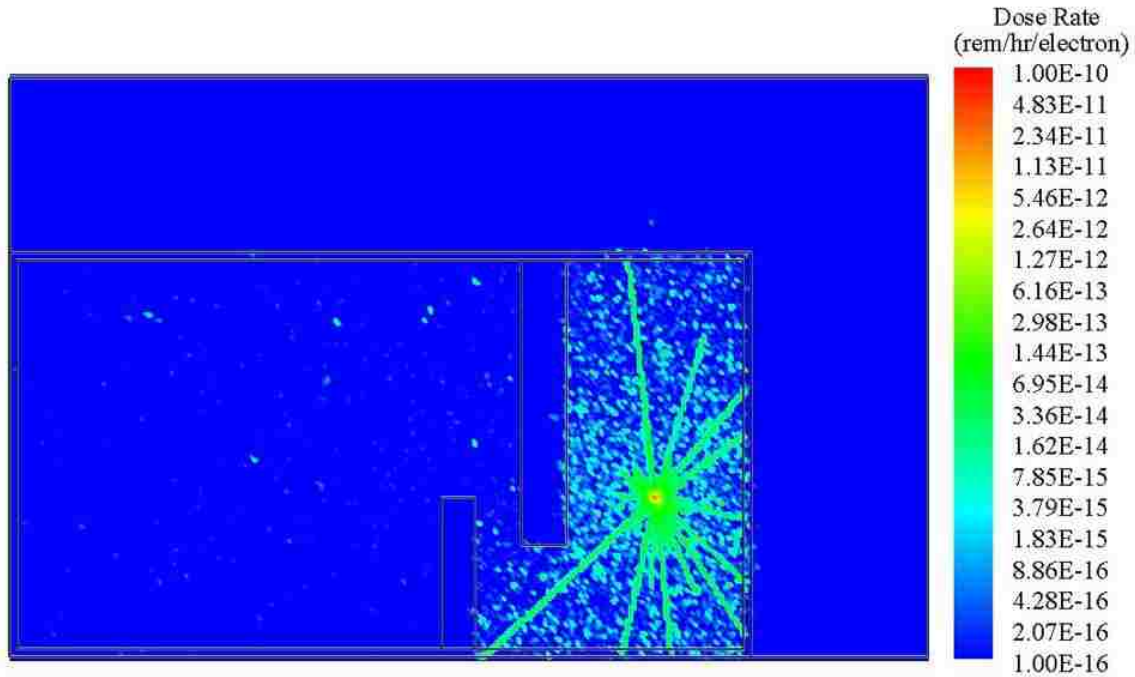


Figure 38. K15 maximum neutron dose rate, 15 MeV electrons

The maximum neutron dose rate footprint is similar to that of the normal neutron dose rate map with the exception that the dose rate has increased in the southern half of the accelerator bay. This is due to the fact that the polyethylene neutron shielding was removed in the rear of the linac.

4.2.4.3 Validation of K15 Computational Model

The photon dose rate from a K15 was experimentally measured at Varian Medical Systems by an internal ion chamber (calibrated at 1 m north of the linac) and found to be 11700 rem/min for high energy mode and 3500 rem/min for low energy mode. MCNPX F5 tally results at the same locations yielded values of 1.40×10^{-9} rem/hr/starting electron and 3.10×10^{-10} rem/hr/starting

electron for high and low energy respectively. Multiplying these tally values by the respective DC averaged electron currents and converting to the appropriate time scale gave MCNPX values for high and low energy dose rate as 15,744 and 3687 rem/min, respectively. Thus, the MCNPX model gave conservative estimates of photon dose rate by scale factors of 1.35 for high energy mode and 1.05 for low energy mode.

4.2.5 Summary of Linac Source Term Characterization

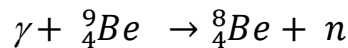
It is important for safety purposes to quantitatively evaluate the differences in radiation production between the two linacs. At one meter north of the linac, the M6 linac produces a photon dose rate of just over 400 rem/min. At the same location, the photon spectra from the K15 generates dose rates 28 times larger (high energy mode) and 8 times larger (low energy mode) than the M6 does. When compared to the M6 results, the K15 maximum dose rates an order of magnitude larger. This is due to the accelerator producing higher energy photons (and in greater fluxes). At 1 cm behind the respective linac targets, the maximum photon fluxes occur within a 10 degree conic angle. At this angle, the total photon flux (normalized computational result multiplied by the electron current) of the K15 in high energy mode is over 4 times as large as that of the M6.

Table 13. UNLV linac characteristics

Angle	Absolute Photon Flux (photons/cm ² /s)		
	K15 (15 MeV)	K15 (9 MeV)	M6 (6 MeV)
10	4.27E+14	1.47E+14	9.53E+13
20	2.81E+14	1.07E+14	7.00E+13
30	1.89E+14	7.66E+13	4.93E+13
40	1.27E+14	5.42E+13	3.40E+13
50	8.03E+13	3.61E+13	2.19E+13
60	4.38E+13	2.09E+13	1.24E+13
70	1.78E+13	8.97E+12	5.41E+12
80	4.34E+12	2.60E+12	1.29E+12
90	9.75E+10	6.91E+10	2.04E+10
Measured Dose Rate (rem/m/min)	11700	3500	406.67
Computational Dose Rate (rem/m/min)	15744	3687	460
Scale Factor (MCNP Dose / Measured Dose)	1.35	1.05	1.13

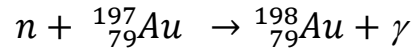
4.3 Accelerator Driven Photoneutron Source

It was desired to use the M6 linac to produce photoneutrons through the interaction of bremsstrahlung photons with a cylindrical (9" long, 3" diameter) beryllium (0.99999 ⁹Be) converter. The 6 MeV endpoint energy of the bremsstrahlung generated by the M6 is greater than the neutron separation energy of beryllium (1.66 MeV) leading to the generation of neutrons from the (γ ,n) reaction:



The M6 computational model was used to calculate the neutron fluxes for two different geometric orientations (vertical and horizontal) of the beryllium converter. Following the determination of the converter orientation yielding the maximum neutron flux, neutron activation

measurements were conducted in order to validate the model. A gold activation foil was placed on top of the beryllium converter where it was used to measure the flux of neutrons produced during the irradiation cycle. The ^{197}Au nuclei in the foil capture the photoneutrons generated in the converter, resulting in the formation of excited ^{198}Au nuclei according to the (n, γ) reaction:



The newly produced ^{198}Au nuclei de-excite according to the decay scheme shown in Figure 39.

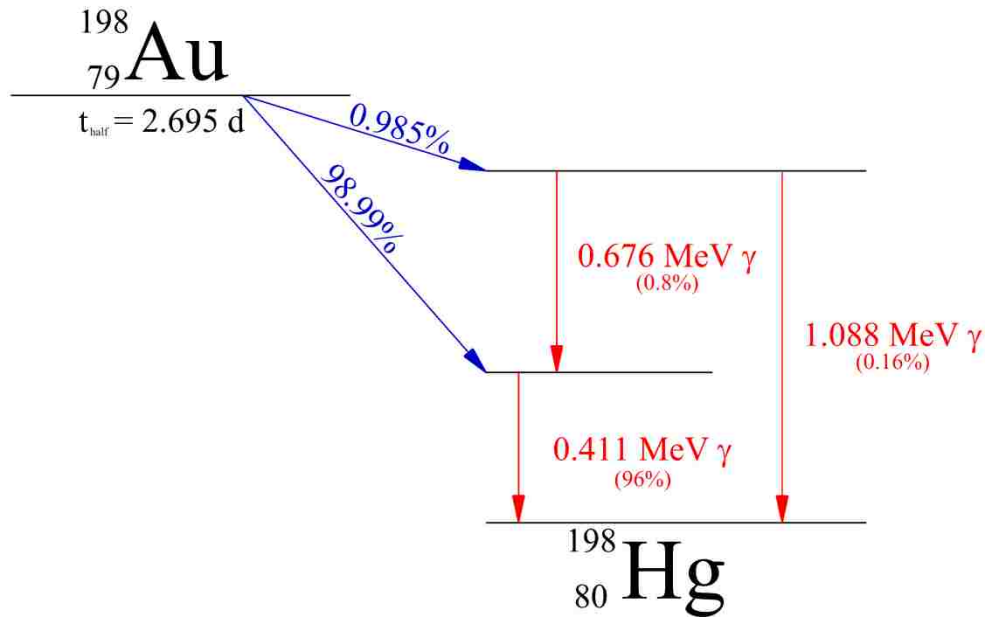


Figure 39. Au-198 decay scheme

An ORTEC High Purity Germanium (HPGE) detector was used to determine the count rate and the energy of the gammas released during the decay of the atoms in the activated gold foil.

The radioactivity of the gold foil was determined from these counts and used to validate the MCNPX model.

4.3.1 MCNPX Model

MCNP5 was used to determine the accelerator facility dose rates during operation of the M6 linac as the no photonuclear reactions took place (due to the endpoint energy of the bremsstrahlung spectrum being lower than the photoneutron energy thresholds of the linac and nearby building materials). However, as MCNP5 lacks photoneutron production and interaction capabilities, the model was run in MCNPX. Similar to the K15 model, the *ispn* entry on the "phys:p" card was changed from the default value of "0" (off) to "1" (on, biased) to account for photonuclear production. The model geometry was modified by removing the collimator pieces from the M6 linac, and placing the beryllium converter in the center of the collimator cavity in both vertical and horizontal configurations. As with the previous computational models, F4 tallies on a series of thin radial surfaces were placed 1 cm outside the collimator cavity to determine the angular distribution of neutrons generated within the converter (Figure 40). The cross section library used was the ENDF/B-VII for photonuclear data, denoted by the ".70u" identifier.

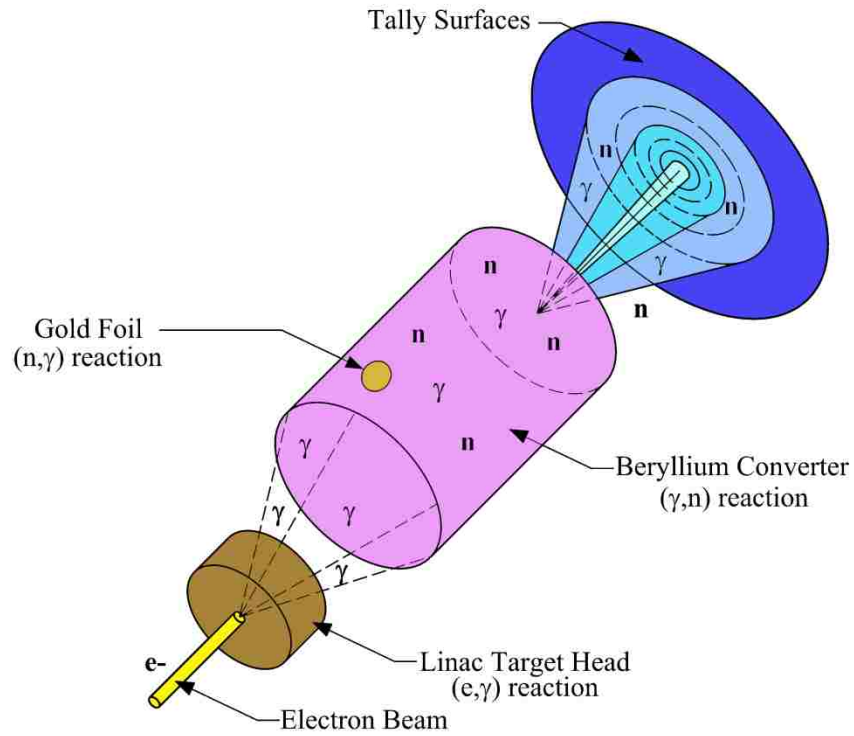


Figure 40. Determination of photoneutron flux

The results for fluxes (MCNP normalized F4 tally results times the electron current of the M6) of neutrons produced by the interaction of bremsstrahlung photons with the beryllium converter are shown in Figure 41.

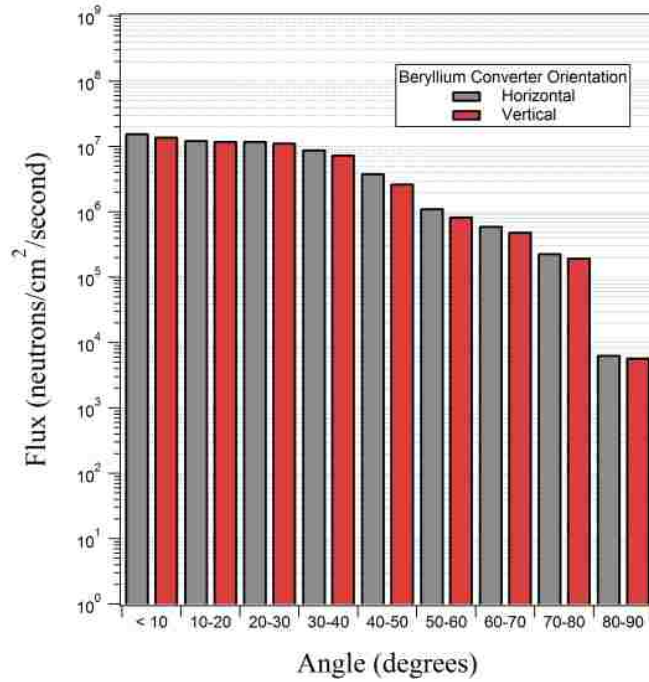


Figure 41. Comparison of neutron fluxes based on converter orientation

The results showed that photoneutron production was 13% larger when the converter was in the horizontal as opposed to the vertical position. The largest neutron flux occurred during horizontal placement of the converter and was found to be 1.6×10^7 neutrons/cm²/s. Additionally, neutron fluxes on the order of 10^7 were found to be possible for angles up to 30°. The photoneutron spectrum at a conic angle of 10° is shown in Figure 42.

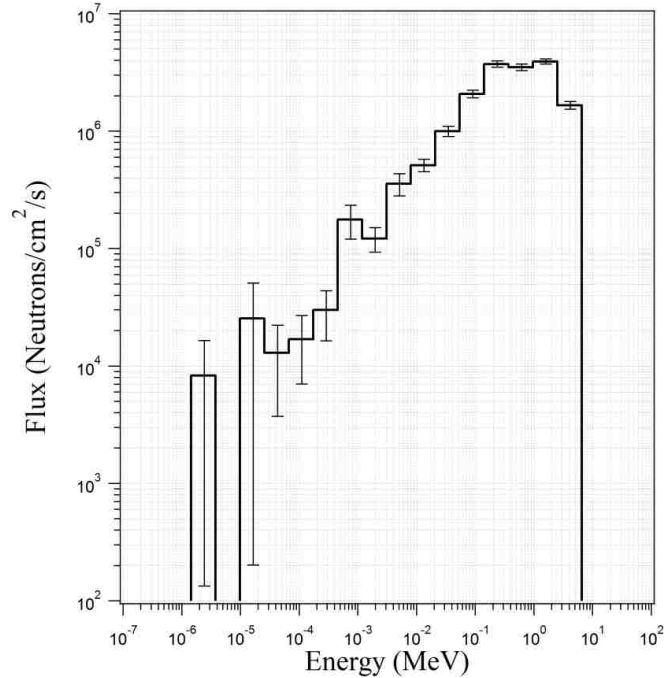


Figure 42. Photoneutron spectrum, 1 cm behind collimator cavity

4.3.3 Experimental Set-Up and Results

With the computational results determining that the maximum neutron fluxes occur when the converter is in the horizontal orientation, an experiment was carried out in order to validate the model. The table on which the M6 sits was lowered and the collimator pieces were removed. The beryllium converter was placed horizontally in the collimator cavity. With the collimators removed and neutrons being produced, the dose rates were expected to rise throughout the facility. Three layers of polyethylene shielding (2" thick normal polyethylene and 1" thick 5% borated polyethylene) was placed on top and behind the linac in order to minimize neutron dose rates within the building (shown in Figure 43).



Figure 43. M6 linac setup used for photoneutron production

A gold foil (1/2" radius, 0.002" thick) was placed on top of the horizontally oriented beryllium converter, 1.5" from the leading edge and used to measure the neutron flux generated by the (γ,n) reaction occurring within the beryllium converter. After a 1 hour irradiation, the gold foil was removed and was placed in an HPGe detector where the gamma-ray emissions from the gold were counted for 2 days, with the resulting gamma spectrum shown in Figure 45.

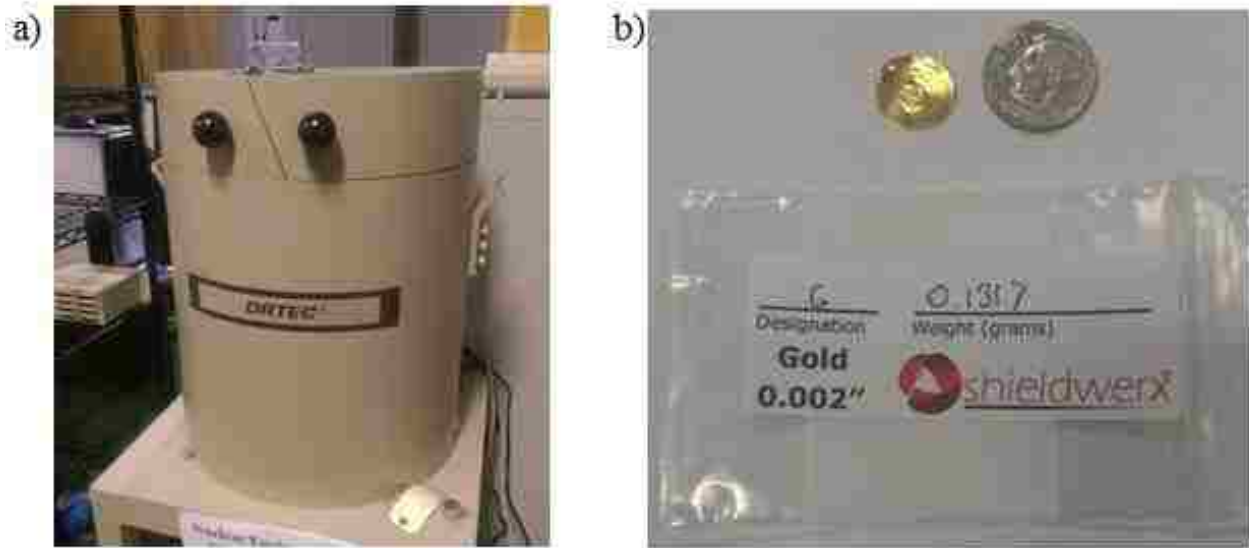


Figure 44. Experimental equipment a) ORTEC HPGe detector and b) a gold activation foil

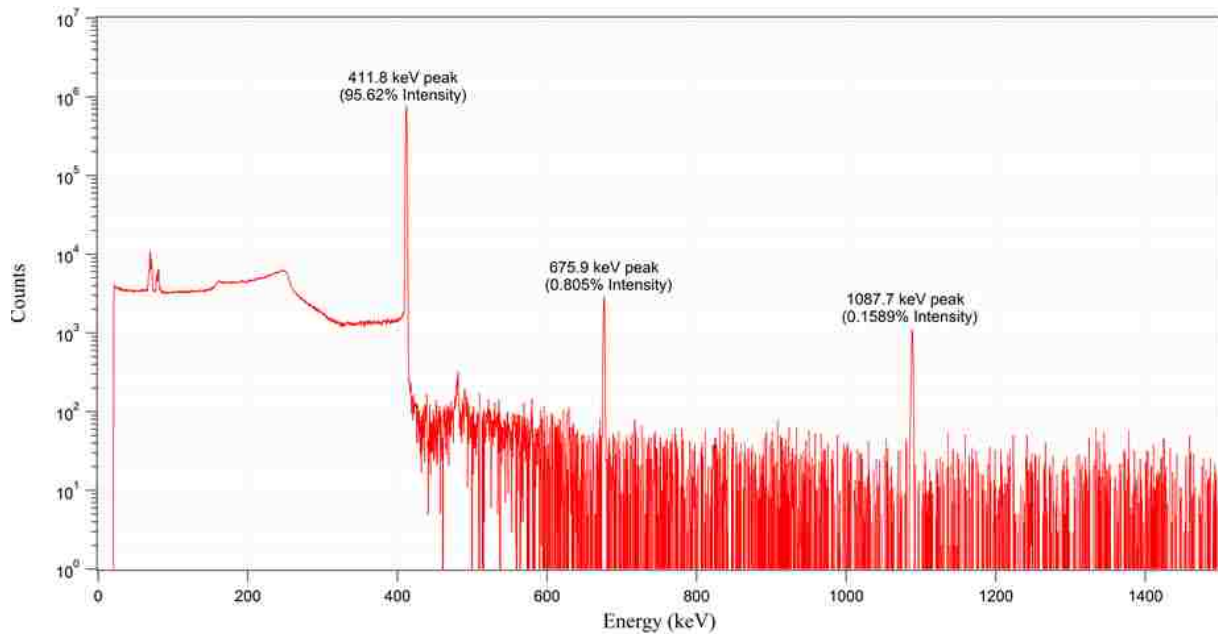


Figure 45. Activated gold foil spectrum

The gamma spectrum from the gold foil showed three distinct energy photopeaks at 411.8, 675.9 and 1087.7 keV, with intensities corresponding to those expressed in the decay scheme.

Analysis of the count rate in the 411.8 keV photopeak determined the activity of the gold foil to be 3.49×10^{-3} mCi after two days, corresponding to an initial activity of 5.86×10^{-3} mCi. After one half-life (2.7 d for ^{198}Au), the activity would be expected to be 2.93×10^{-3} mCi. This corresponds to 3.62×10^6 counts as would have been seen by the HPGe if the gold foil was counted for the first full half-life. Modifying the number of counts by the efficiency of the detector (15% at 411.8 keV) and the intensity of the photopeak (95.62%) yields the number of (n, γ) reactions occurring during the first half-life of gold. As the number of reactions during the first half-life of an activated isotope is equal to the exactly half of the total number of reactions that will occur during the total decay time, doubling this number will determine the total number of reactions that occurred during irradiation. Neutron activation analysis of the gold foil determined that the total number of (n, γ) reactions that occurred in the foil during 1 hour of irradiation was 5.03×10^7 .

4.3.4 Model Validation

To calculate the number of (n, γ) reactions occurring in the foil determined it was necessary to place an F4 tally with an FM tally modifier on the gold foil. The syntax for the MCNPX input is seen in Figure 46.

```

c -----
c
c Tally on Au foil to calc. (n,gamma) rxns
F4:n 7003
FM4 -1 11 102
sd4 1

```

Figure 46. Calculating the number of reactions in MCNPX

The number 4 on the FM4 designator defines the tally modifier to be attached to the corresponding tally number 4. The "-1" instructs MCNPX to modify the neutron F4 tally results (on cell 7003) by multiplying by the atomic density of material "11" (corresponding to the gold 197 isotope in this model) as well as the cross section of the of the appropriate MT reaction number. In this case, "102" denotes the (n, γ) reaction cross section. By default, MCNPX divides the final product by the volume of the cell (7003) in order to normalize the result (per unit volume). The "sd4 1" line instructs MCNP to not divide the final tally result by the volume of the cell (or it can be understood as MCNP multiplying through by the volume after dividing by the volume) so the units of the tally result are the total number of reactions occurring within the cell per starting electron. The result of the modified F4 tally on the gold foil was calculated to be 5.89×10^{-11} (n, γ) reactions/starting electron. The electron current of the M6 was previously determined to be 3.4×10^{14} electrons/s and the linac was operated for 1 hour (3600 s). Multiplying the modified F4 tally result by the electron current and the linac operation time gives the computed value for the total number of (n, γ) reactions occurring within the gold foil after 1 hour of operation as 7.21×10^7 . The gold foil activation results determined that the total number of (n, γ) reactions was 5.03×10^7 resulting in a final scale factor (computational/experimental) of 1.43.

Chapter 5: Assay of SNM Using a 15 MeV Linac

With the computed K15 linac based photon source term validated by the experimental photon dose rate measurement, it was used as a radiation probe for SNM interrogation models. The results from neutron induced fission studies have led to the generation of databases with a large amount of product yields, yet similar photofission data has been lacking. Recent investigations have aimed to determine these yields for the photofission assay. Delayed gamma-ray yields from the photofission assay of depleted uranium (DU), ^{239}Pu and ^{232}Th [99] and prompt gamma-ray yields from neutron-induced fission were studied computationally [100]. Experimental work on the cumulative yields of fission products generated during the thermal fission of ^{235}U and ^{239}Pu and the fission product yields produced from 16.3 MeV and 19.4 MeV bremsstrahlung was performed [101]. Fission product yields were also determined for the photofission of ^{235}U and ^{238}U for 12 MeV, 15 MeV, 20 MeV, 30 MeV and 70 MeV bremsstrahlung sources [102, 103] and for ^{238}U using a 9 MeV bremsstrahlung source [104]. Delayed gamma-ray yields have also been determined for the photofission of ^{238}U and ^{239}Pu using a 22 MeV linac [105]. Lastly, delayed neutrons from the photofission of ^{238}U by 19 MeV bremsstrahlung were investigated [106]. There have not been studies on the neutron yields using the K15 linac.

5.1 Computational Model of SNM Assay

MCNP6 input decks were created to simulate the photofission assay of SNM by K15 linac generated bremsstrahlung photons. The models simulated the irradiation of NRC category 1 amounts (5 kg) of shielded SNM at a distance of 1 m. The 5 kg SNM spheres for ^{235}U and ^{239}Pu have radii of 3.97 and 2.89 cm, respectively. The effects of 5 cm thick of polyethylene and lead shielding in the active interrogation of SNM spheres were also studied. The models were used to

determine the angular dependent radiation environment at a distance of 1 cm behind the shielded spheres in addition to the determination of the neutron spectra at these locations.

For the photofission assay models, the source terms were defined using the bremsstrahlung spectrum instead of the impinging 15 MeV electron beam. This approach (using the bremsstrahlung photon spectrum as the source term, not the electron beam) decreases computational time and allows for quicker solving of the problems of interest. The K15 photon spectrum was previously determined at a distance of 1 cm behind the linac target for increasing conic angles of 10 degrees. In this model, it was desired to define the photon source such that it exactly engulfed the SNM target and shielding (Figure 47). Defining the SDEF card in this way ensures model accuracy in simulating only the photon spectrum that interacts with the shielded SNM. The angular dependent photon spectrum used in the SDEF card will vary depending on the SNM type used, the shielding thickness, and the distance between the source and target.

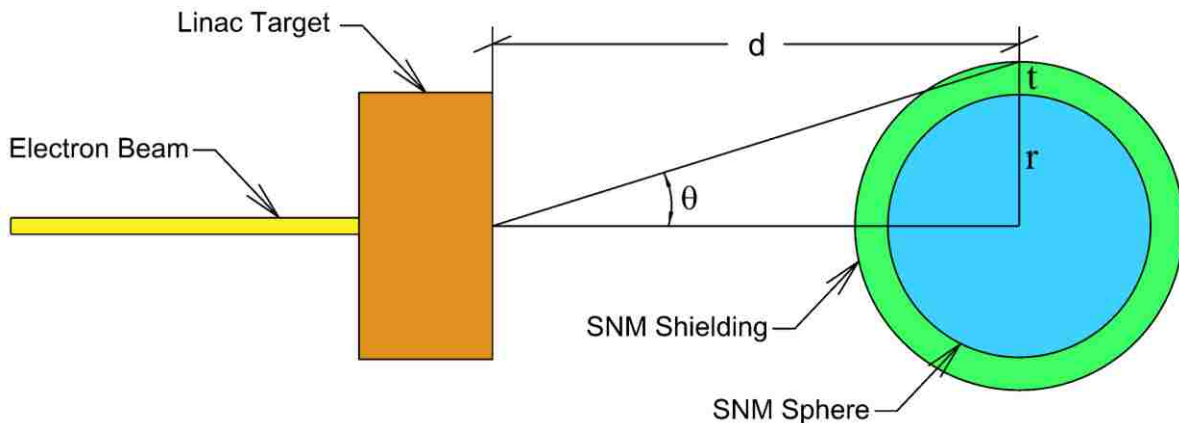


Figure 47. The photon SDEF

In order to ensure that the error associated with each energy bin of the bremsstrahlung spectra was below the 10% MCNP6 requirement, the NPS value was set to 500,000,000. The results of

the spectra for angles under 12° at a distance of 1 cm behind the linac target are shown in Figure 48.

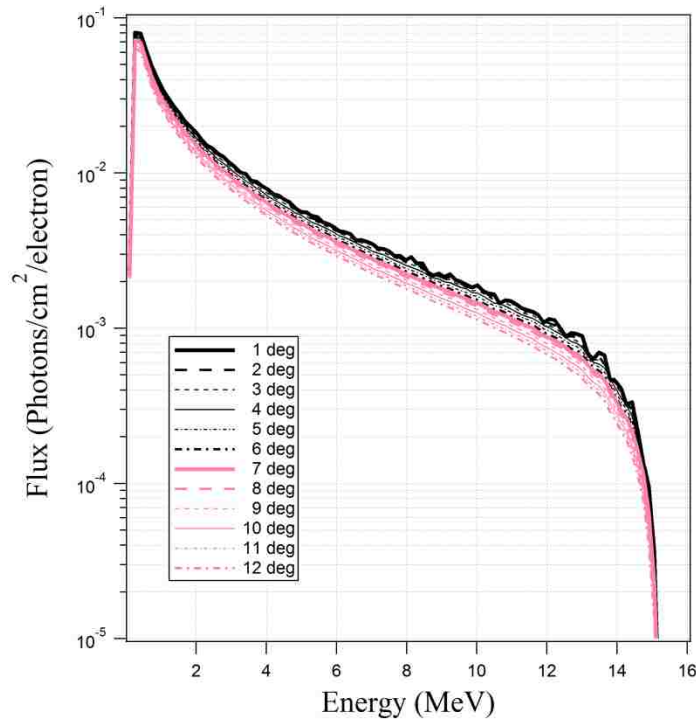


Figure 48. Bremsstrahlung spectra, 1 cm from linac

The computational results of the bremsstrahlung spectra generated from the electron beam MCNPX model were normalized to one starting electron. When these spectra are used as inputs for a separate MCNP input deck, the new results will be normalized to the starting particle used in that model, or one photon. In order to ensure that the new model is consistent in solving the original problem, it was necessary to determine the number of bremsstrahlung generated per electron in the first model. This number was found in the photon creation section of the MCNPX output file of the original model (Figure 49).

photon creation	tracks	weight (per source particle)	energy
source	0	0.	0.
nucl. interaction	0	0.	0.
particle decay	0	0.	0.
weight window	0	0.	0.
cell importance	0	0.	0.
weight cutoff	0	0.	0.
electron importance	0	0.	0.
dxtran	0	0.	0.
forced collisions	0	0.	0.
exp. transform	0	0.	0.
from neutrons	0	0.	0.
bremstrahlung	3389202772	6.7784E+00	3.3780E+00
p-annihilation	26066580	5.2133E-02	2.6640E-02
photonuclear	0	0.	0.
electron x-rays	2906734366	5.8135E+00	4.7045E-02
compton fluores	0	0.	0.
muon capt fluores	0	0.	0.
1st fluorescence	207651046	4.1530E-01	3.3598E-03
2nd fluorescence	0	0.	0.
(gamma,xgamma)	0	0.	0.
tabular sampling	0	0.	0.
prompt photofis	0	0.	0.
total	6529654764	1.3059E+01	3.4550E+00

Figure 49. MCNPX output - photon creation results

The ratio of generated bremsstrahlung to one starting electron in the original model was determined to be 6.7788. Since the new model results are normalized to one starting photon, the new tally results must be divided by this ratio in order to remain consistent across both models. This can be done by including a weight function ($1 / \text{ratio}$) in the SDEF card of the new MCNPX model, or can be divided from the tally results during post processing. The accuracy of the new photon source model was verified by comparing the photon flux result at an angle of 10° at 10 cm behind the target against those obtained by the original electron source model (Figure 50).

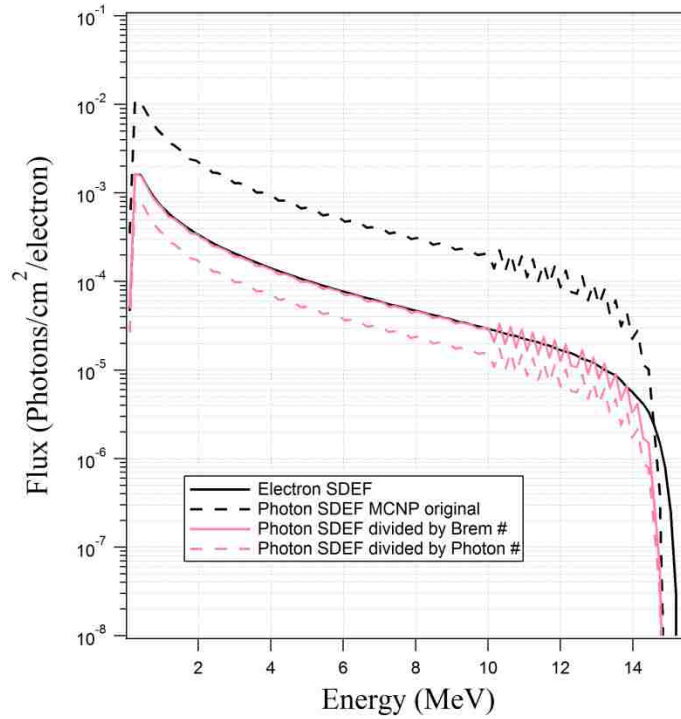


Figure 50. SDEF source check, 10 degree angle at 10 cm from source

The unmodified MCNPX results from the photon source model (dashed black line) were found to be larger than the results from the original electron source model (solid black line). When these results were individually divided by the ratio of bremsstrahlung generation to source electron (solid pink line), it was found that the modified results were nearly identical to the original results from the electron source model. The electron source term model took 2.82 days to run in MCNPX while the photon source term model took 2.34 hours. From this simple experiment, it was shown that the photon source term model provided nearly identical results to the original electron source term model, but ran 28.8 times quicker.

5.1.2 Modeling the active assay of SNM

The SNM interrogation model uses the K15 linac generated photon beam to probe 5 kg spheres of ^{235}U and ^{239}Pu (of various enrichments) at 1 meter from the linac. F4 tallies on thin concentric surfaces located 1 cm behind the shielded SNM were used to measure the angular distribution of neutrons produced during the irradiation process of the nuclear material. Again, photofission was enabled using the Lawrence Livermore National Lab (LLNL) model in the MCNP6 deck by setting the *fism* entry in the "Phys:p" card to 1 (from the default 0). The activation control (ACT) card controls the use of delayed fission products in the model (Figure 51).

```
c -----  
c Control delayed particle production  
act fission=n nonfiss=none dn=both dg=none  
c -----
```

Figure 51. ACT card example

Setting the *fission* entry equal to *n* enabled production of delayed neutrons, while setting the *nonfiss* equal to *none* ensures that no delayed particles will be produced according to non-fission reactions. The *dn* entry controls the delayed neutron data source with the *both* option specifying that delayed neutrons will use model physics when libraries are not available. Delayed gammas are controlled with the *dg* entry. Using line emission data requires this option set to *lines*, however this slows down the model immensely and was not used. In the model to determine the neutrons fluxes created by SNM assay, the *dg* card was set to *none*. The MCNP models were run with a *nps* value of 2E9 in order to minimize the relative error associated with each energy bin in the tallies.

Tally tagging was used to distinguish between prompt fission, delayed fission, and photonuclear produced neutrons. An example of the MCNP code used for tally tagging is seen in Figure 52.

```

c ----- Tally Tagging -----
f4:n 6000
e4 1e-3 50log 16
ft4 tag 3
fu4 92235.00018 92235.99999 92238.00018 92238.99999 1e10
c -----

```

Figure 52. Tally tagging example

The *tag a* card allows tracking of tally contributions based and how the particle was created. Setting *a* equal to 3 enables the production tag retention (tag is not lost) of particles in the models. The tally *FU* card were used to specify the bins of interest. Other than special tags, each tagging bin is of the form CCCCCZZAAA.RRRRR where CCCCC represents the cell number (optional), ZZAAA is the isotope identifier and RRRRR is the reaction number identifier. The 92235.00018 tag specifies prompt fission neutrons generated within ^{235}U while the 92235.99999 bin specifies delayed fission neutrons generated within ^{235}U . Special tags such as *-1* (allows for the tallying of source particles, if any) and *1e10* (creates an "everything else" bin that accounts for particles that contributed to the original tally but were not from those specified bins) may also be used.

5.2 Computational Results

MCNP6 Models were developed for the photofission assay of highly enriched uranium (90% enrichment in ^{235}U , 10% ^{238}U) and weapons grade plutonium (93% ^{239}Pu , 7% ^{240}Pu) for bare (without shielding) metal spheres as well as metal spheres surrounded by 5 cm poly shielding, 5 cm lead shielding, or a combination of the two (2.5 cm lead surrounded by 2.5 cm of

polyethylene). These cases were chosen as they represented high-Z and low-Z material (and a combination of the two) shielding material matrices. More studies (including alternate shielding materials and variable shielding thickness) can be undertaken in order to better understand photofission assay of SNM, but those chosen in this study were a representation of the typical materials. Neutron yield following the photon assay of a bare SNM metal sphere allows for determination of the neutron fluxes that occur due the (γ,f) and (γ,n) reactions within the SNM. The addition of shielding to the SNM sphere will alter this neutron environment. This is due to (γ,n) reactions occurring within the shielding materials in addition to those happening within the SNM metal (Figure 53). Additionally, shielding may attenuate the neutrons produced within the SNM sphere. Ultimately, the ratio of fission neutrons to total neutrons at 1 cm behind the SNM sphere will be affected by photon and neutron interactions with the shielding materials.

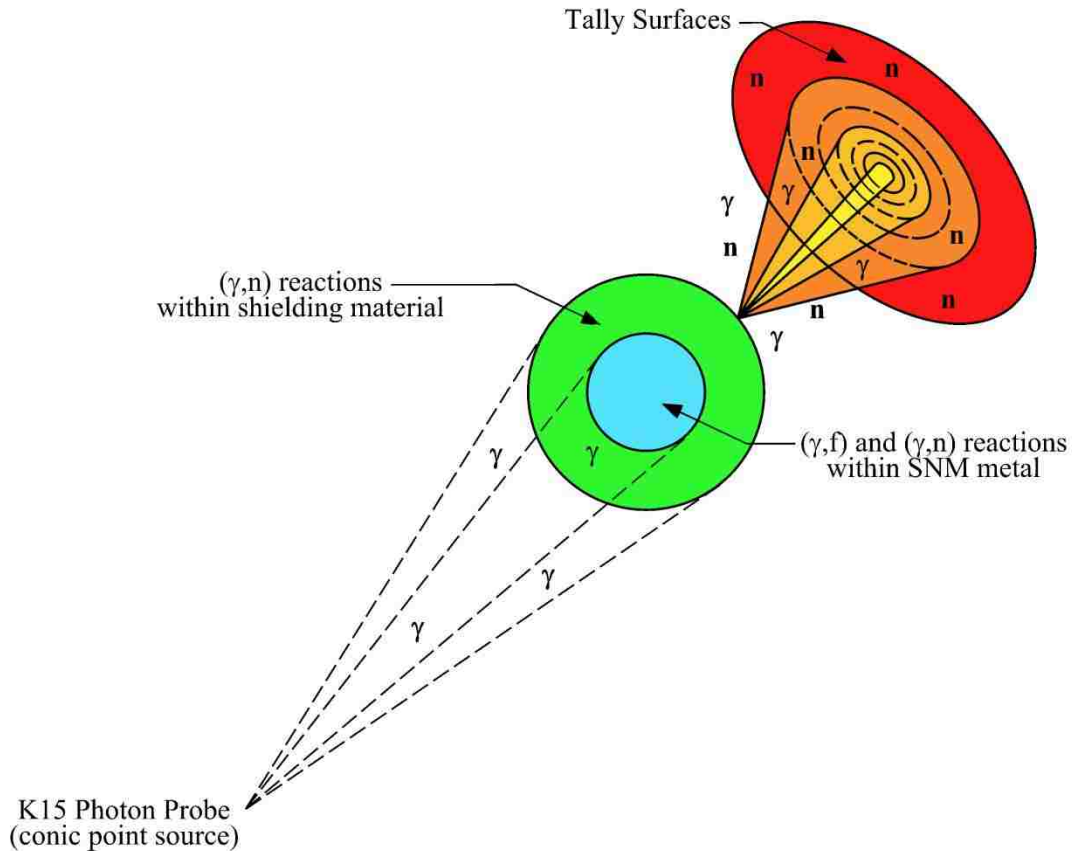


Figure 53. Reactions occurring during photofission assay of shielded SNM

5.2.1 Assay of Bare SNM

The F4 neutron tally results from the MCNP6 models of SNM without shielding represent the maximum fission neutron fluxes during the photon assay. Without shielding, the ratio of fission neutrons to total neutrons is highest due to the lack of photoneutron production within shielding materials. The likelihood of specific reaction induced by a photon (be it a photonuclear or photofission reaction) occurring within the SNM material's isotope is determined by the corresponding reaction cross section, which is energy dependent. The ENDF/B-VII.I photoabsorption cross sections [49] for uranium and plutonium are presented in Figure 54 and Figure 55.

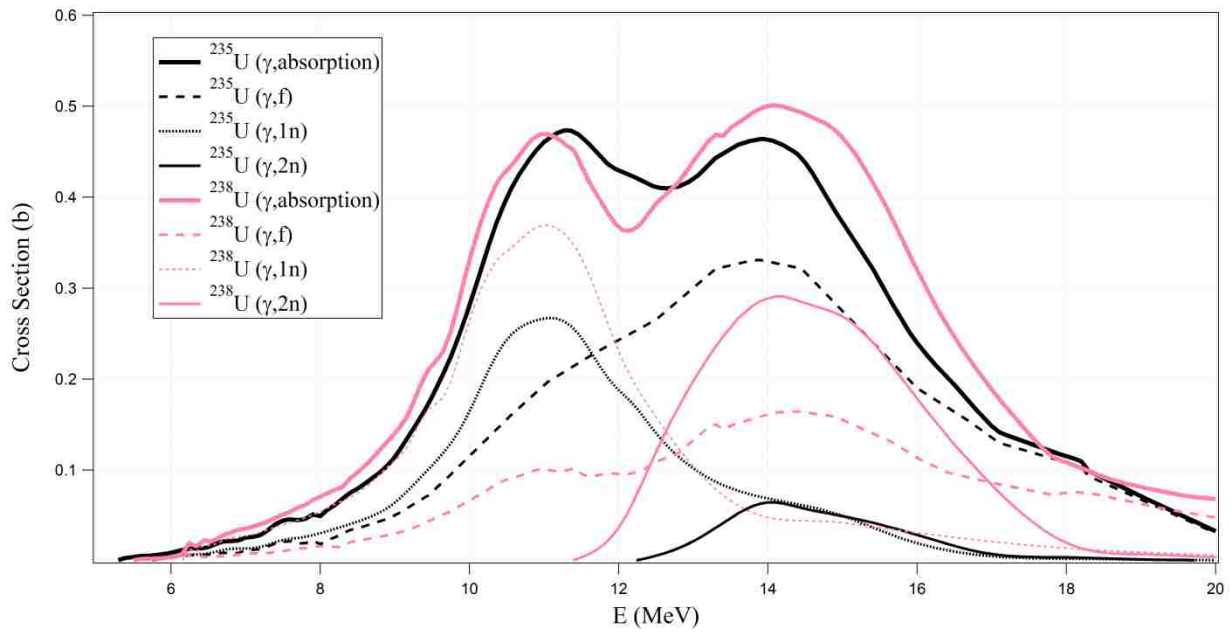


Figure 54. Uranium photoabsorption cross sections

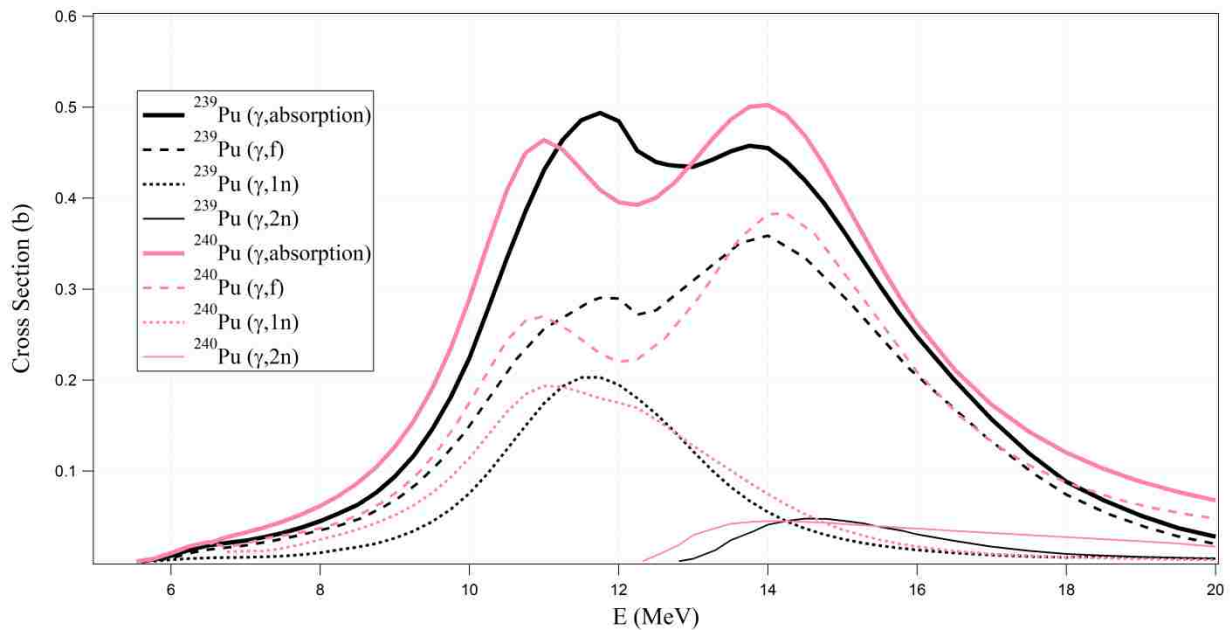


Figure 55. Plutonium photoabsorption cross sections

Near 15 MeV, the photofission cross section is largest for uranium and plutonium isotopes, enabling the maximum fission neutron production.

The MCNP6 models determined that the neutron fluxes produced during the photofission assay of bare plutonium metal were slightly larger than those produced during the photofission assay of bare uranium metal (Figure 56) due to plutonium having a larger density (19.84 g/cm^3) than uranium (19.1 g/cm^3).

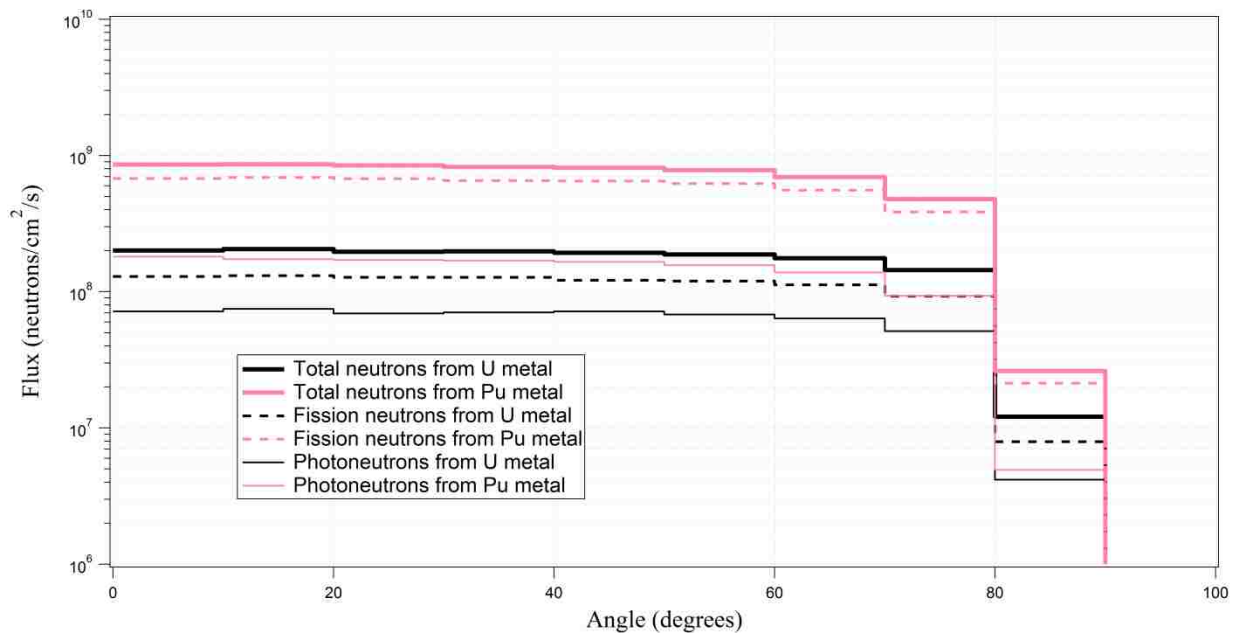


Figure 56. Neutron fluxes during assay of bare weapons grade SNM

The fluxes of total (prompt fission plus delayed plus photonuclear), fission (prompt plus delayed) and photonuclear neutrons were consistent across all angular intervals for both SNM types, with the exception of a noticeable decrease, at angles larger than 80° . It was determined that just behind (1 cm) the SNM spheres, the total neutron (fission plus photonuclear) flux is expected to reach about 9×10^8 and 2×10^8 neutrons/cm²/s for bare spheres of weapons grade plutonium and highly enriched uranium, respectively. The fluxes of delayed neutrons were

found to be as expected, less than 1% of the fluxes of prompt neutrons for both isotopes of uranium and plutonium.

5.2.2 Assay of Shielded SNM

The effect of shielding materials on the neutron yield produced during the photofission assay of SNM was investigated. It was determined that the presence of lead shielding surrounding the SNM metal reduced fission neutron fluxes at 1 cm behind the spheres by two orders of magnitude and total photoneutron fluxes by one order of magnitude (Figure 57).

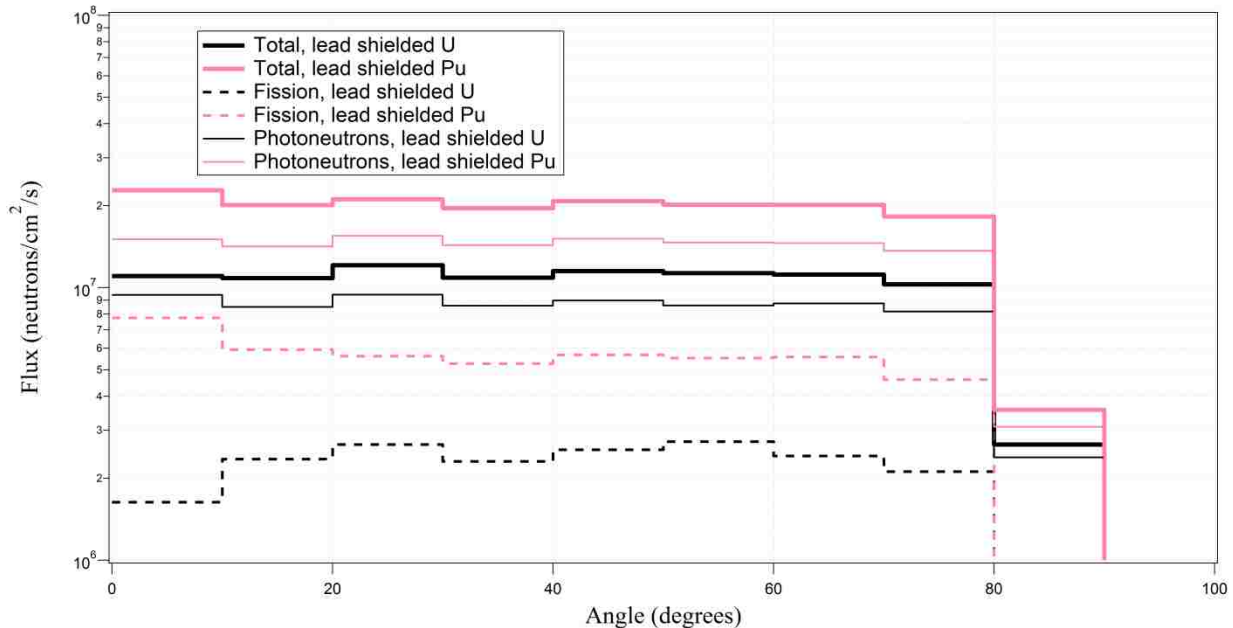


Figure 57. Neutron fluxes during assay of lead shielded weapons grade SNM

High-Z materials (such as lead) reduce the number of photons (attenuate) in the probe beam. The computed bremsstrahlung spectra at 1 m were determined using F4 tallies on the plutonium spheres for unshielded and lead shielded configurations (Figure 58).

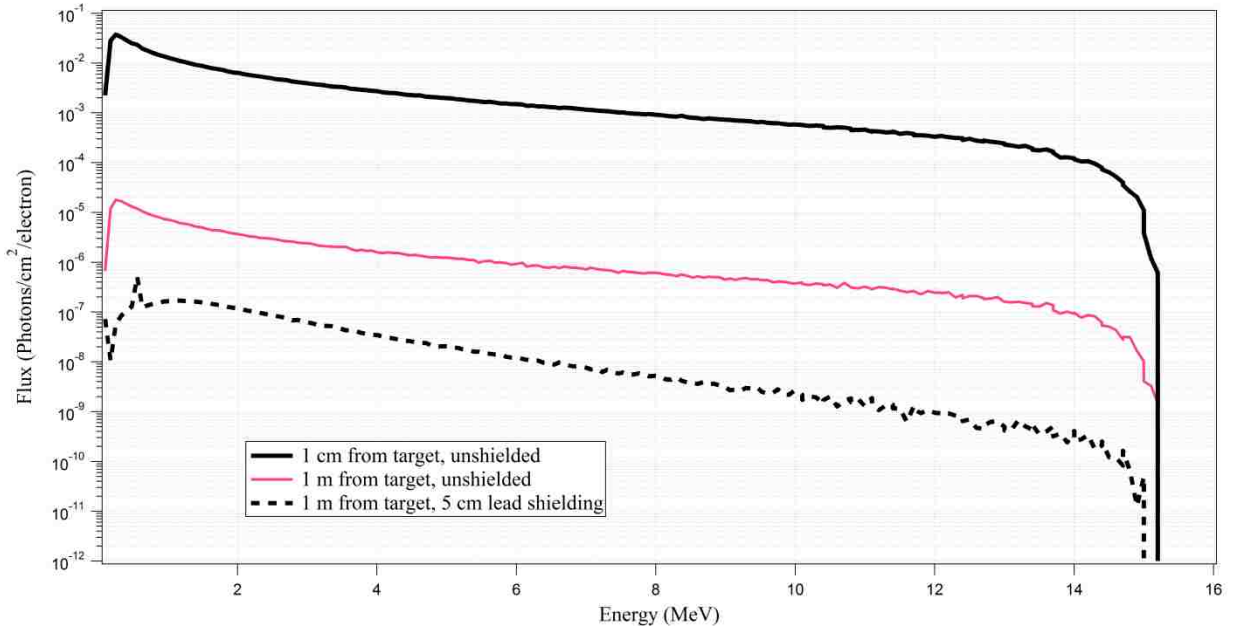


Figure 58. Bremsstrahlung spectra at 1 meter from K15 linac

It was determined that at 1 m, the probe's photon fluxes were reduced by more than three orders of magnitude comparing to the 1 cm distance. When 5 cm of lead shielding was used, the flux decreased by additional two orders of magnitude. Additionally, photoneutrons were produced within the lead shielding as well.

The effect of polyethylene shielding on the neutron environment during the photofission assay of SNM was investigated as well. The neutron fluxes at 1 cm behind the polyethylene shielded SNM metals are shown in Figure 59. It was determined that the neutron fluxes following the high-energy photon assay of polyethylene shielded SNM were lower than during the assay of bare SNM, but higher than during the assay of lead shielded SNM.

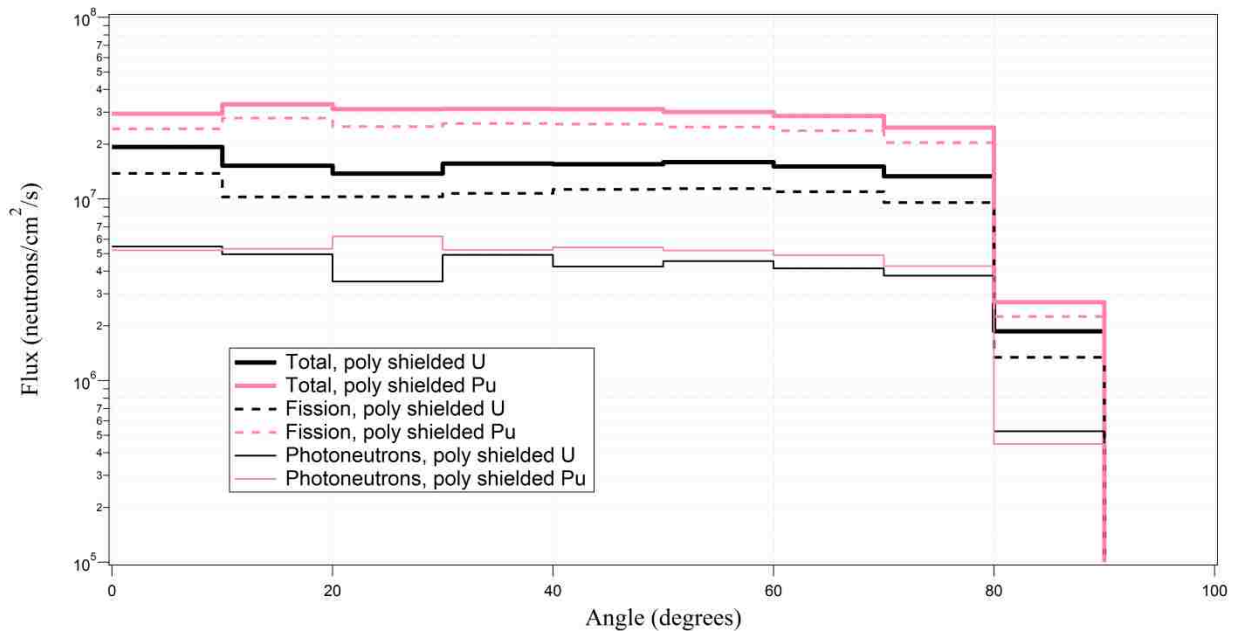


Figure 59. Neutron fluxes during assay of polyethylene shielded weapons grade SNM

The isotopes in polyethylene have total absorption cross sections two orders of magnitude lower than those the isotopes found in natural lead (Figure 60). As a result, less photoneutrons were produced by (γ,n) reactions in polyethylene shielding than in lead shielding of the same thickness.

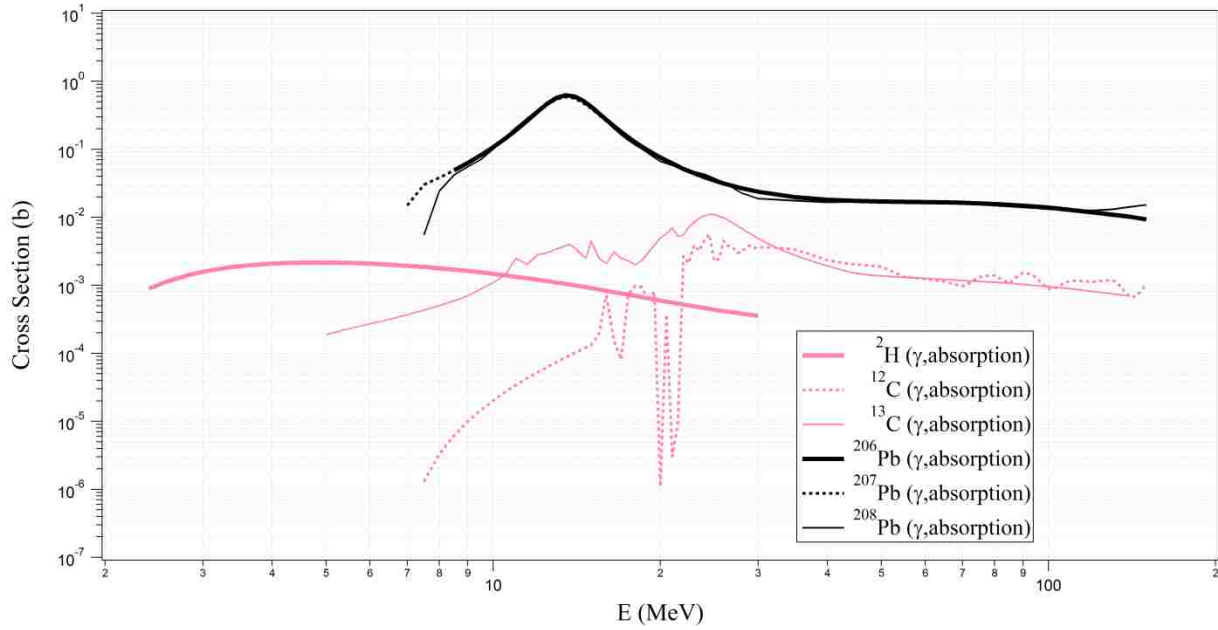


Figure 60. Photonuclear cross sections for shielding materials

Furthermore, polyethylene shielding does not effectively reduce the number of photons in the radiation probe. The fission neutron fluxes at 1 cm behind poly shielded SNM were not reduced to the levels found by lead shielded SNM. However, these neutron fluxes were lower than non-shielded SNM due to interactions with the polyethylene shielding.

Neutron fluxes were also determined for a combination of the two shielding materials (Figure 61). This combination consisted of a 2.5 cm thick lead inner layer and a 2.5 cm thick polyethylene outer layer.

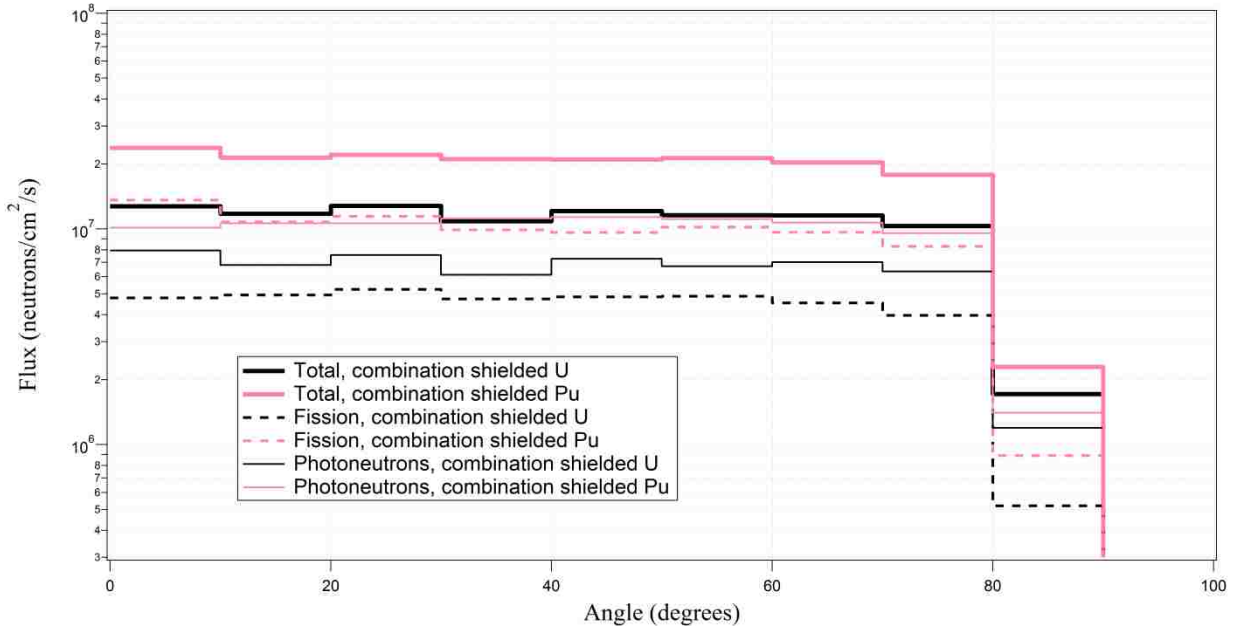


Figure 61. Neutron fluxes during assay of lead and polyethylene shielded weapons grade SNM

The modeling results obtained for such example of dual material shielding were found to be similar to those obtained from the models with only one material. It was found that the angular variation of neutron fluxes was minimal (aside from angles greater than 80°) and that neutron fluxes during the assay of plutonium metal were larger than those of uranium metal. Total neutron fluxes when both lead and polyethylene shielding was used were found to be larger than when lead shielding alone was used but less than when polyethylene alone was used.

In order to properly understand the effects of shielding material on the neutron environment following the high-energy photon assay of SNM, a comparison of the fluxes of total (Figure 62) and fission (Figure 63) neutrons across all models was made. Additionally, the fraction of fission neutrons to total neutrons was computed (Figure 64).

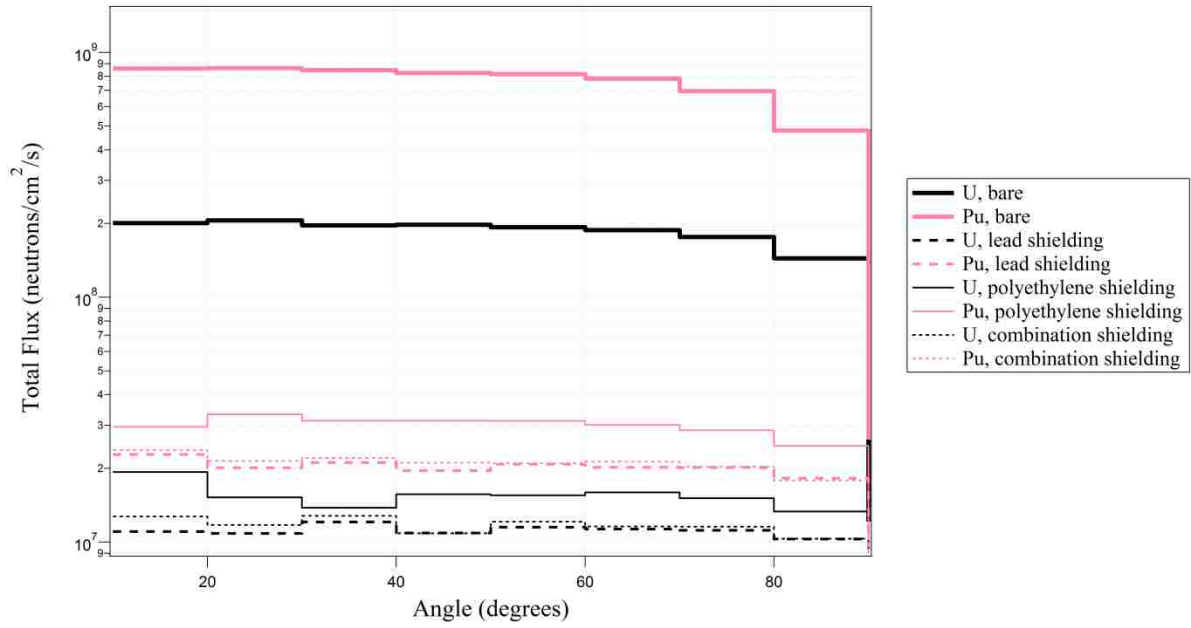


Figure 62. Total neutron fluxes for photon assay of SNM

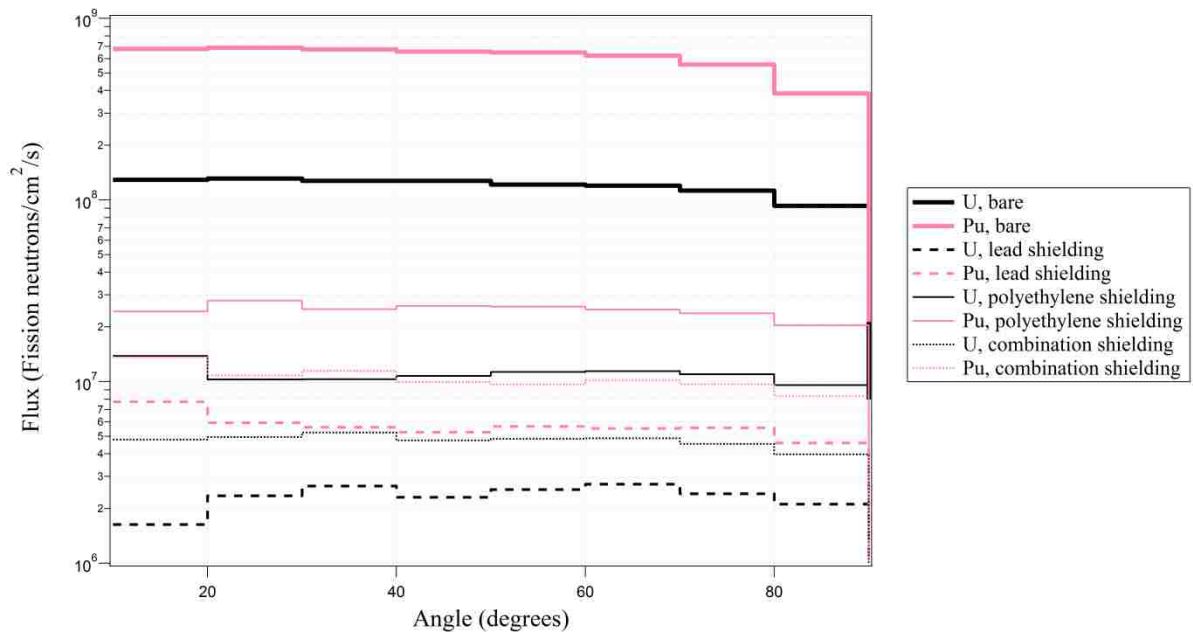


Figure 63. Fission neutron fluxes for photon assay of SNM

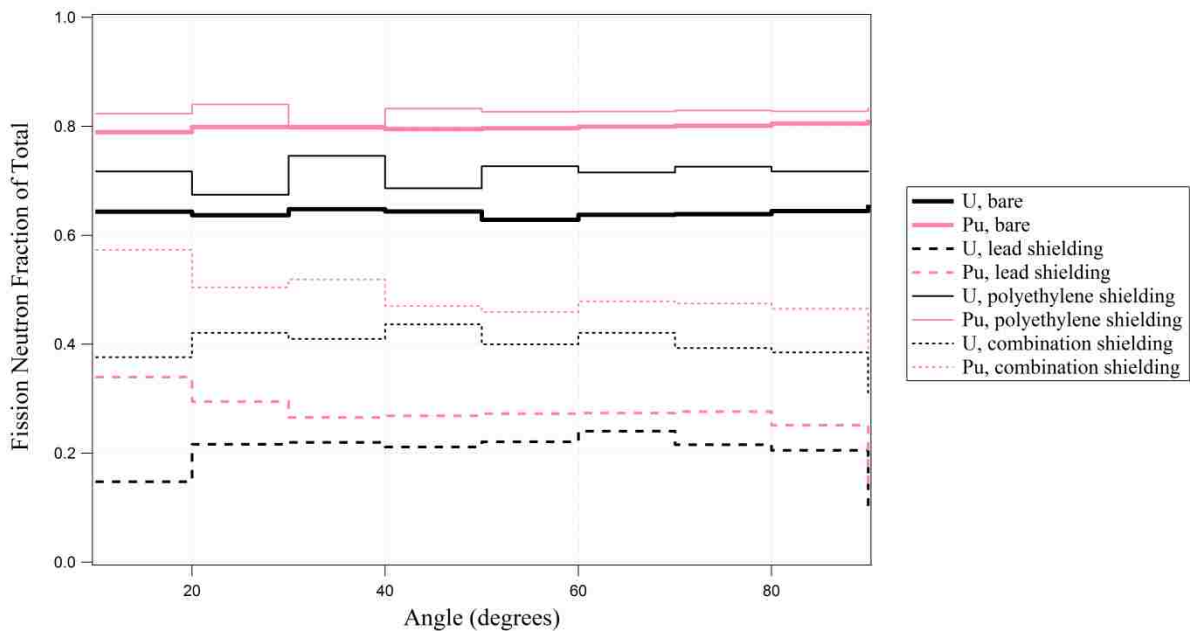


Figure 64. Fraction of fission neutrons at 1 cm behind SNM

It was found that the total neutron fluxes were largest when the photon assay was performed on a bare SNM metal. The results showed that the presence of the considered shielding materials reduced the total neutron flux by at least an order of magnitude for both uranium and plutonium metals. However, the angular distribution of total neutron fluxes varied by less than an order of magnitude between shielding material types. When the Varian K15 linac is used to perform the photon assay on 5 kg of shielded weapons grade SNM, the expected total neutron flux at 1 cm behind the material range is between 10^7 to 10^9 neutrons/cm²/second.

The presence of shielding material surrounding the respective SNM metals reduces the flux of fission neutrons behind the SNM metals by up to two orders of magnitude, depending on the shielding material used. The range (maximum to minimum) of the fluxes of fission neutrons varies by almost three orders of magnitude. It was shown that while the fission neutron fluxes vary between the different shielding materials, they do not vary significantly with the angle. It

was determined that the K15 linac will produce fission neutrons at 1 cm behind shielded SNM materials within the flux range between 10^6 and 10^9 neutrons/cm²/s, depending on the shielding material present.

The fraction of fission neutrons across all angles was approximately constant for each individual assay scenario. The fission neutron fraction varied between the individual scenarios due to varying numbers of photoneutrons produced within the shielding materials. The results showed that shielding material type affects the fraction of fission neutrons produced during the photon assay of SNM.

5.2.3 Enrichment effects

The effect of the enrichment (by ²³⁵U and ²³⁹Pu isotope) on the neutron yield following the photon assay of SNM was investigated for both uranium and plutonium metals. The MCNP6 models were run with varying SNM enrichment (from 0% to 100%, in 25% increments) in order to determine the fluxes of neutrons produced through the (γ ,f) and (γ ,n) reactions. For angles between 70° and 80°, the total neutron flux, the fission neutron flux and the fission neutron fraction were determined (shown in Figure 65 through Figure 67).

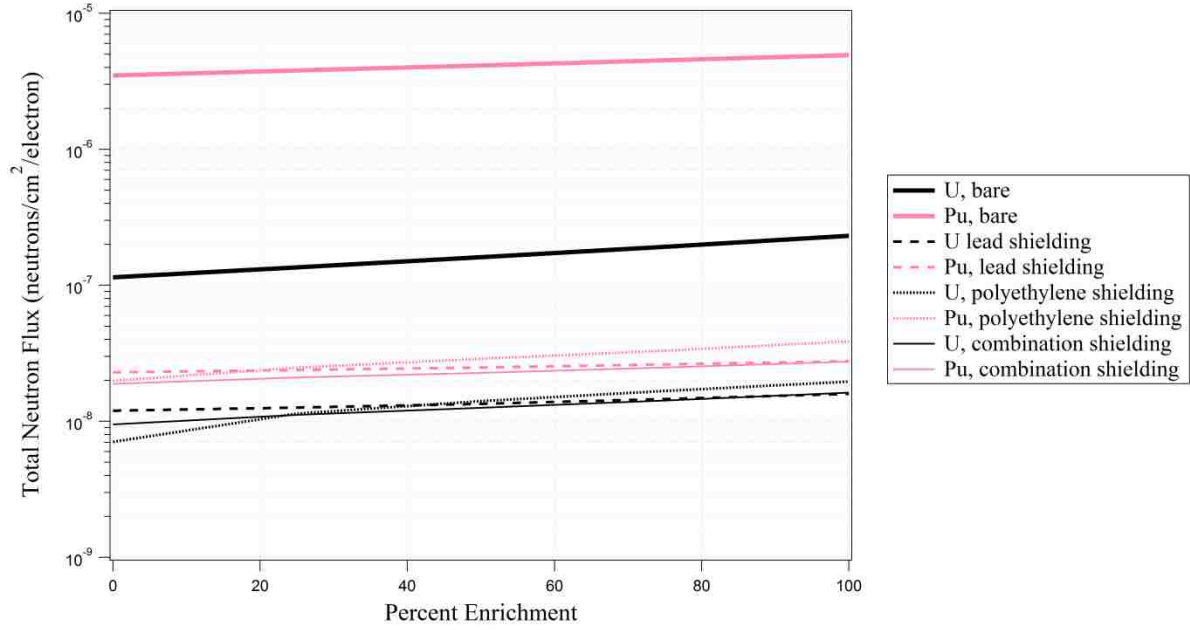


Figure 65. Enrichment effects on the total neutron flux

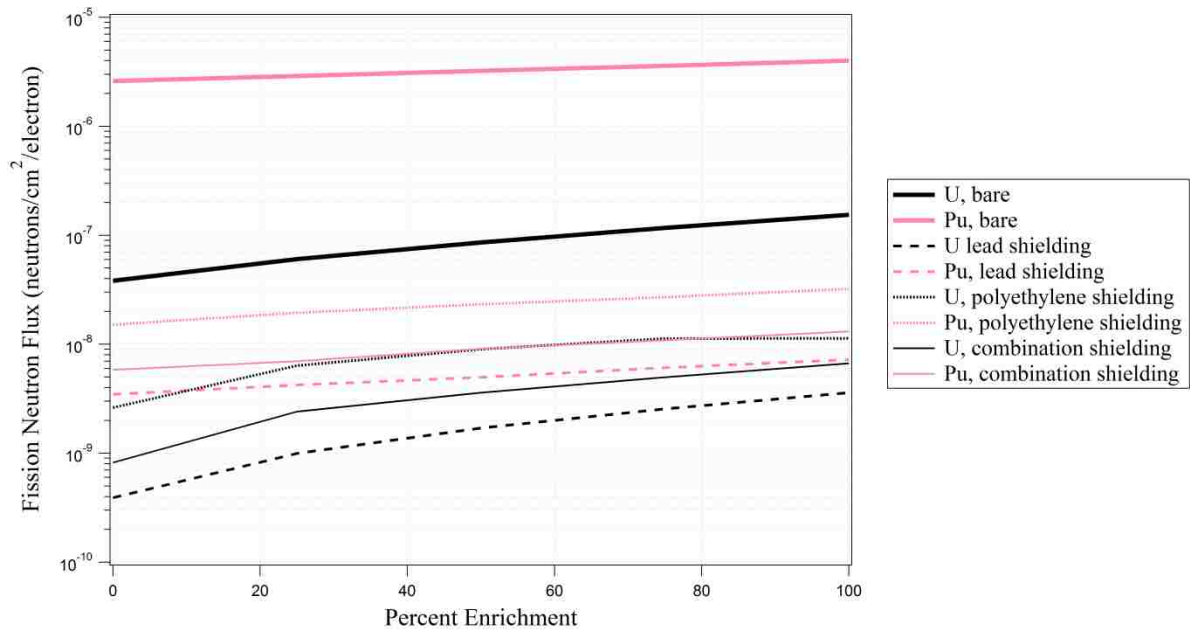


Figure 66. Enrichment effects on the fission neutron flux

The results showed that as the enrichment (^{235}U and ^{239}Pu) in the SNM metals increased so too did the fluxes of fission neutrons and photoneutrons for the considered metals and shielding

materials. The largest increase in total neutron flux due to an increase in the enrichment (from 0 to 100%) was found to be for uranium shielded by polyethylene (136%) while the smallest increase was found to be for plutonium shielded by lead (21%). Similarly, the largest increase in fission neutron flux was found for a lead shielded uranium sphere (818%) while the smallest increase was for a bare plutonium sphere (53%). The average fission neutron flux increase (320%) was found to be greater than the average total neutron flux increase (68%).

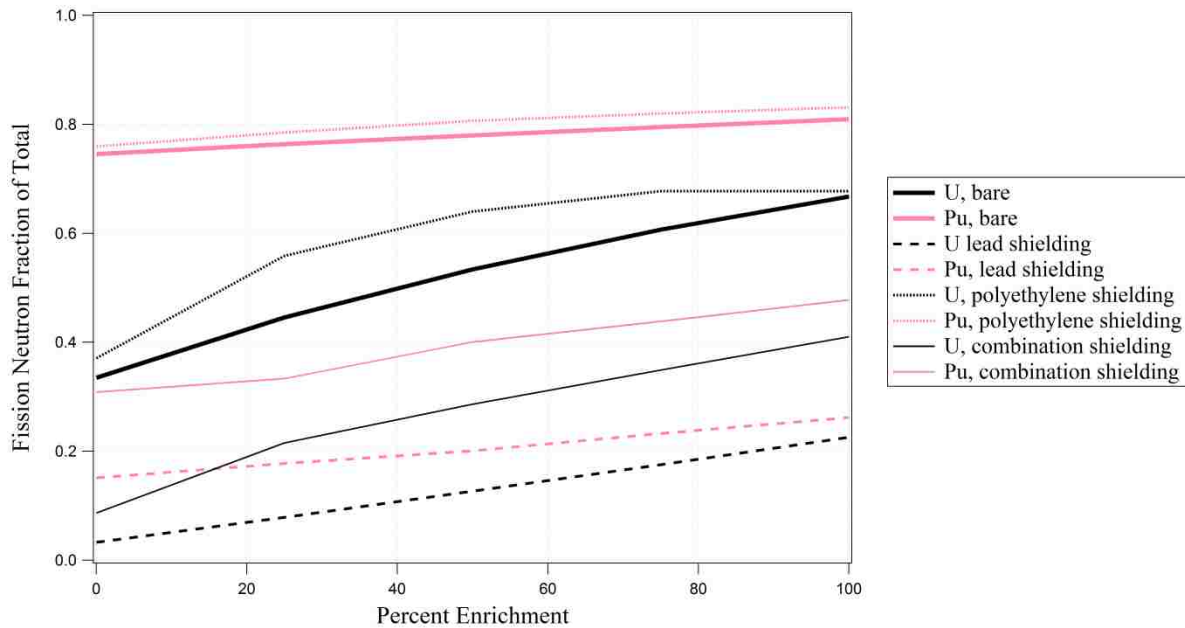


Figure 67. Enrichment effects on the fission neutron fraction

It was determined that as the SNM enrichment increased, the fraction of fission neutrons increased as well. The largest increase was found for a bare uranium metal (33%) while the smallest increase was found for a bare plutonium metal (6%).

5.2.4 Neutron Spectra

The total, photofission and photonuclear neutron spectra were determined within each angular interval for each SNM assay model. Using the tally tag cards with the logarithmic energy binning on each of the F4 tally surfaces, the individual neutron spectra were computed at each angle for each MCNP6 model. The computed neutron spectra at 1 cm behind the SNM, at angles between 70° and 80°, for uranium without shielding (Figure 68), with polyethylene shielding (Figure 69), with lead shielding (Figure 70) and a combination of the two (Figure 71) were calculated and are shown for example.

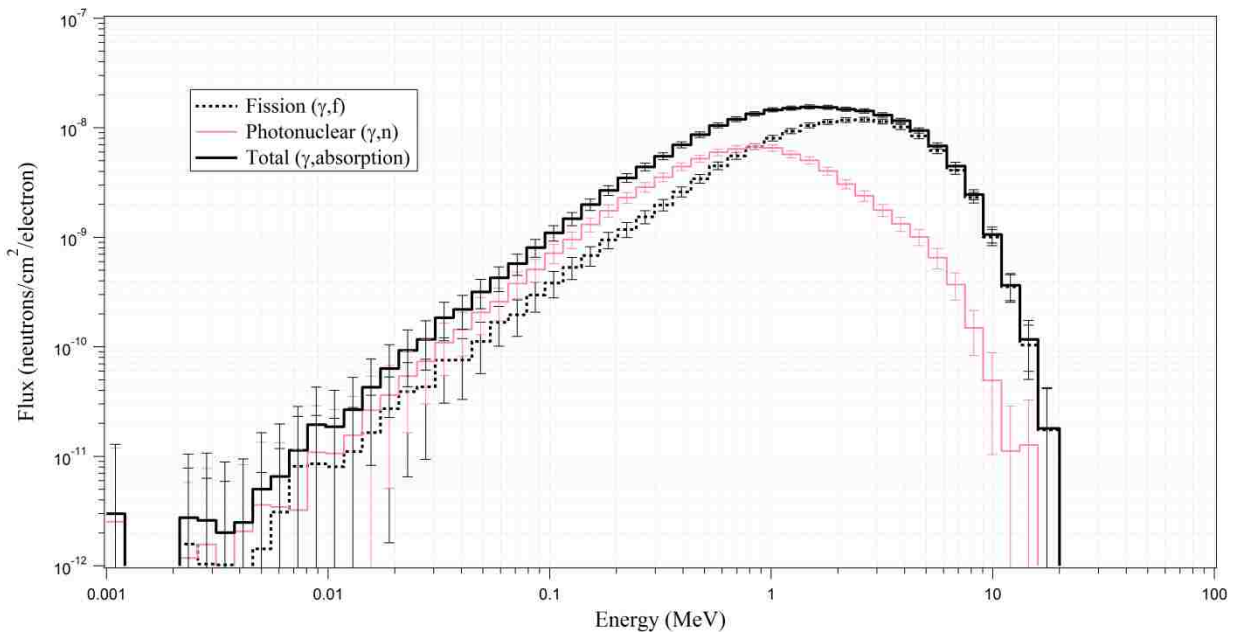


Figure 68. Spectra of neutrons generated during photon assay of unshielded uranium

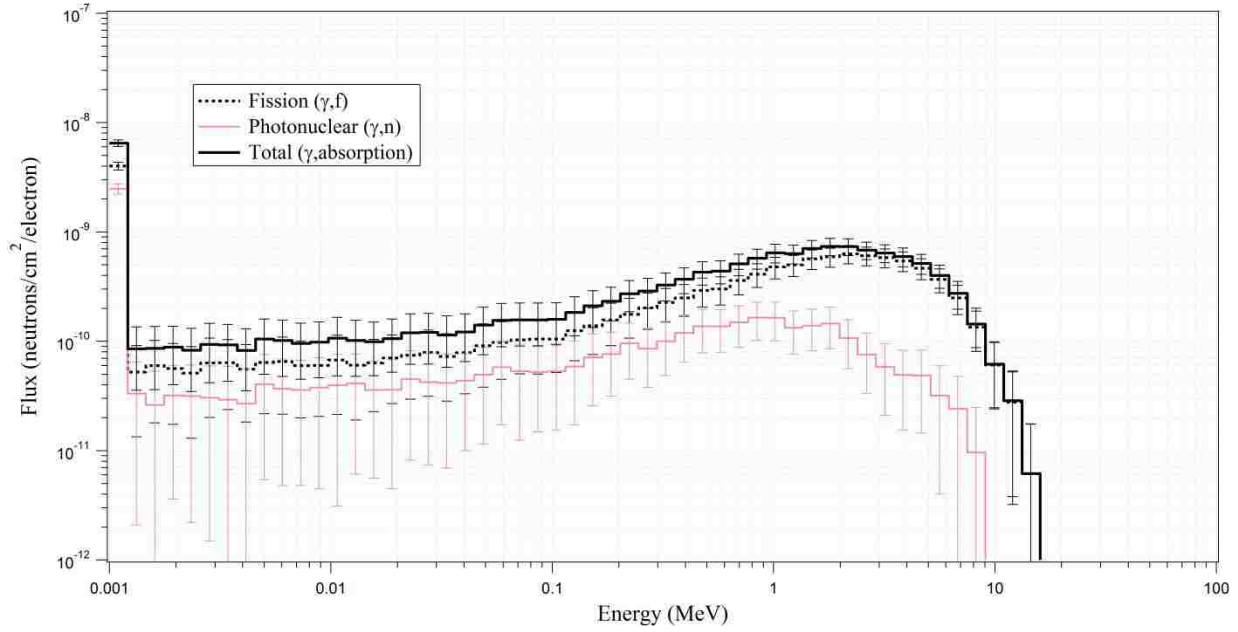


Figure 69. Spectra of neutrons generated during photon assay of uranium with 5 cm polyethylene shielding

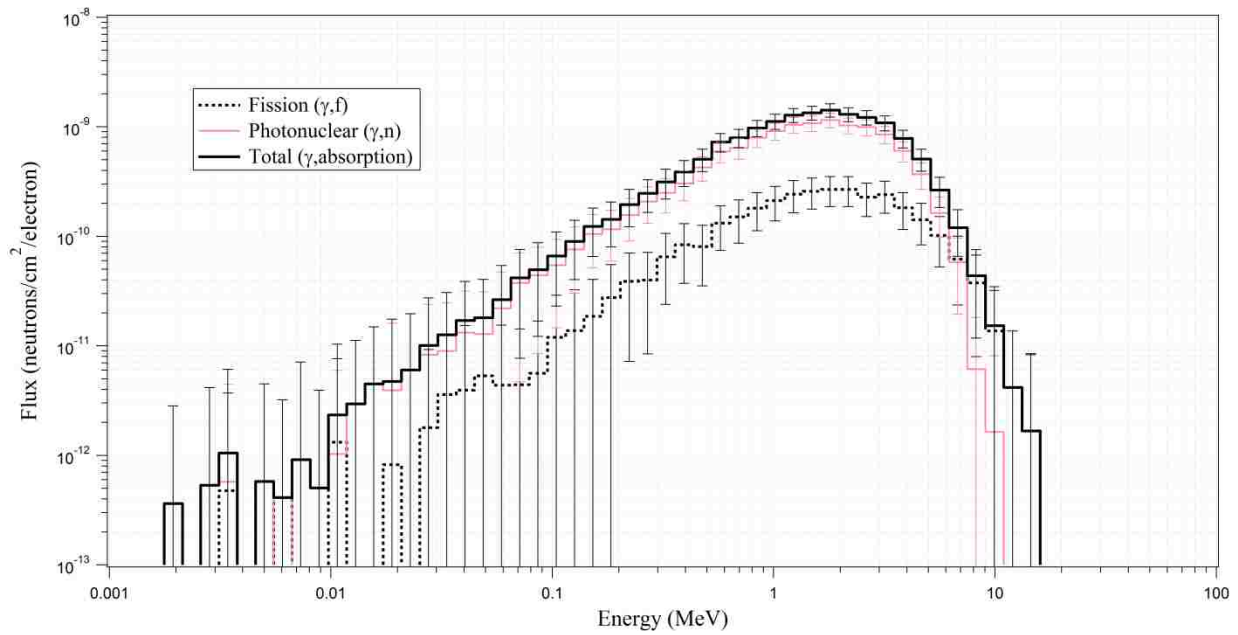


Figure 70. Spectra of neutrons generated during photon assay of uranium with 5 cm lead shielding

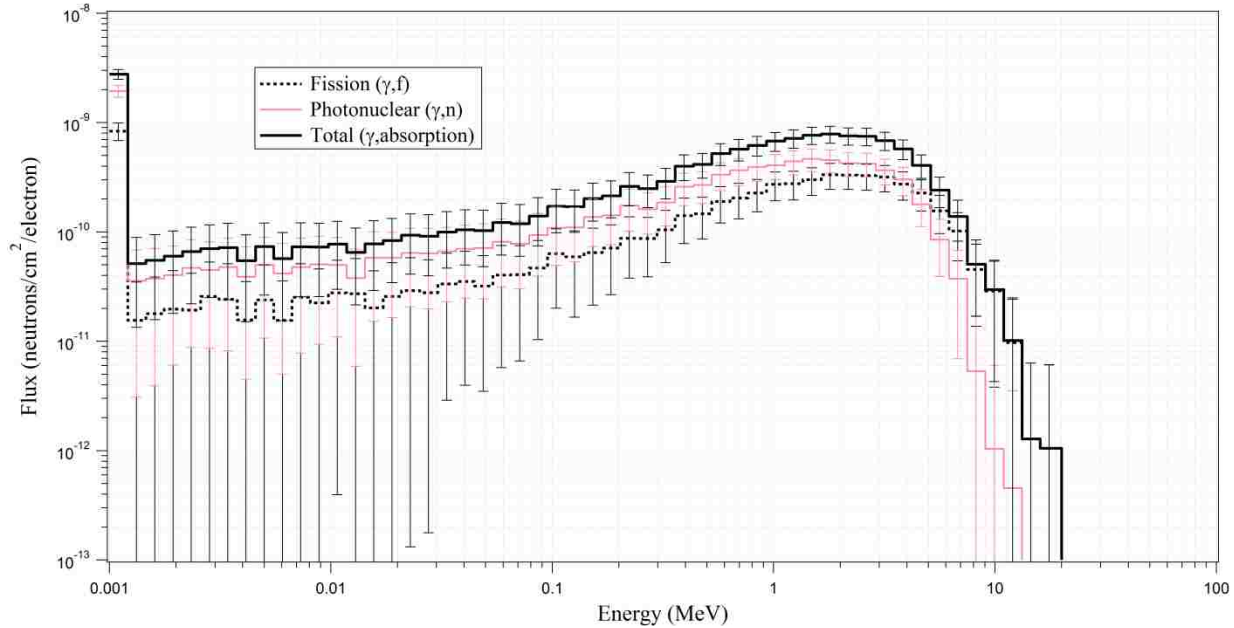


Figure 71. Spectra of neutrons generated during photon assay of uranium with 5 combination shielding

Neutron spectra at 1 cm behind the SNM spheres were computed for angles between 70° and 80° for weapons grade plutonium without shielding (Figure 72), with polyethylene shielding (Figure 73), with lead shielding (Figure 74) and a combination of the two (Figure 75). When the SNM is surrounded by 5 cm of polyethylene shielding, the resulting neutron environment contains greater quantities of fission neutrons than photoneutrons. Conversely, the opposite is true when SNM was shielded by 5 cm of lead. This is due to lead having a $(\gamma, \text{absorption})$ cross section two orders of magnitude larger than the polyethylene components (carbon and hydrogen). When both lead and polyethylene were used as the shielding, it was found that for neutron energies below 6 MeV, the photoneutron fluxes were larger than the fission neutron fluxes. However, the difference between the two fluxes was not as large as when the lead shielding alone was used. At neutron energies higher than 6 MeV, the fission neutron fluxes were larger than photoneutron fluxes.

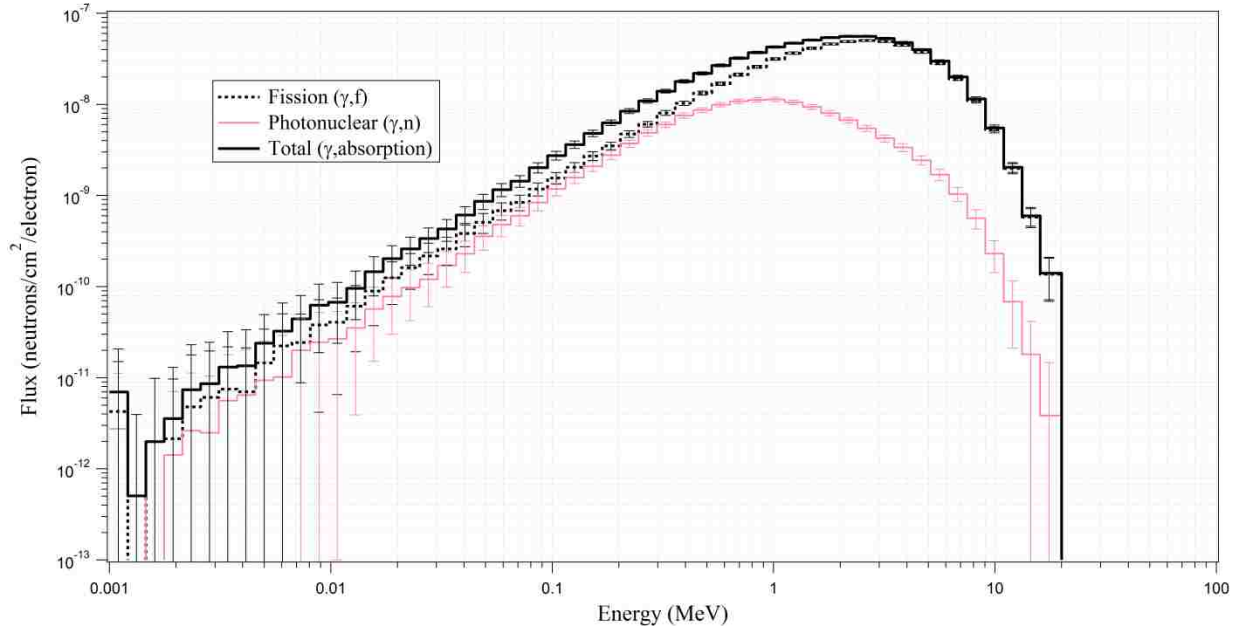


Figure 72. Spectra of neutrons generated during photon assay of unshielded plutonium

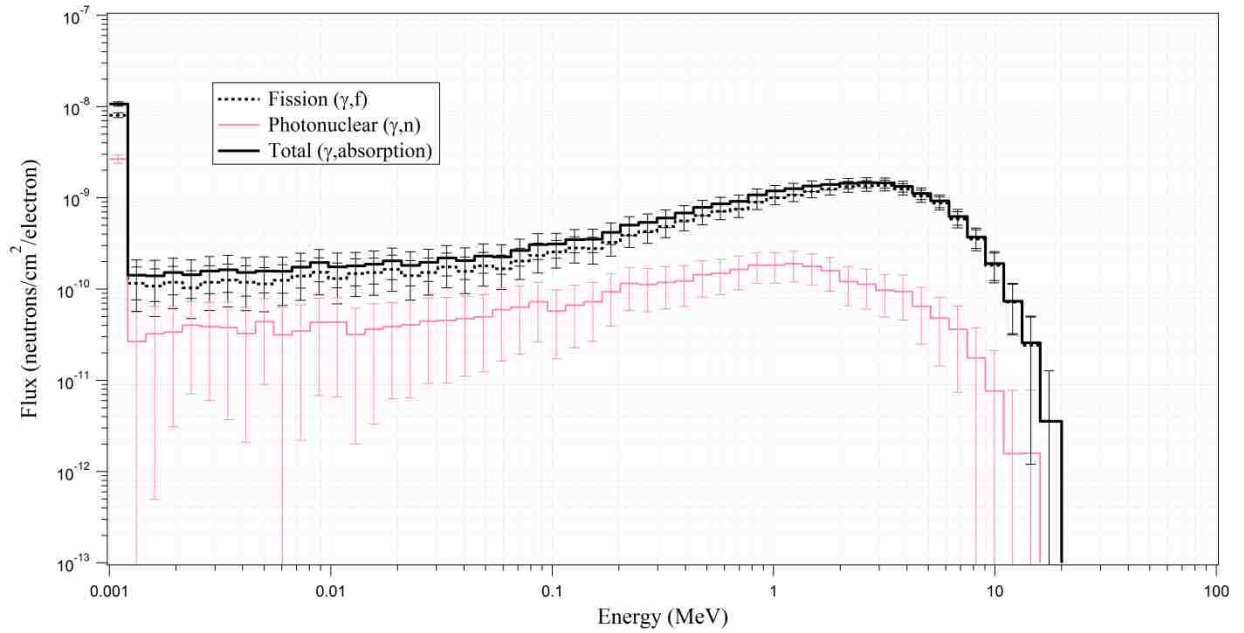


Figure 73. Spectra of neutrons generated during photon assay of plutonium with 5 cm polyethylene shielding

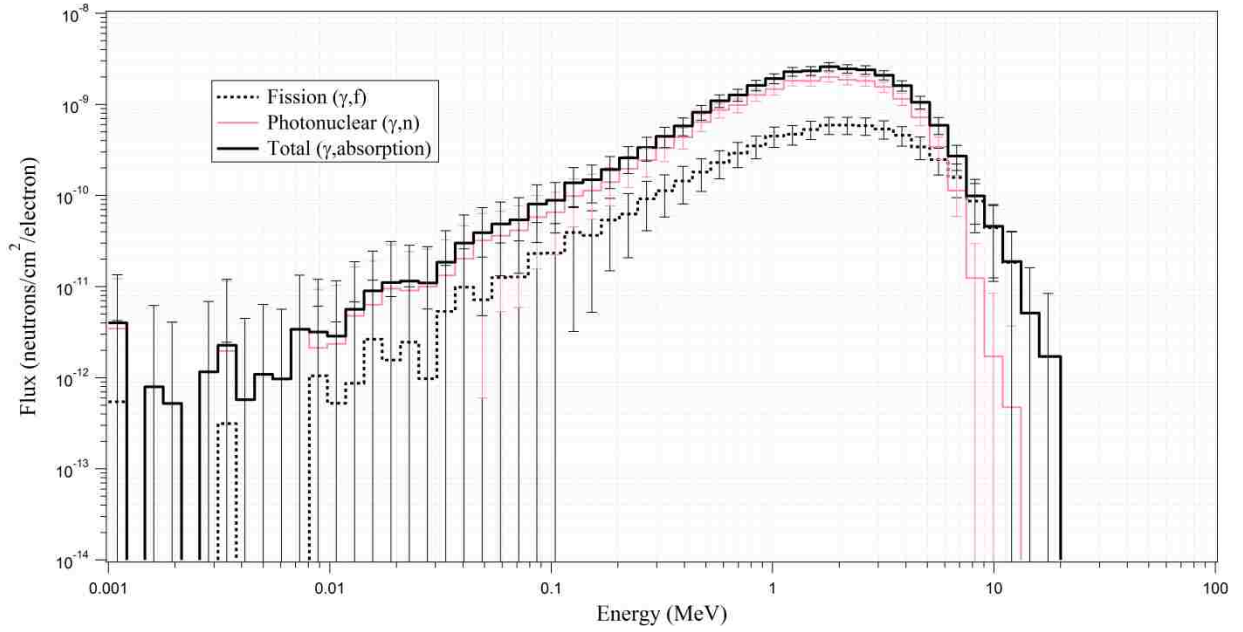


Figure 74. Spectra of neutrons generated during photon assay of plutonium with 5 cm lead shielding

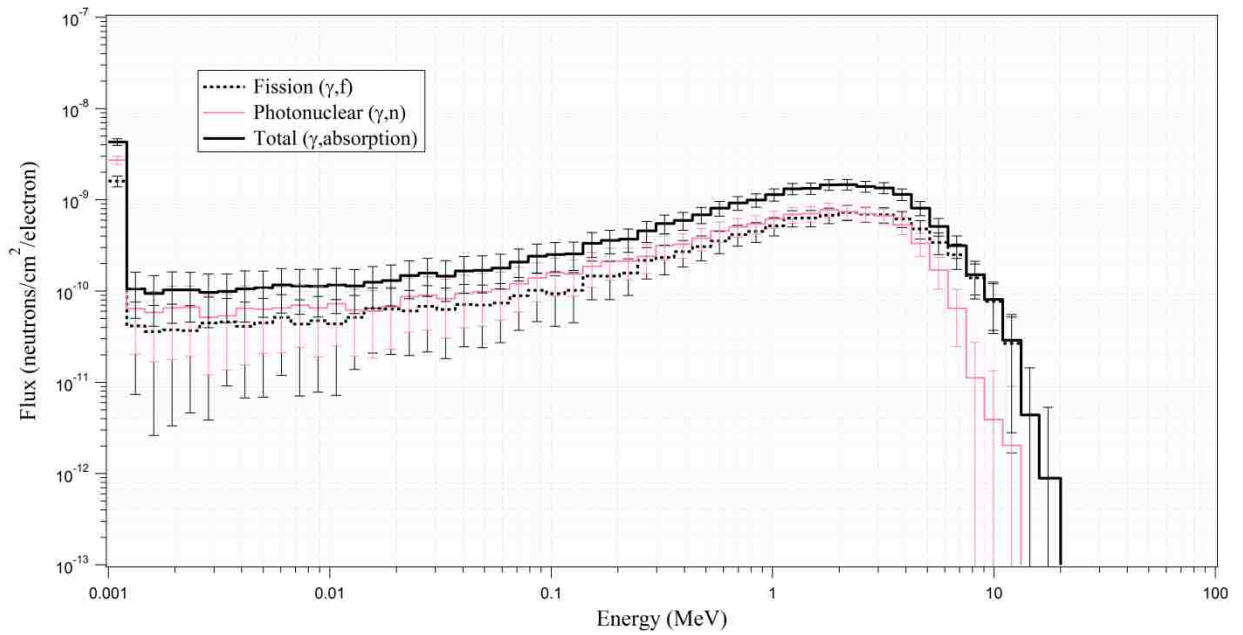


Figure 75. Spectra of neutrons generated during photon assay of plutonium with 5 cm combination shielding

5.2.4 Photon Spectra

While the detection of photons produced during the SNM fission is beyond the scope of this study, the photon fluxes at 1 cm behind the shielded SNM sphere were determined for several scenarios in order to evaluate the total radiation environment created during the photon assay of SNM. The photon spectra for the weapons grade plutonium photon assay with lead shielding computed for at angle between 70° and 80° of are shown in Figure 76.

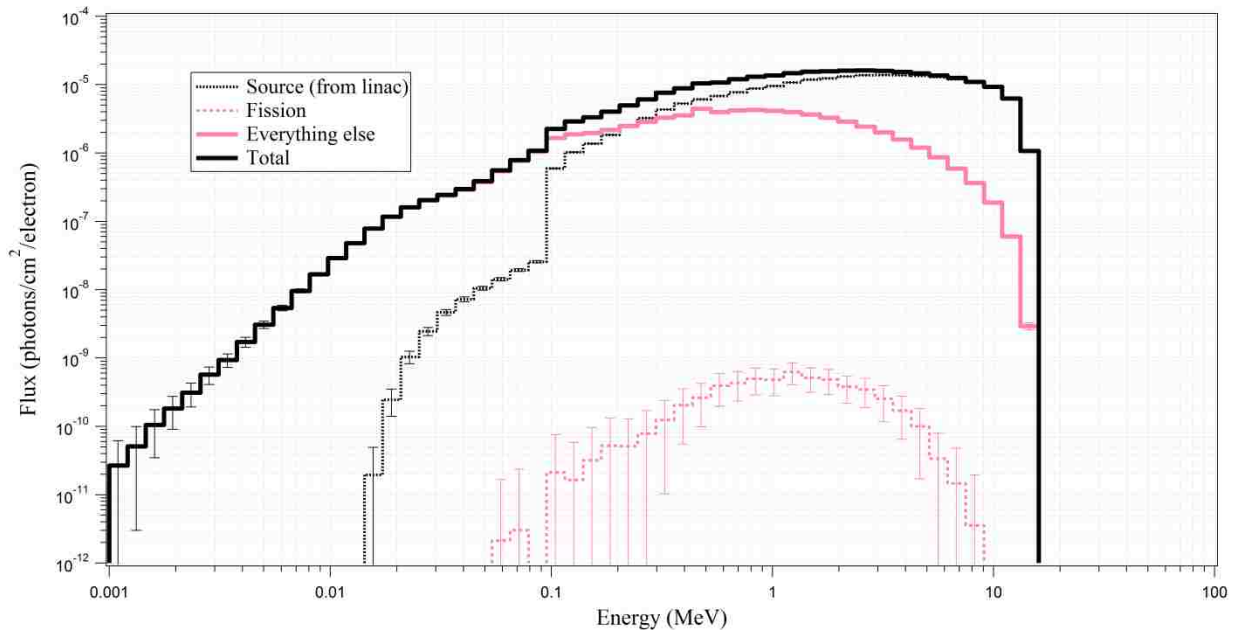


Figure 76. Spectra of photons generated during photon assay of plutonium with polyethylene shielding

The photons with the largest fluxes were found to originate from the linac photon probe. The fission photons have fluxes 4-5 orders of magnitude lower than the other photons types. When the K15 linac was used as a photon probe for the assay of shielded SNM, the resulting neutron production consisted of both fission and photonuclear neutrons, in varying fraction depending on the enrichment of the SNM, and the shielding material used. The use of a polyethylene shielding

around the weapons grade plutonium metal resulted in a neutron environment with the largest percentage of fission neutrons (greater than 80%) whereas the use of lead and polyethylene shielding around uranium yielded the lowest (20%). In order to identify the presence of SNM during the assay of an unknown quantity of material, it is necessary to detect prompt fission neutrons. It is helpful to use neutron multiplicity in order to distinguish between neutrons created through fission and those created through other photonuclear reaction.

Chapter 6: Neutron Detection

In order to achieve nuclear security and safeguard goals, neutron detection needs to be reliable and accurate. Neutrons are detected by their interaction with a detector medium, resulting in the production of an electric signal that provides information about the incident neutron's energy, magnitude and temporal flux characteristics. Whereas moderated ^3He detectors were once considered the detection standard due to their ability to identify thermal neutron sources, several disadvantages have led to the need for the alternative detector developments. A renewed interest in security efforts has led to increased demand for ^3He , resulting in the inflated cost and isotope shortages [107, 108]. Additionally, ^3He detectors require the neutron moderation (slowing down) prior to the detection. Moderating materials are combined with ^3He detectors in order to slow down neutrons to the thermal energy range, where the reaction cross sections are large enough that they may undergo such nuclear reaction and ultimately be detected. An alternative to ^3He gaseous detectors, scintillator detectors do not require the moderation of a neutron before detection and as such, allow the detection of fission neutrons in their natural energy range [109]. In addition to the ability to detect fast neutrons, scintillator detectors typically have quicker response times than gaseous detectors and are able to be used in high count rate environment. Finally, if multiple scintillator detectors are used, time correlation analysis is possible due to the ability to measure the fast neutron's temporal information.

6.1 Scintillator Detectors

When the incident radiation interacts with the scintillator material, atomic electrons become excited and ultimately release photons during the de-excitation processes [110]. The main reactions occurring within the plastic material are the scattering reactions on the hydrogen and carbon atoms. This recoiling proton ionizes the scintillator material, resulting in the production of light. Depending on the energy of this recoiling proton, several other reactions may occur, resulting in the production of deuterons, tritons, and alpha particles. The produced scintillation photons are converted into electrons that are amplified through a series of dynodes and converted into a current signal through use of an optically coupled photomultiplier tube (PMT) or silicone PMT. Ultimately the number of photons generated by the scintillation process is proportional to the energy of the incident radiation that passed through the scintillator.

For this study, the Eljen Technology's EJ-299-33A plastic scintillator was evaluated [111]. The scintillator (shown in Figure 77) is composed of a combination of fluorescent dye compounds 2,5-diphenyloxazole and 9,10-diphenylanthracene mixed with a polyvinyl toluene matrix [112].



Figure 77. EJ-299-33A plastic scintillator

White teflon tape was used to wrap the plastic scintillator (acting as a reflector) followed by several layers of black electrical tape (to prevent ambient light from entering the plastic material). Optical grease was used to create a layer for the scintillation light transmission between the uncovered end of the scintillator and the PMT (Figure 78).



Figure 78. PMT

Several layers of black electrical tape were used to secure the scintillator on the PMT and create a "light-tight" environment. The PMT anode's current was transmitted to the computer through use of a high voltage (HV) base, attached to the bottom of the detector. The HV base was connected to a digital data acquisition (DAQ) unit (eMorpho by Bridgeport Instruments) which was used to process the detector signals [113]. The detector apparatus is shown Figure 79.



Figure 79. Detector apparatus

There have been numerous studies regarding the use of plastic scintillators in neutron detection investigations. A fluorocarbon based plastic scintillator was proposed as an alternative to the current inorganic fluorine loaded liquid detectors [114]. It was found that the light output of the detector was approximately 30% of that obtained by other plastic counterparts. Additionally, pulse shaped discrimination (PSD) was found to be successful for this proposed scintillator material.

The suitability of creating an inexpensive and efficient thermal neutron detector by adding gadolinium to plastic scintillators was investigated [115]. Known for having the largest radiative

(n, γ) capture cross-sections among stable elements, gadolinium produces low energy conversion electrons and gamma ray after thermal neutron absorption. It was determined that the use of plastic scintillators doped with gadolinium were able to detect up between 46% (0.5% Gd by weight) to 76% of incident thermal neutrons (3% Gd by weight). Additionally, plastic scintillators doped with gadolinium were studied in attempt to provide a neutron counting method using a robust compensation technique [116] instead of PSD. A two-scintillator compensation system was used. The first scintillator (gadolinium loaded detector) was used to detect thermal and fast neutrons as well as photons while the second detector (non-gadolinium loaded) was used to detect only fast neutrons and photons. The results showed unbiased counts over natural radioactivity and fission product background readings (within a monitored area). Thermal neutron detection sensitivities were found to be similar to that of commercially available ^3He detectors.

The first study on the PSD capabilities of the EJ-299-33 plastic scintillator used time-of-flight distributions from a ^{252}Cf source to show that the light output when exposed to neutrons was less than when compared to the EJ-309 liquid scintillator [117]. It was also found that PSD capabilities increased with increasing particle energy. Similarly, a study on the feasibility of the plastic scintillator EJ-299-33 in performing PSD in order to distinguish between incident gamma-rays and neutrons was performed using ^{252}Cf sources [118]. Comparison of PSD results was made to the EJ-309 and EJ-301 liquid scintillators. It was found that the energy and time resolution of the plastic scintillator results were very similar to those of the liquid scintillator, however, the PSD capability at low energies is significantly lower.

Cross-correlation measurements of mixed oxide fuel (MOX) and ^{252}Cf using the plastic scintillator EJ-299-33 were performed in order to compare the plastic scintillators capabilities of

performing PSD to that of the EJ-309 liquid scintillator [119]. It was determined that although the plastic scintillator has lower detection efficiency and PSD capability than its liquid counterpart, it was still capable of distinguishing between the two radioactive sources. It was recommended to use plastic scintillators to characterize correlated samples where particulate information is unnecessary for neutron energies below 1.7 MeV. Additionally, it was found that the EJ-299-33 plastic scintillator was capable of distinguishing between plutonium oxide and plutonium metal by comparison of emitted neutron spectra [120].

The PSD performance of the EJ-299-33 plastic scintillator using a PuBe source was investigated [121]. Different shielding combinations were used to vary the gamma-ray and neutron intensities incident on the detector. It was found that the plastic scintillator was capable of detecting PuBe produced radiations regardless of shielding. Further, a new PSD method known as frequency gradient analysis (FGA) was proposed in order to increase the FOM by reducing the area of overlap of the gamma-ray and neutron events through exploitation of the difference in Fourier transforms of the respective pulses.

The response functions of the EJ-299-33A plastic scintillator for fast neutrons were investigated [122]. Experiments were performed using a 7 MV Van de Graaff system to accelerate proton and deuteron beams into tritium or deuterium targets to generate monoenergetic neutrons (the reaction's angular dependence was also used to fine-tune the neutron energy). Detector responses were measured for neutron energies between 0.12 MeV to 8.2 MeV as well as 12.2 MeV to 20.2 MeV. The on the fly PSD was used to distinguish between photons and neutrons and a figure of merit (FOM) of 1.3 was determined for this detector's neutron response.

6.2 Pulse Shape Discrimination

In a mixed radiation environment, it is important to be able to distinguish between the various radiation types present. Pulse shape discrimination techniques are those employed to discriminate between different types of radiation based on the differences between pulse shapes of their digitized signal waveforms. For this study, the performance of the EJ-299-33A scintillator for PSD in a mixed photon-neutron environment was evaluated. When the scintillator records an individual pulse from a radiation event, particle identification (PID) values were determined according to

$$PID = \frac{IT - PIT}{PIT}$$

where IT is the total integration time, and PIT is the partial integration time of the signal. The PID value can be thought of as the ratio of the energy contained within the "tail" of the pulse (area under the curves after the PIT value until the end of the pulse) to that at the beginning or "head" of the pulse (area under the waveform from the beginning of the pulse to the PIT value) [123].

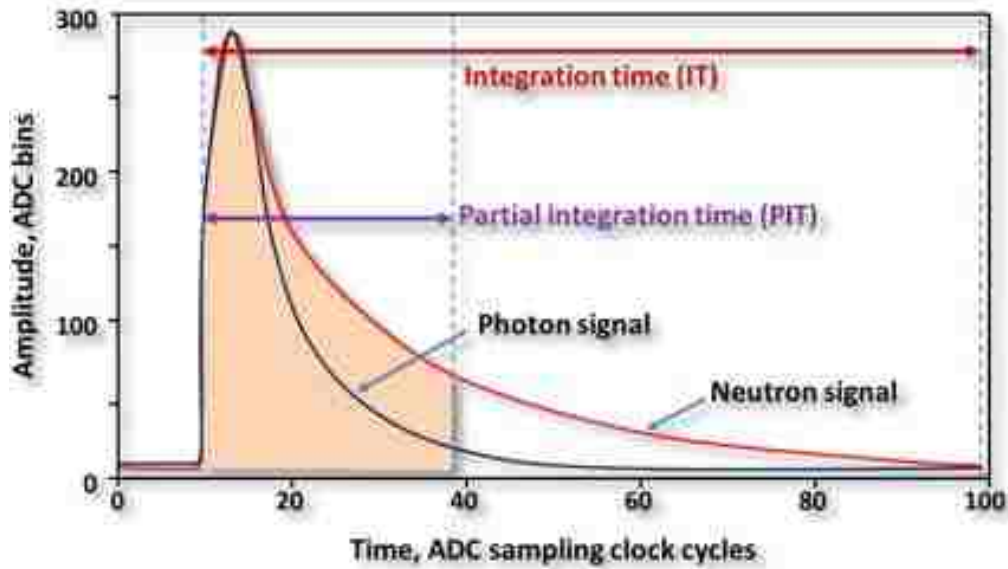


Figure 80. PID components of a digital signal [123]

The "tail" of a neutron signal is longer than that of a photon signal due to a neutron requiring more time to lose its energy. When using PSD to compare digital signals of neutrons and photons, the longer tail results in a larger PID value.

6.3 Neutron multiplicity and coincidence counting

During the fission of SNM, several prompt fast neutrons are emitted in what is known as the neutron multiplicity event. The average number of neutrons emitted per fission, ν , is unique for each isotope (Table 14).

Table 14. Average number of neutrons per fission [124]

Isotope	n_{total}	n_{delayed}	Type
^{232}Th	2.46	0.05	Fast
^{233}U	2.5	0.007	Thermal
^{235}U	2.44	0.016	Thermal
^{238}U	2.82	0.047	Fast
^{238}Pu	3	0.005	Fast
^{239}Pu	2.88	0.007	Thermal
^{240}Pu	3.09	0.009	Fast
^{241}Pu	2.95	0.016	Thermal
^{242}Pu	3.19	0.018	Fast
^{241}Am	3.24	0.004	Thermal
^{242}Cm	2.53	0.001	Spontaneous
^{243}Cm	3.43	0.003	Thermal
^{244}Cm	2.69	0.003	Spontaneous
^{245}Cm	3.6	0.006	Thermal
^{252}Cm	3.77	0.009	Spontaneous

The ability to distinguish between fission neutrons and neutrons produced through other means depends on the ability to measure the neutron multiplicities. By measuring neutron multiples (doublets, triplets, etc.) within a specific coincidence time window, proper identification of the material undergoing fission may be carried out. Multiplicity counting helps to distinguish between neutrons produced through fission and those produced from other reactions.

Studies involving time correlated radiation detection using scintillator detectors have been performed previously. The feasibility of using liquid scintillators for the measurement of both neutron and gamma-ray multiplets emitted by Mixed-Oxide (MOX) samples at Idaho National Lab (INL) was investigated [125]. The results showed that liquid scintillators were capable of performing PSD allowing for the successful distinguishing between neutron and gamma-rays multiplets emitted from the MOX samples. Additional studies using liquid scintillators to count

neutron and gamma-ray multiplets originating from ^{252}Cf and PuBe sources [126] as well as plutonium oxide samples [127] were also performed. In both cases, the liquid scintillators proved capable of performing the desired measurements.

Multiplicity correlations for SNM and non-SNM sources (cosmic radiation present at the sea level) were studied for both neutron and gamma-rays [128]. It was computationally determined that while there was positive correlation between the multiplicity of radiation emitted from an HEU source, there was weak correlation for cosmic radiation. Further, it was difficult to simultaneously observe a burst of neutron and gamma-ray counts from non-SNM sources.

6.4 Computational Model of the Detector

For this study, the suitability of using EJ-299-33A plastic scintillators for the detection of fission neutrons created during the high-energy photon assay of shielded SNM was investigated. To understand how the incident neutron's energy effected the light production within the plastic scintillator, the detector response functions were computationally determined. The response functions were computed using isotropic, monoenergetic (from 0.1 MeV to 13 MeV) neutron point sources located 5 cm from the plastic scintillator. As light in the scintillator is produced by one or more of several possible nuclear reactions occurring within the plastic material, the contribution of each reaction to the total was evaluated. *F6* tallies were used to compute the energy deposited within the plastic material for each of the individual particles (protons, tritons, helions, deuterons, alphas, photons, electrons) that may be produced by interaction of neutrons with the scintillator material. An *F8* tally with a pulse-height light (PHL) special treatment card was used to determine the sum of the responses of all reactions occurring within the plastic. The *PHL* card converts the *F6* results for total energy deposition into a tally of detected pulses within

the detector cell. The effect of varying scintillator thickness on light production was also investigated.

The effect of the scintillator material thickness on the overall detector response was also studied. The tallies to determine the monoenergetic neutron responses are shown in Figure 81.

```

c ----- Tallies -----
c Tallies used to determine detector response from monoenergetic neutrons
f6:h 1001          $ energy deposition from proton
f16:t 1001         $ energy deposition from triton
f26:s 1001         $ energy deposition from helion (3He)
f36:d 1001         $ energy deposition from deuteron
f46:a 1001         $ energy deposition from alpha
f56:p 1001         $ energy deposition from photon
f66:e 1001         $ energy deposition from electron
f8:h,t,s,d,a,p,e 1001 $ detector response from all particles
ft8 ph1 7 6 1 16 1 26 1 36 1 56 1 66 1 76 1 $ PHL treatment (converts deposited energy to light)
e8 0 1000i 15     $ energy bins (0 to 15 MeV, 1000 intervals)
c -----

```

Figure 81. Tallies, detector response to monoenergetic neutrons

The syntax for the PHL treatment line specified that 7 different individual *F6* tallies were to be summed for detector region *I*. Once the detector responses to monoenergetic neutron sources were determined, it was necessary to show that the EJ-299-33A plastic scintillators were capable of performing neutron coincidence measurements.

For neutron coincidence modeling, 5 kg of shielded SNM metal was placed in the center of the area surrounded with four plastic scintillators, arranged at 90 degrees from each other, each positioned 1 cm from the target (Figure 82). A thermal neutron source located in the center of the SNM spheres was used to induce the fission.

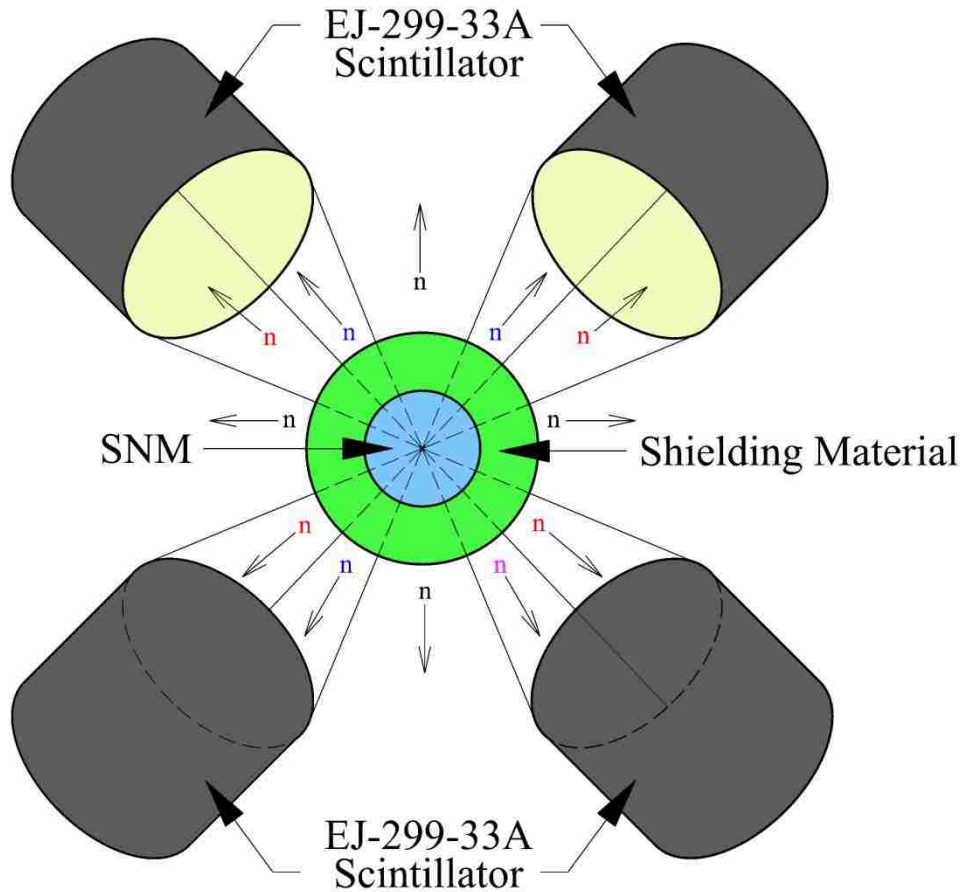


Figure 82. Neutron multiplicity computational model set

Fission neutrons are emitted isotropically from the SNM. The detectors will count fission neutron multiplets (i.e. blue triplets, red quadruplets as shown in Figure 82) and determine detector responses for each. Again, *F6* and *F8* (with *PHL*) tallies were used to determine the detector responses to the neutrons generated by the fission of shielded SNM. For this model, additional information was added to each tally card in order to determine the total energy deposited within all detectors and determine the detector responses for neutron multiplicity events (Figure 83).


```

c ----- Tallies -----
c Tallies used to perform neutron coincidence modeling
c
f6:h 2001 2002 2003 2004          $ energy deposition from protons in all detectors
f16:t 2001 2002 2003 2004        $ energy deposition from tritons in all detectors
f26:s 2001 2002 2003 2004        $ energy deposition from helions in all detectors
f36:d 2001 2002 2003 2004        $ energy deposition from deuterons in all detectors
f46:a 2001 2002 2003 2004        $ energy deposition from alphas in all detectors
c
f8:h,t,s,d,a (2001 2002 2003 2004) $ energy deposition sum, from all particles
ft8 phl 5 6 1 16 1 26 1 36 1 46 1 $ PHL treatment - Region #1 (Detector #1, cell 2001)
          5 6 2 16 2 26 2 36 2 46 2 $ PHL treatment - Region #2 (Detector #2, cell 2002)
          5 6 3 16 3 26 3 36 3 46 3 $ PHL treatment - Region #3 (Detector #3, cell 2003)
          5 6 4 16 4 26 4 36 4 46 4 $ PHL treatment - Region #4 (Detector #4, cell 2004)
c
e8 0 20 nt                        $ 2 Energy bins (yes/no), Region #1
fu8 0 20 nt                        $ 2 Energy bins (yes/no), Region #2
c8 0 20 nt                         $ 2 Energy bins (yes/no), Region #3
fs8 0 20 nt                        $ 2 Energy bins (yes/no), Region #4
t8 0 499i 10 nt                   $ Time bins (every 0.1 shake)
c -----

```

Figure 83. Tallies, neutron coincidence modeling

As four detectors were used in the model, four cell numbers (2001, 2002, 2003, 2004) must accompany each *F6* tally in order to determine the respective particle total energy deposition in all detectors. Similarly, the same four cell numbers must be present in the *F8* tally. Each detector region requires *PHL* definition as well. The MCNPX cards for each are identical (each consisting of the 7 different *F6* tallies required for the *PHL* card) with the exception of the cell specification.

The *e8*, *fu8*, *c8*, and *fs8* cards were used to define the energy bins for each detector region. While neutrons multipliers can be generated at any energy, the specific energies of the neutron multiples were unimportant for this study. The energy bins were set at 0 and 20 in order to allow for a quick interpretation of the output. Defining the energy bins in this method ways allows for quick determination of neutron coincidences as the MCNPX results show that either a coincidence occurred (non-zero energy bin) or it did not (zero energy bin) [129].

6.5 Computational Results

The computational results for the plastic scintillator response functions created by the light generation due to the total energy deposition by protons, tritons, helions, deuterons, photons, electrons, and alpha particles are shown in Figure 84. The statistical uncertainty for the tally values in each energy bin were less than 1% for all results.

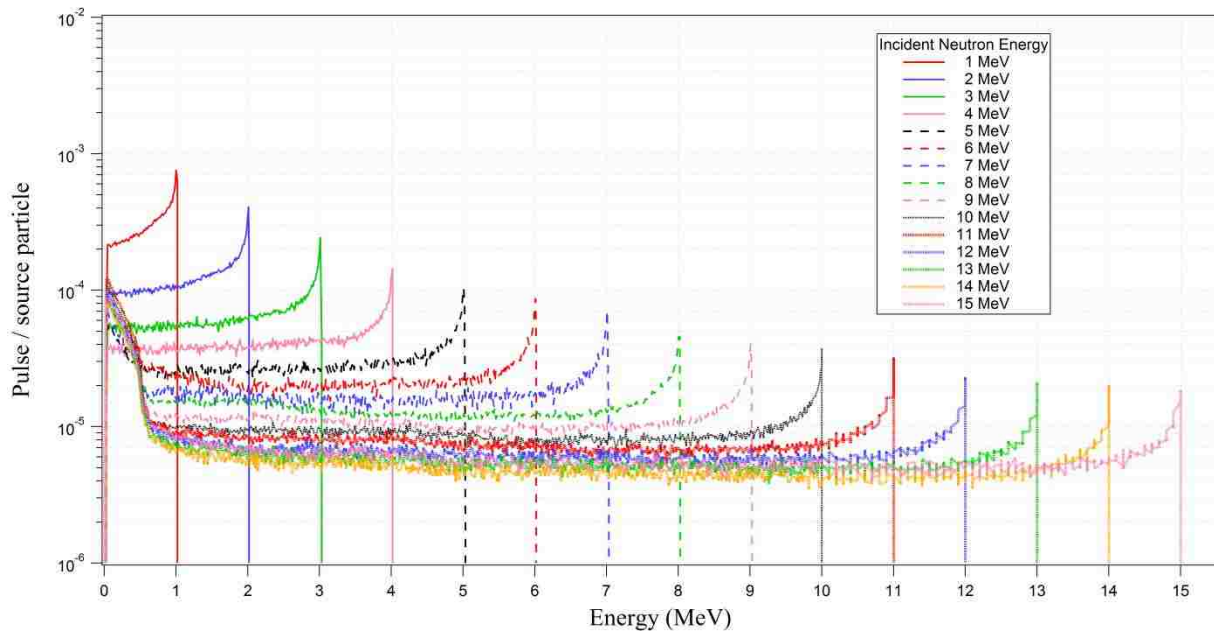


Figure 84. EJ-299-33A response functions for monoenergetic neutron source

The results showed that for fast neutron energies, the EJ-299-33A scintillator produced suitable detector responses. For each incident neutron energy, the total response consisted of an initial PHL spike at low energy (below 1 MeV) followed by an additional spike at the energy corresponding to that of the incident neutron. In order to understand the particle contribution to the detector responses in Figure 84, and identify those responsible for the respective light peaks, the model was run using neutron energies of 2 MeV, 6 MeV, and 15 MeV with the individual pulse height light responses being calculated.

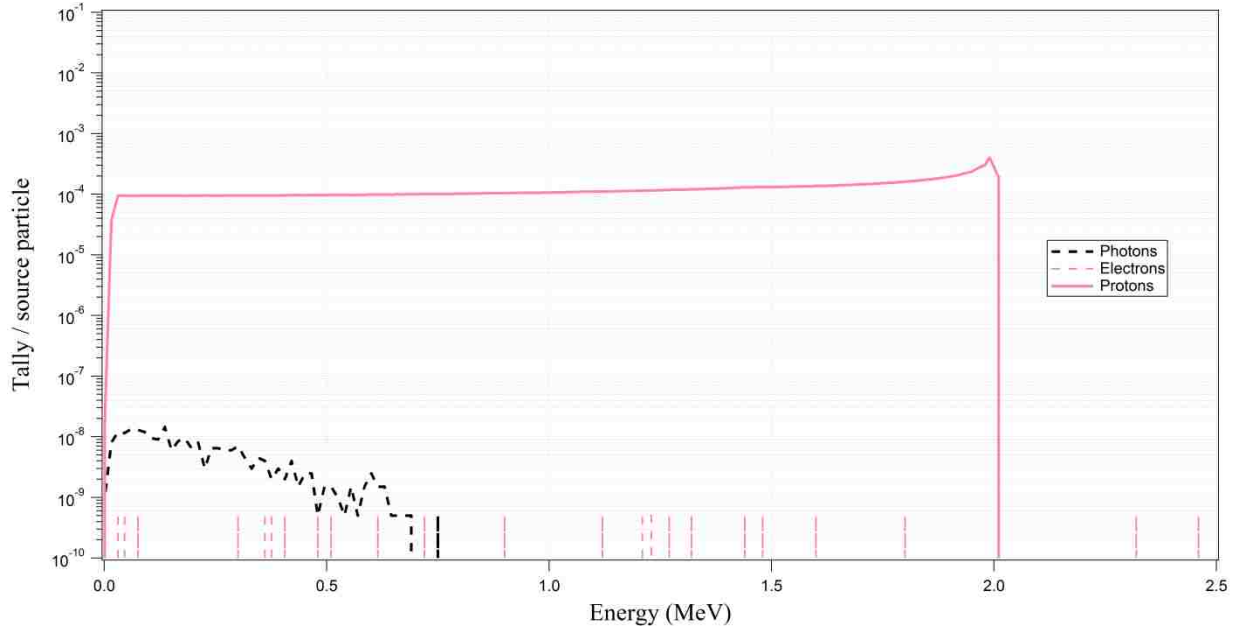


Figure 85. EJ-299-33A response function components for 2 MeV neutron source

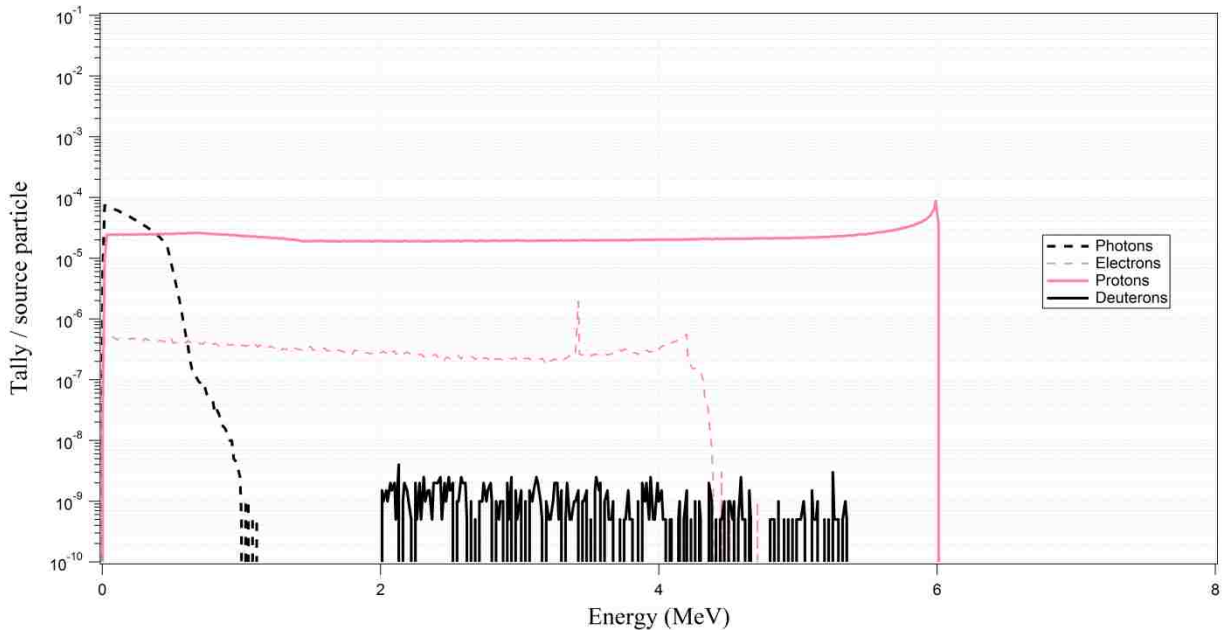


Figure 86. EJ-299-33A response function components for 6 MeV neutron source

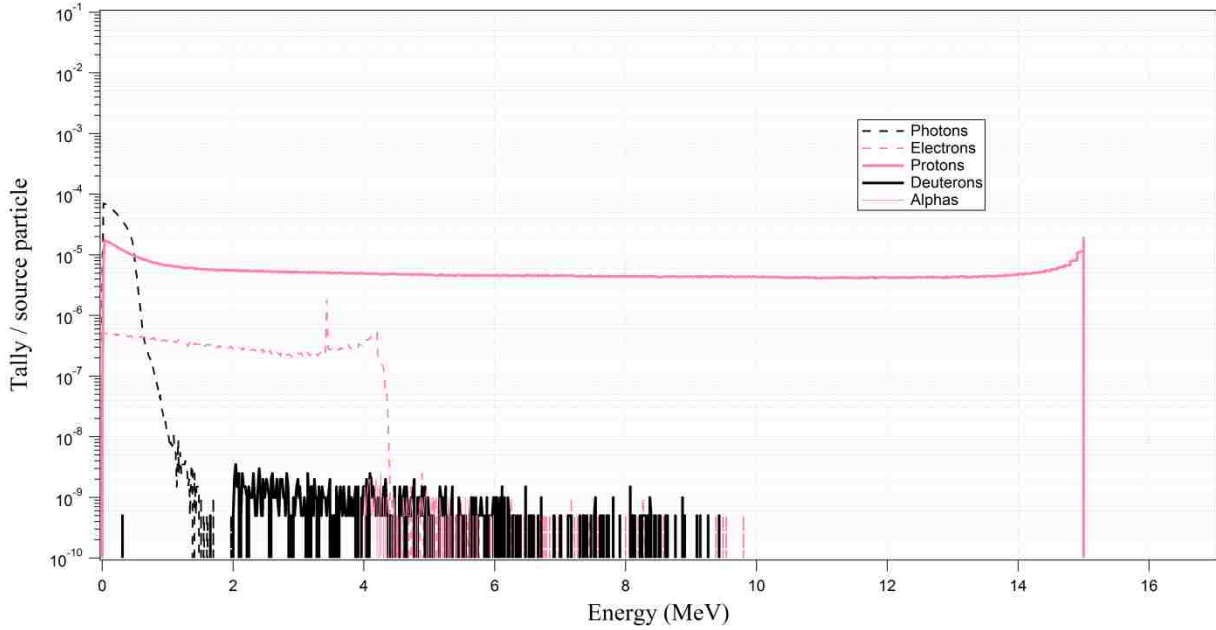


Figure 87. EJ-299-33A response function components for 15 MeV neutron source

The results from Figure 85 through Figure 87 show that the particles contributing most to the response function were protons. The light generation contributions of the remaining particles (alphas, photons, deuterons, electrons) were found to be negligible when compared to the contribution by protons.

It was desired to study the effect of incident neutron energy on the particle energy contributions within the plastic material (Figure 88). The individual energy deposition contributions were determined from the results of the *F6* tallies used in the total detector response models.

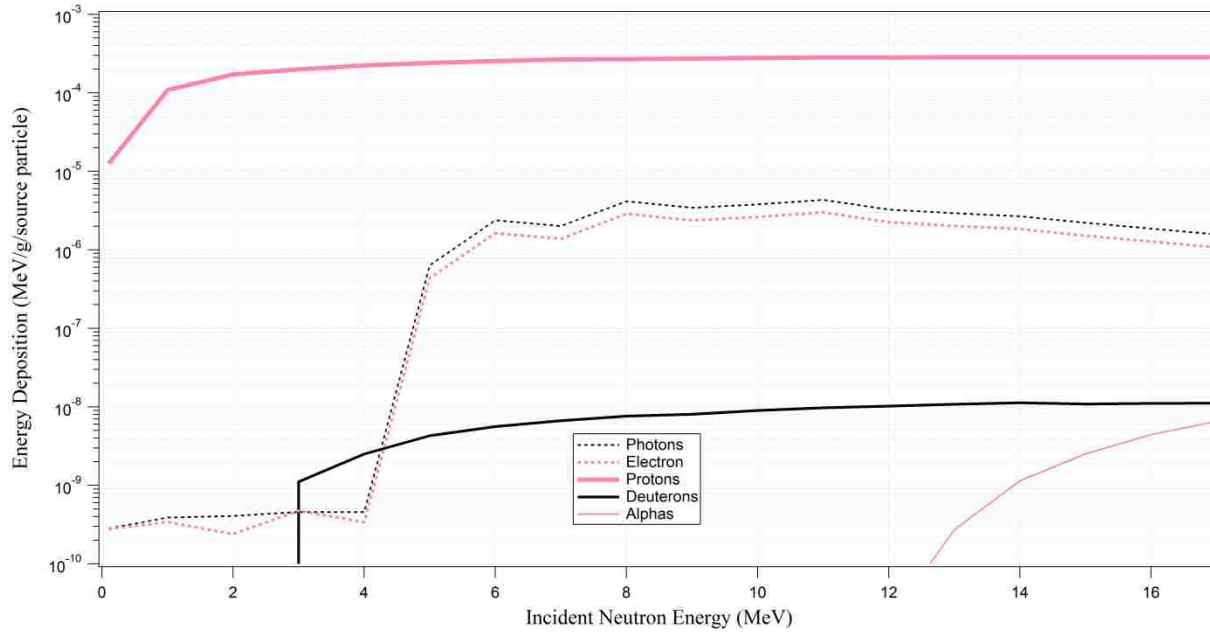


Figure 88. Particle contribution to energy deposition in EJ-299-33A

One can see that for all fast neutron sources, the majority of the energy deposited within the plastic was due to proton recoil. Deuteron production occurred when incident neutron energies exceeded 3 MeV. The total energy deposited by deuterons was found to be less than 0.01% of that deposited by protons. At energies greater than 4 MeV, the energy deposited due to electrons and photons increased by over 4 orders of magnitude, but was still less than 1% of the energy deposited by protons. Alpha particles were produced within the plastic material at neutron energies of 12 MeV and greater, but their energy deposition contribution was 4 orders of magnitude (0.01%) less than that of protons. Lastly, it was determined that no energy was deposited by triton or helion particle interactions.

The MCNPX results for neutron coincidence counting determined the detector responses that were shared between two or more scintillator detectors of the array over the given energy range and the time interval. For this study, the EJ-299-33A scintillator was evaluated for detecting time-correlated neutrons at any possible energy (it was previously shown that neutrons generated

from photofission occur at energies up to 15 MeV). For this reason, the MCNPX model was used to show the total light output due to neutron coincidence at all energies. Examples of the plastic scintillator (for all combinations of detectors within the model) light responses generated due to the detection of neutron singlets and doublets for WG Pu are shown in Figure 89 and Figure 90.

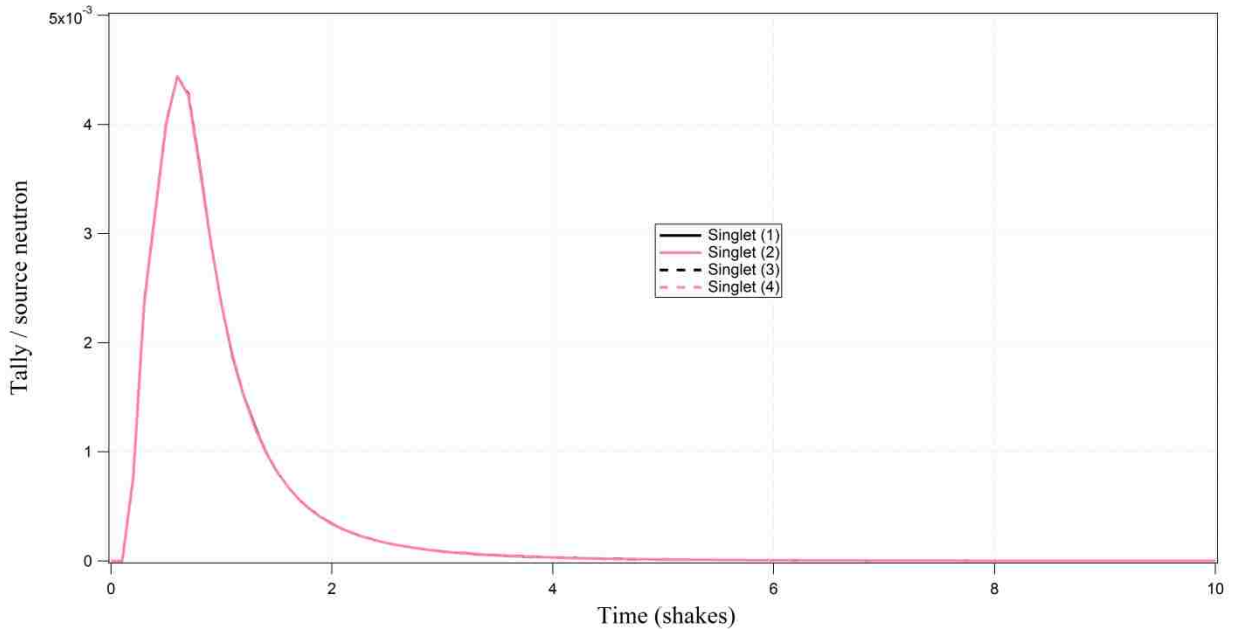


Figure 89. EJ-299-33A singlet responses for WG Pu surrounded by lead shielding

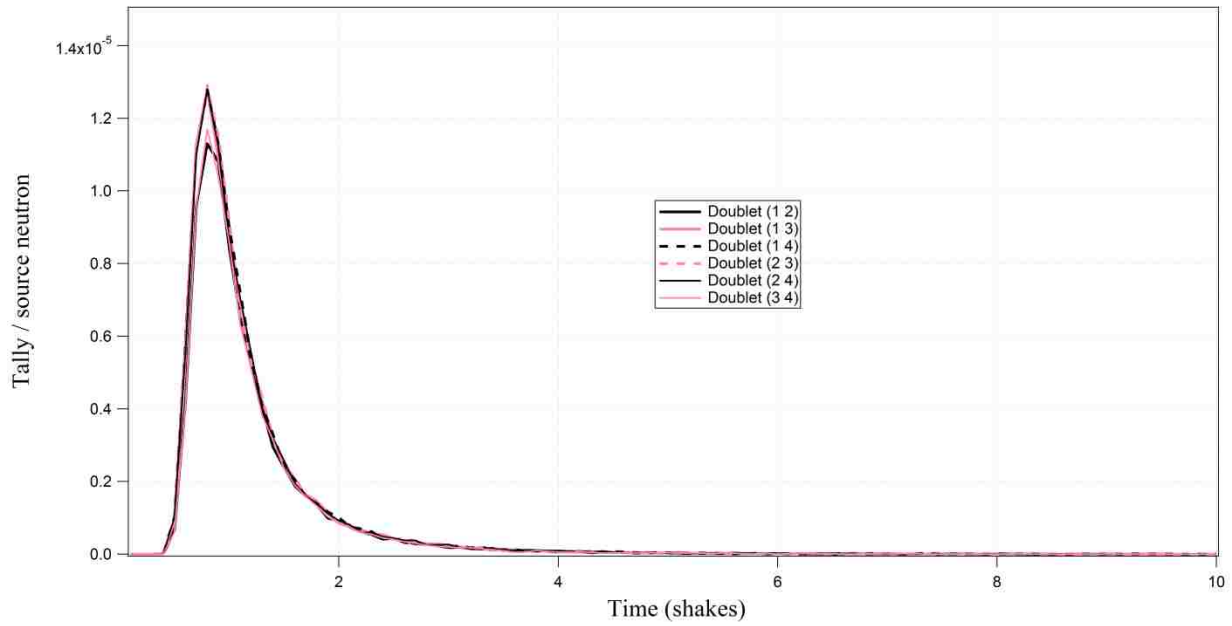


Figure 90. EJ-299-33A doublet responses for WG Pu surrounded by lead shielding

The results showed that for any single detector (for singlets) or combination of two detectors (for doublets), the resulting detector light responses are nearly identical. The same was true for the results in other MCNPX models (i.e. the doublet response for unshielded HEU was similar for each combination of two detectors). The effects of shielding and SNM type on the total light response of the plastic scintillator are shown in Figure 91.

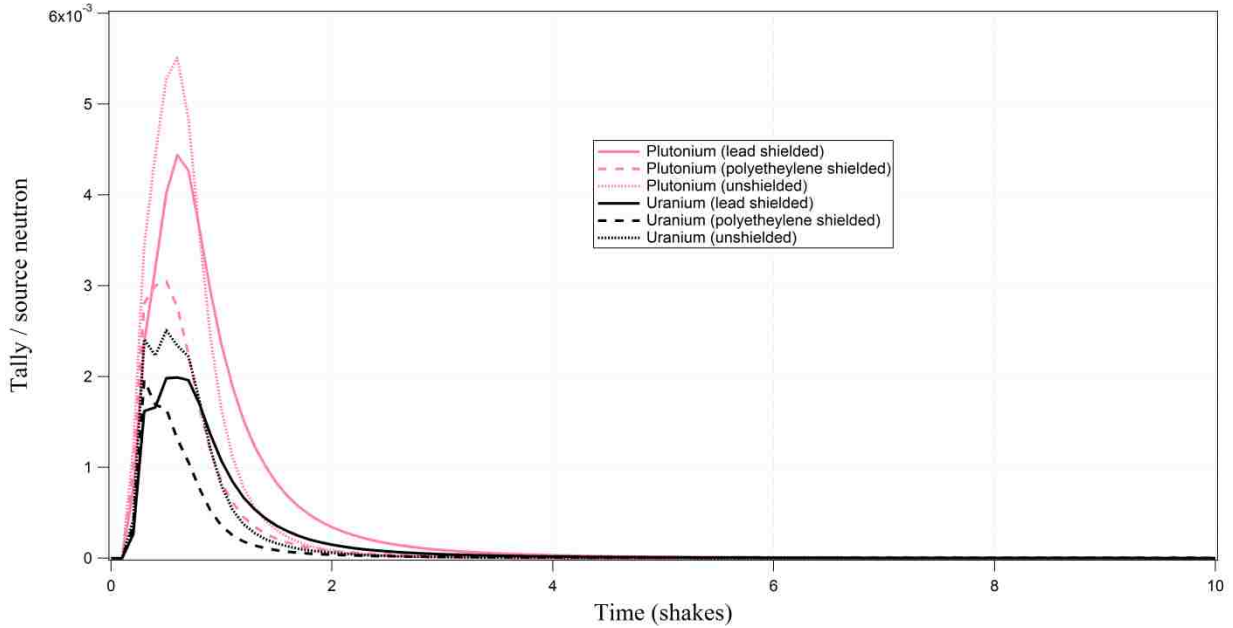


Figure 91. EJ-299-33A singlet responses for SNM fission sources

These results showed that the detector light output for the plutonium models were larger than those of the uranium models. This was in agreement with the results from chapter 5 that determined that neutron fluxes produced during photofission were larger for plutonium metals than uranium metals, despite the fact that the radius of the uranium sphere was approximately 1 cm larger. The results from Figure 91 show that the light generation within the EJ-299-33A scintillator is reduced when using a polyethylene shielding around the SNM. The use of polyethylene shielding minimizes the neutron flux (due to the large hydrogen scattering cross section) outside of the shielding matrix thus lowering the neutrons available to interact with the plastic scintillator. The results for the total light responses generated by the detection of neutron doublets, and triplets are seen in Figure 92 and Figure 93, respectively.

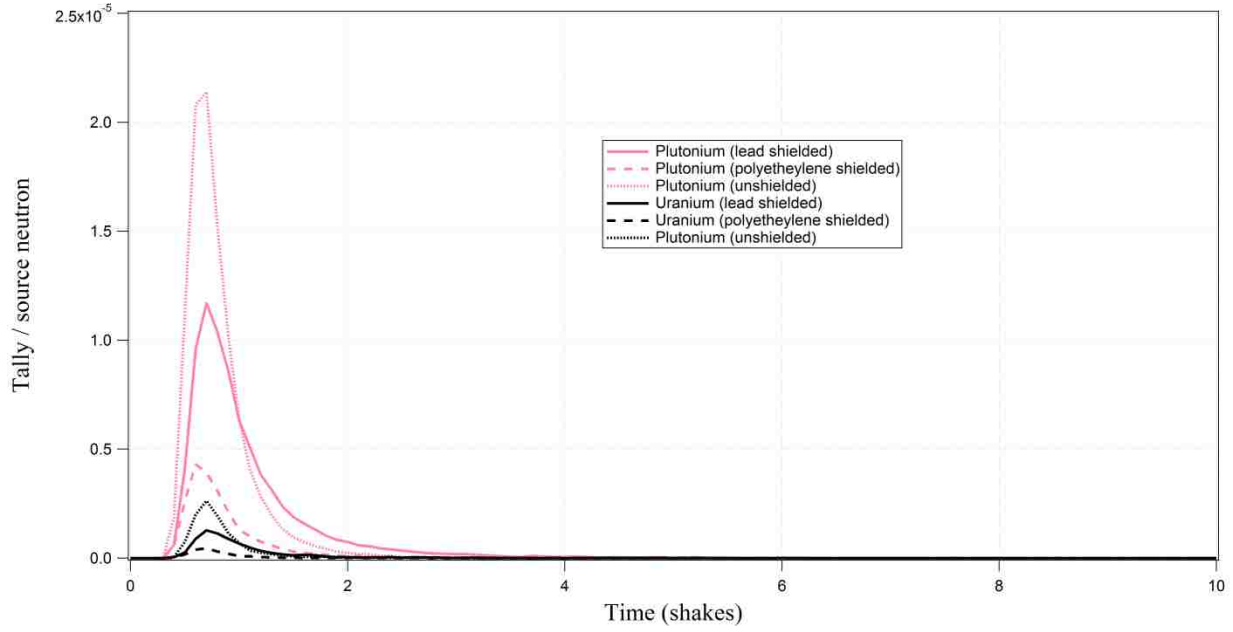


Figure 92. EJ-299-33A doublet responses for SNM fission sources

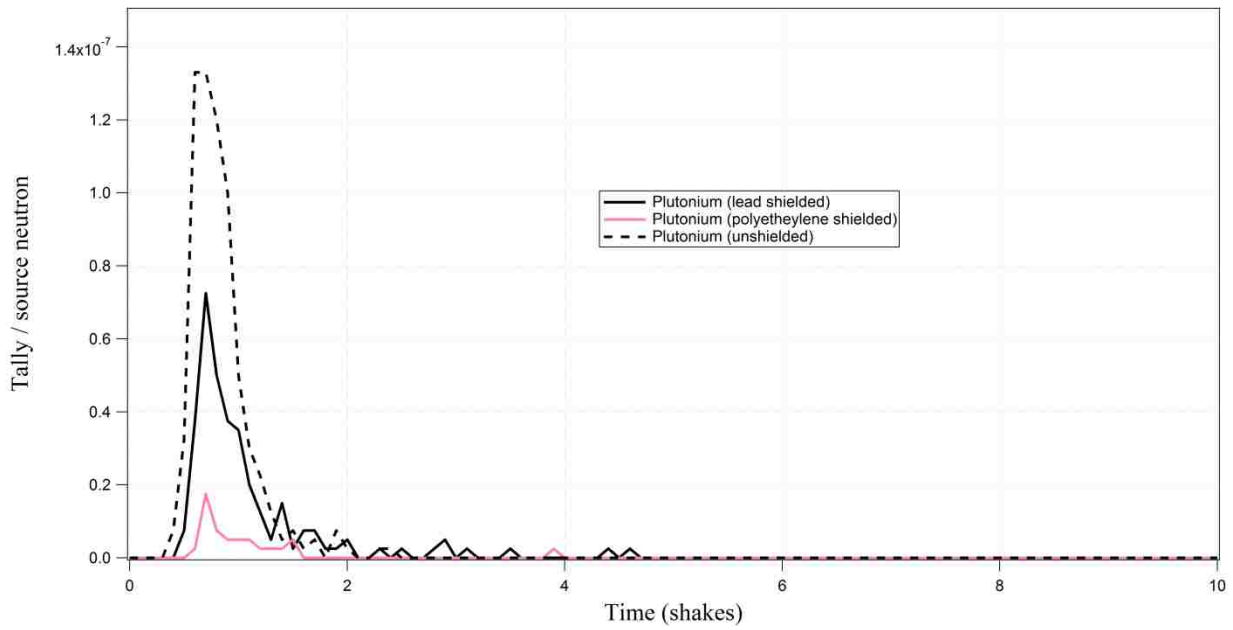


Figure 93. EJ-299-33A triplet response for plutonium fission source

The trends from the neutron coincidence studies show that EJ-299-33A light responses for doublets were larger for a plutonium source than for a uranium source. Additionally, it was determined that there were no triplet responses for the uranium samples in the used four-detector array scheme. No quadruplet responses were determined for either uranium or plutonium materials. Further, it was found that for all multiplets, the use of polyethylene shielding reduced the EJ-299-33A light responses by a larger value than for the plutonium shielding case. Finally, the total light response results from the neutron coincidence studies determined that the triplet response light outputs were two orders of magnitude lower than their respective responses for doublets, which were two orders of magnitude lower than the singlet responses.

The ability of MCNPX to accurately simulate time-correlated neutron events was checked by running the coincidence model using an (α ,n) source substituted for the original thermal neutron induced fission SNM sources. The computed coincidence (due to neutron doublets, triplets, and quadruplets) light responses in the plastic material for the MCNPX model are shown in Figure 94.

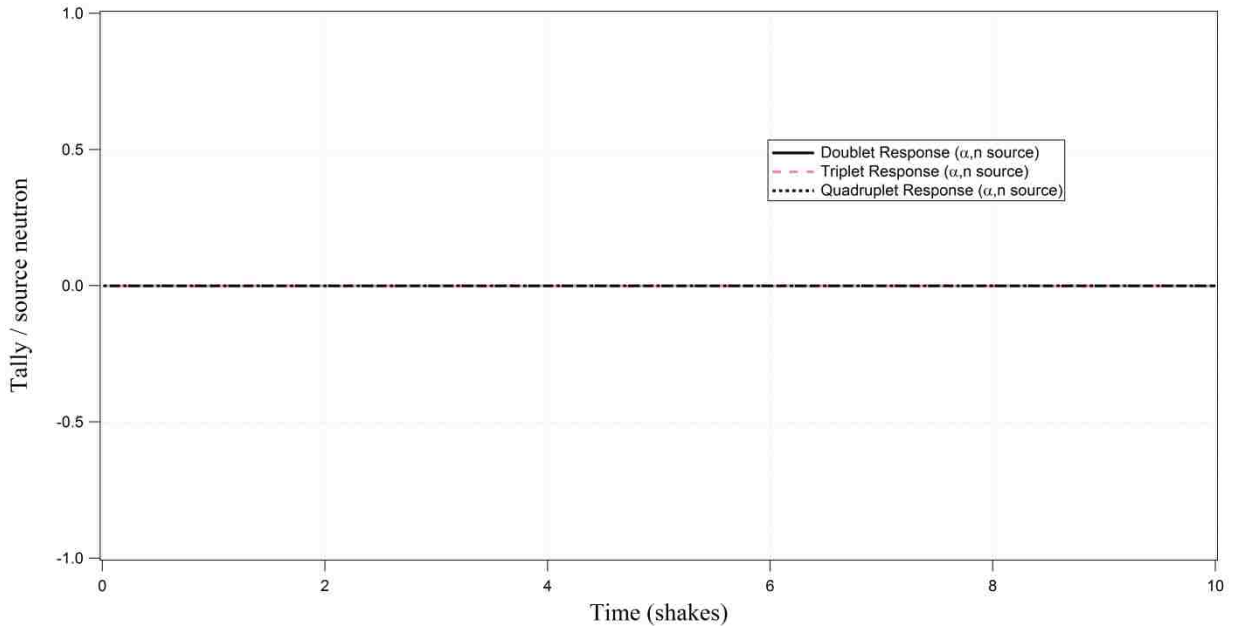


Figure 94. EJ-299-33A multiplet responses for (α,n) source

The results showed that the light production in the plastic scintillator for neutron multiplets from an (α,n) source was zero. This was expected as neutron multiplets are not generated by an (α,n) source, but only single neutrons at different moments in time. The MCNPX model produced neutron multiplet tally results in the array of four EJ-299-33A detectors for a fission source, but did not produce any neutron multiplet tally results for an (α,n) source, confirming that these scintillators enable the detection of coincident neutrons generated in the fission events.

6.5 Experimental Set-up

The EJ-299-33A scintillator was used to perform PSD to distinguish between photons and neutrons. The scintillator was experimentally tested using a 32g, 2 curie (Ci) plutonium-beryllium ($^{239}\text{PuBe}$) source. The sealed PuBe source was housed within a 55-gallon drum that filled with a paraffin wax to minimize the dose rates in the vault (Figure 95).



Figure 95. UNLV 2 Ci PuBe source

The scintillator was placed directly against the drum, at the height of the beam.

6.6 Experimental Results

A Bridgeport Instruments (BPI) graphical user interface (GUI) was used to control the eMorpho DAQ. The digital pulses of individual particle events were analyzed to determine their time properties by using the *trace* function (shown in Figure 96).

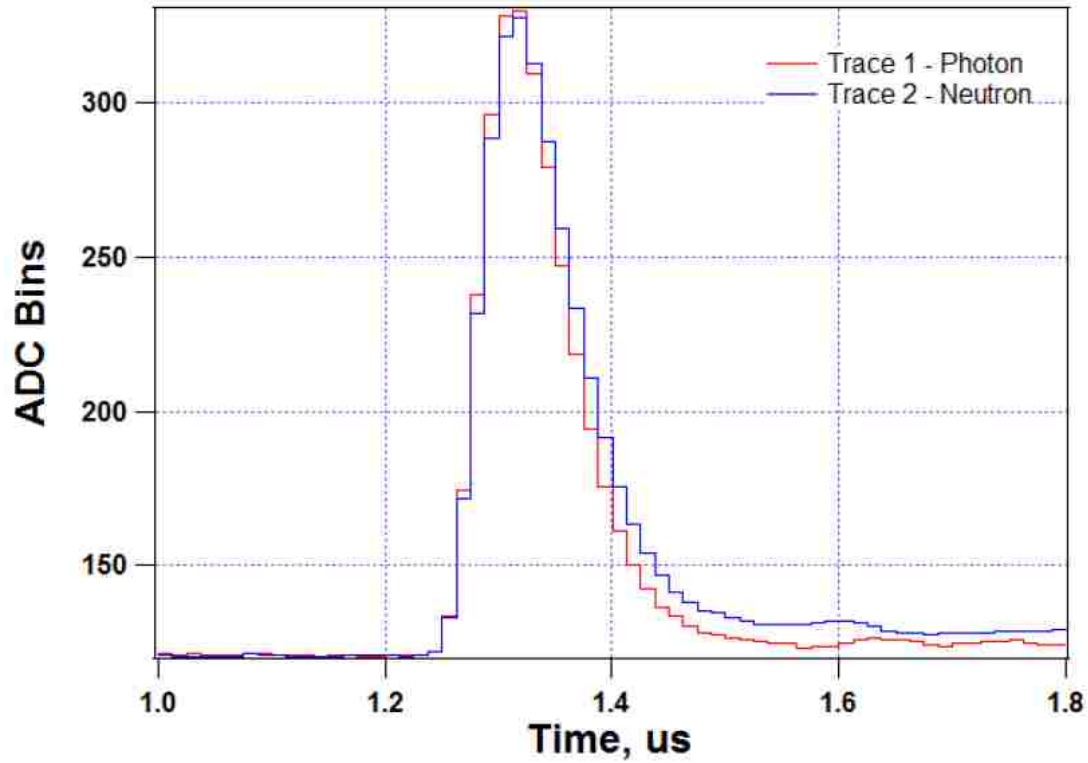


Figure 96. Digital pulses from PuBe source [109]

The pulse shape was similar for both photon and neutrons, but the neutron “tail” is slightly longer (take more time for the neutron to lose its energy) than the photon “tail.” PID values were determined for 85,000 particle counts (250 buffers, each buffer consisting of 340 events) with the results shown in Figure 97.

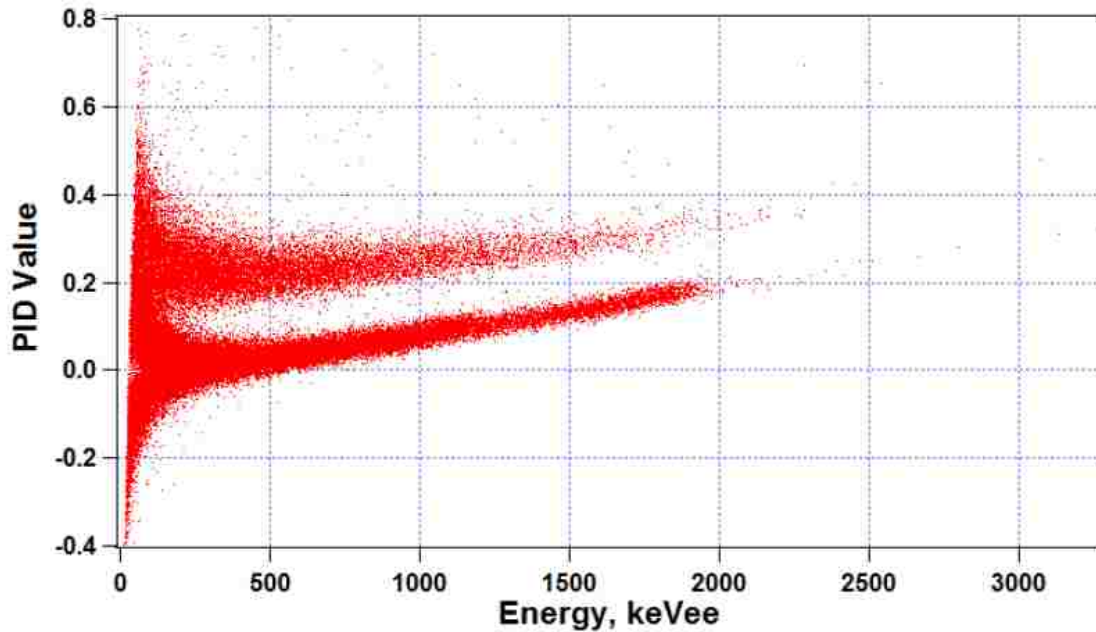


Figure 97. PID values, PuBe source [109]

The PSD results showed two distinct PID-value groupings. The lower grouping was due to photons while the upper grouping was due to neutrons. In order to distinguish between the two particles, it is necessary to establish a PID cut-off value. To determine this PID cut-off value, the counts versus PID value were plotted (Figure 98).

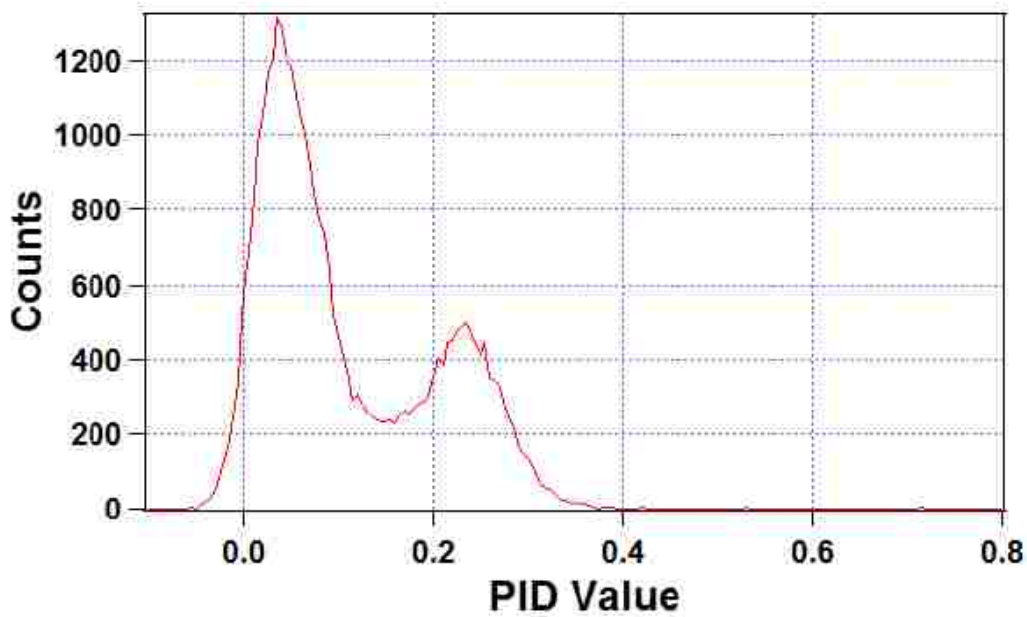


Figure 98. Number of PID counts, PuBe source [109]

The first peak (PID ~ 0.06) corresponds to photon values while the second (PID ~ 0.24) corresponds to neutron values. Based on these results, the PID cut-off value should be chosen between the two, near 0.17.

The experiment was repeated with a ^{60}Co source (gamma-ray emitter only) to confirm these results and show that both neutrons and photons are able to be separated using the PID method. The results of the ^{60}Co measurements were as expected, with only a lone grouping of PID values (Figure 99) and a lone PID peak (Figure 100) being found. Only photons were produced during the decay of ^{60}Co therefore only one grouping was found. The results from the ^{60}Co measurements confirm the accuracy of the PSD measurements of the PuBe source's radiation emissions.

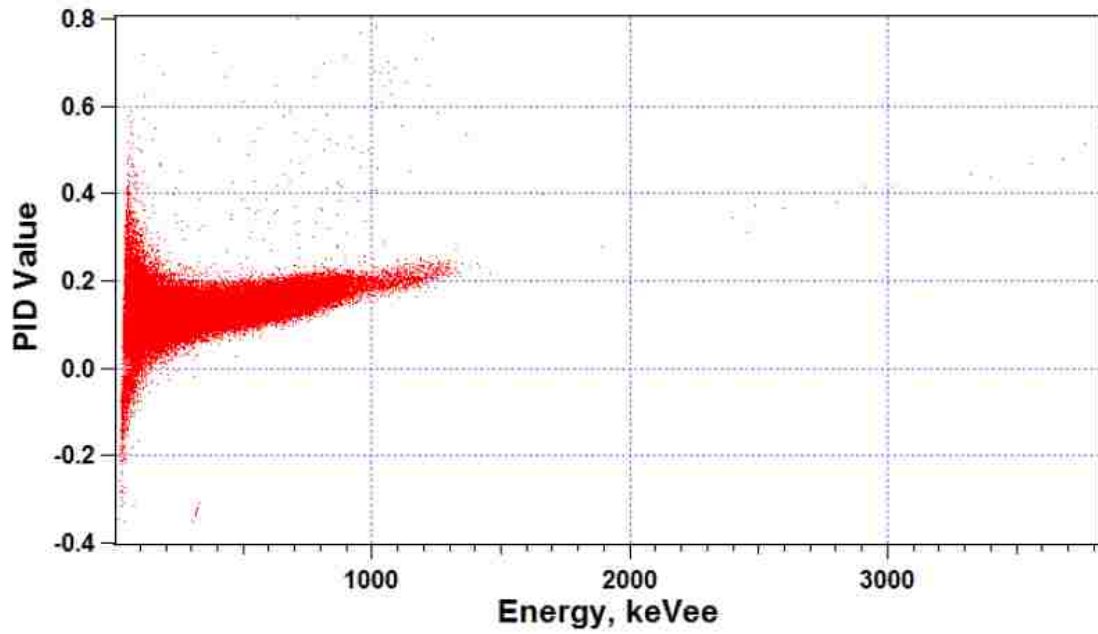


Figure 99. PID values, Co-60 source [109]

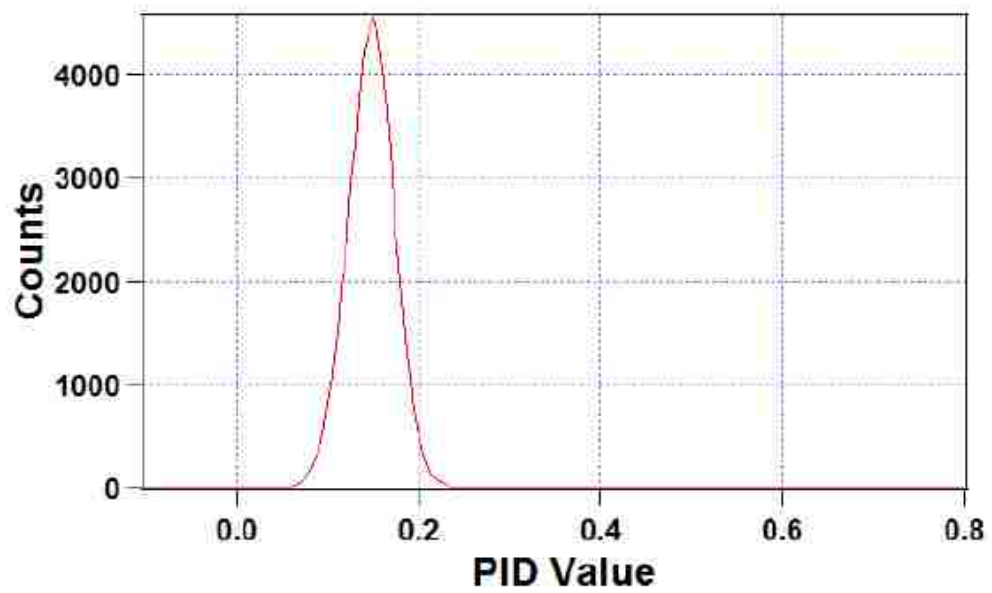


Figure 100. Number of PID counts, Co-60 source [109]

In order to simulate time-correlated analysis of a neutron multiplicity event, a ^{60}Co source was used as the SNM was not available to test. When ^{60}Co decays, two photons (1.17 MeV and 1.33 MeV) are emitted within 10^{-12} seconds of each other (Figure 101).

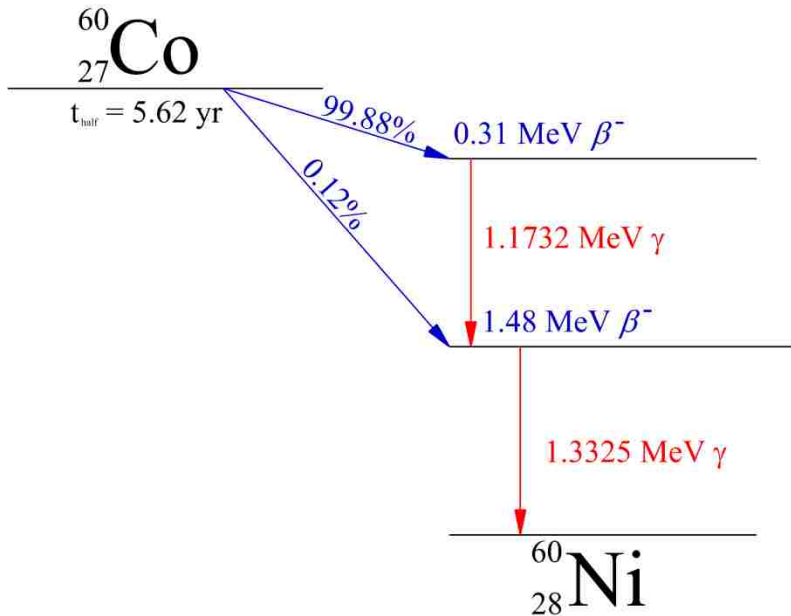


Figure 101. Cobalt-60 Decay Scheme

The first photon (1.17 MeV) can be emitted at any angle, with the second photon being emitted at an angle that satisfies momentum conservation. In order to ensure that both photons can be seen by the two EJ-299-33A scintillators at the same time, the ^{60}Co was placed directly between them (Figure 102). The BPI qMorpho DAQ was used to perform coincident photons detection. qMorpho allows for multiple scintillator detectors to be used in parallel and functions the same way as eMorpho [113].



Figure 102. Coincident photon experimental setup [109]

Photon pulses were detected in both detectors (Figure 103). The individual pulse heights were occurred different values, but at approximately the same moment in time (1 ADC clock cycle is equal to 12.5 ns).

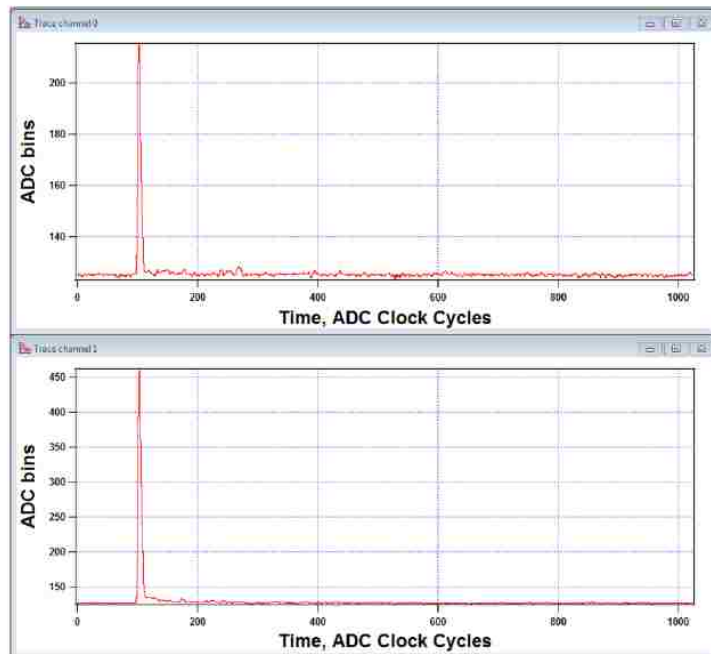


Figure 103. Coincident photon pulses, Co-60 source, separated [109]

When the two pulses are compared directly (Figure 104) it was determined that both events occurred just after 1.2 μs on the used time scale. The results show that the EJ-299-33A scintillators equipped with the digital DAQ are capable of performing coincident measurements.

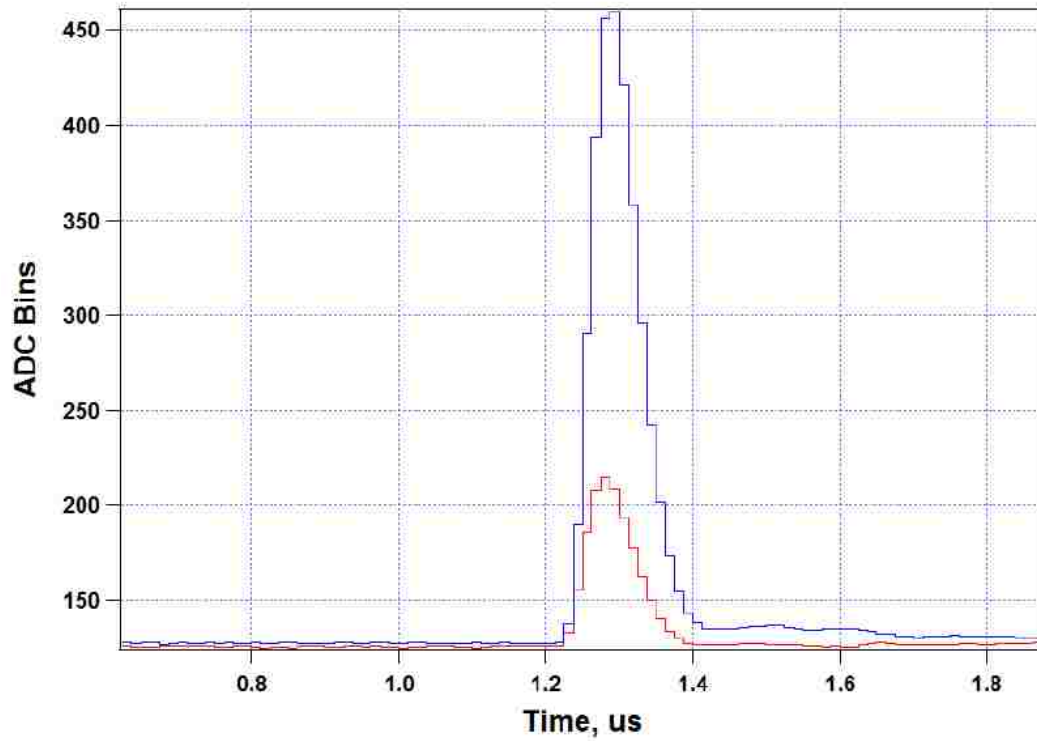


Figure 104. Coincident photon pluses, Co-60 source, combined [109]

Chapter 7: Conclusions

The purpose of this study was to computationally and experimentally evaluate that a Varian K15 linac could be used for the photofission assay of shielded SNM, and that the resulting fast neutrons emitted in fission events could be detected by the EJ-299-33A plastic scintillator detectors.

Linac-based photon source terms were computationally determined for 6 MeV and 15 MeV linacs using MCNP5 and MCNPX. Photon dose rates were measured to validate the computational models. It was found that the models allow conservative estimates of dose rates for the 6 MeV and 15 MeV linacs by factors of 1.13 and 1.35, respectively. The models were then used to determine the dose rate footprints within the UNLV accelerator facility and validate that the dose rate outside the facility was kept below the NRC guideline (2 mrem/hr). The M6 linac model was used to simulate the irradiation of a beryllium converter and determine the flux of photoneutrons produced. Gold foil activation was used to measure the neutron yield above the converter. The MCNPX model was found to give estimates 1.43 times that of the measured value. It was determined that the model was suitable in determining conservative estimates for photoneutron fluxes produced by the linac.

The K15 linac model was used to determine the radiation signatures following the high-energy photon assay of shielded uranium and plutonium. Four scenarios were studied for each material – photon assay of unshielded SNM, SNM with 5 cm of polyethylene shielding, SNM with 5 cm of lead shielding, and SNM with combination shielding (2.5 cm of polyethylene surrounded by 2.5 of lead). The results showed that despite the presence of the considered shielding types, fast neutron fluxes (fission and photoneutron) up to 10^8 neutrons/cm²/s were

expected. It was also found that as the SNM enrichment increased, the ratio of fission neutron flux to total neutron (fission plus photoneutron) flux increased.

The modeling results showed that the EJ-299-33A plastic scintillator produces suitable detector responses for fast neutrons generated during the photofission assay of shielded SNM. It was also computationally shown that an array of the plastic scintillator detectors was capable of performing time-correlated measurements of neutron multiplets generated during fission events. Furthermore, it was shown experimentally that the EJ-299-33A scintillator detectors were capable of performing PSD in a mixed photon-neutron environment (using a PuBe source) as well as performing time correlated analysis using a photon source (^{60}Co).

Experimental work was performed to validate the computational linac source term models as well as to evaluate the suitability of using EJ-299-33A scintillators for the detection of fast fission neutrons. However, a lack of SNM (for a variety of reasons) prevented experimental photon assay studies. In the future, experimental work using the K15 linac for the photofission assay of shielded SNM is suggested.

References

- [1] Maritime Transport Committee, "Security in maritime transport: Risk factors and economic impact." OECD Direct. Sci. Tech. Ind., Paris, France, 2003.
- [2] Inbound Logistics. (2015). "Top 10 U.S. Container Ports," [Online] Available: <http://www.inboundlogistics.com/cms/article/top-10-us-container-ports/> [Accessed 28 June 2016]
- [3] Homeland Security News Wire. (2017). "Cargo and Containers," [Online]. Available: <http://www.homelandsecuritynewswire.com/topics/cargo-container-security?page=2>. [Accessed 15 March 2017]
- [4] IAEA. (2016). "Concept and terms," [Online]. Available: <http://www-ns.iaea.org/standards/concepts-terms.asp>. [Accessed 28 April 2016]
- [5] "Nuclear Security and Safeguards," U.S. NRC, 2015 [Online]. Available: <http://www.nrc.gov/security.html>. [Accessed 25 June 2016].
- [6] U.S. NRC. (2015). "Safeguard Categories of SNM," [Online]. Available: <http://www.nrc.gov/security/domestic/mca/snm.html>. [Accessed 10 July 2016].
- [7] Knoll, G., *Radiation Detection and Measurement*. 4th ed. Hoboken, NJ: John Wiley & Sons, Inc., 2010.
- [8] Yang, H., "Active Interrogation Methods for Detection of Special Nuclear Material," PhD Dissertation, Department of Nuclear Engineering and Radiation Sciences, University of Michigan, Ann Arbor, MI, 2009.
- [9] Almeida, S., *et al.*, "Neutron activation analysis for identification of African mineral dust transport," *Journal of Radioanalytical and Nuclear Chemistry*, vol. 276 (1), pp. 161-165, 2008.
- [10] Nomura, K., *et al.*, "The determination of scandium and gold in meteorites, tektites and standard rocks by neutron activation analysis with an internal-reference method," *Analytica Chimica Acta*, vol. 51 (3), pp. 417-424, 1970.
- [11] Rahn, K., and Sturdivan, L., "Neutron activation and the JFK assassination, Part I. Data and interpretation," *Journal of Radioanalytical and Nuclear Chemistry* vol. 262 (1), pp. 205-213, 2004.
- [12] Rahn, K., and Sturdivan, L., "Neutron activation and the JFK assassination, Part II. Extended benefits," *Journal of Radioanalytical and Nuclear Chemistry* vol. 262 (1), pp. 215-222, 2004.

- [13] Esposito, A., *et al.*, "Determination of the neutron spectra around an 18MV medical LINAC with a passive Bonner sphere spectrometer based on gold foils and TLD pairs," *Radiation Measurements*, vol. 43 (2-6), pp. 1038-1043, 2008.
- [14] Yücel, H., *et al.*, "Measurement of Photo-Neutron Dose from an 18-MV Medical Linac Using a Foil Activation Method in View of Radiation Protection of Patients." *Nuclear Engineering and Technology*, vol. 48 (2), pp. 525-532,
- [15] Hill, T., "Neutron fluence measurements of the Siemens Oncor linear accelerator utilizing gold foil activation," M.S. thesis, Medical University of Ohio, University of Toledo, Toledo, OH, 2005
- [16] Mohammadi, N., *et al.*, "Neutron spectrometry and determination of neutron contamination around the 15 MV Siemens Primus LINAC." *Journal of Radioanalytical and Nuclear Chemistry*, vol. 304 (3), pp. 1001-1008. 2015.
- [17] Loughlin, M., *et al.*, "Neutron activation studies on JET." *Fusion Engineering and Design* vol. 58, pp. 967-971, 2001.
- [18] Klix, A., *et al.*, "Neutronics diagnostics for European ITER TBMS: Activation foil spectrometry for short measurement cycles." *Fusion Engineering and Design*, vol. 87 (7-8), pp. 1301-1306, 2012.
- [19] Klix, A., *et al.*, "Test facility for a neutron flux spectrometer system based on the foil activation technique for neutronics experiments with the ITER TBM." *Fusion Engineering and Design*, vol. 86 (9), pp. 2322-2325, 2011.
- [20] Chao, J., Chiang, A., "Activation detection using indium foils for simultaneous monitoring neutron and photon intensities in a reactor core." *Radiation Measurements*, vol. 45 (9), pp. 1024-1033, 2010.
- [21] Carrel, F., *et al.*, "Detection of high-energy delayed gammas for nuclear waste packages characterization," *Nuclear Instruments and Methods in Physics Research A*, vol. 652 (1), pp. 137-139, 2011.
- [22] Kouzes, R., *et al.*, "Passive neutron detection for interdiction of nuclear material at borders," *Nuclear Instruments and Methods in Physics Research A*, vol. 584 (2), pp. 383-400, 2008.
- [23] Murer, D., *et al.*, "Benefits of time correlation measurements for passive screening," *International Journal of Modern Physics: Conference Series*, vol. 272, 2014.
- [24] Vaughn, S., "Investigation of a Passive, Temporal, Neutron Monitoring System that Functions within the Confines of START I," M.S. Thesis, Dept. Engineering and Physics, Air Force Institute of Technology, Wright-Patterson AFB, OH, 2003.

- [25] Skutnik, S., and Davis, D., "Characterization of the non-uniqueness of used nuclear fuel burnup signatures through a mesh-adaptive direct search," *Nuclear Instruments and Methods in Physics Research A*, vol. 817, pp. 7-18, 2016.
- [26] Whetstone, Z., and Kearfott, K., "A review of conventional explosives detection using active neutron interrogation," *Journal of Radioanalytical Nuclear Chemistry*, vol. 301 (3), pp. 629-639. 2014.
- [27] Brandis, M., *et al.*, "Nuclear-reaction-based radiation source for explosives-and SNM-detection in massive cargo," *AIP Conf. Proc.*, vol. 1336, pp. 711-716, 2011.
- [28] McConchie, S., "Detection of hazardous materials in vehicles using neutron interrogation techniques," Ph.D. dissertation, Department of Physics and Astronomy, Purdue Univ., W. Lafayette, IN, 2007.
- [29] Hall, J., *et al.*, "The Nuclear Car Wash: Neutron interrogation of cargo containers to detect hidden SNM," *Nuclear Instruments and Methods in Physics Research B*, vol. 261 (1), pp. 337-340, 2007.
- [30] Slaughter, D., *et al.*, "The "nuclear car wash": a scanner to detect illicit special nuclear material in cargo containers," *IEEE Sensors Journal*, vol. 5 (4), pp. 560-564, 2005.
- [31] Slaughter, D., *et al.*, "The nuclear car wash: A system to detect nuclear weapons in commercial cargo shipments," *Nuclear Instruments and Methods in Physics Research A*, vol. 579, pp. 349-352, 2007.
- [32] Kane, S., *et al.*, "Simulations of Multi-Gamma Coincidences From Neutron-Induced Fission in Special Nuclear Materials," *IEEE Transactions on Nuclear Science*, vol. 60 (2), pp. 533-538, 2013.
- [33] Kane, S., "Detection of special nuclear materials using prompt gamma-rays from fast and slow neutron-induced fission," Ph.D. dissertation, Department of Physics and Astronomy, Purdue Univ., W. Lafayette, IN, 2010.
- [34] Kane, S. and Koltick, D., "A Neutron Based Interrogation System For SNM In Cargo." *AIP Conf. Proc.*, vol. 1336, pp. 717-722, 2011.
- [35] Kane, S. and Koltick, D., "A Cargo Inspection System for Special Nuclear Material (SNM) Based on Associated Particle Neutron Generators and Liquid-Kr Detectors," *AIP Conf. Proc.*, vol. 1336, pp. 685-688, 2009.
- [36] San Francisco Chronicle, "Smarter technology for port defense/Livermore lab's neutron beam would expose atomic bombs in ship cargo," [Online] Available: <http://www.sfgate.com/news/article/Smarter-technology-for-port-defense-Livermore-2713686.php#page-2> [Accessed 15 May 2016].

- [37] Taggart, D., *et al.*, "LANL's Mobile Nondestructive Assay and Examination Systems for Radioactive Wastes," American Nuclear Society/Spectrum, Seattle, WA 1996
- [38] A.E. Evans, "The Expanding Role of the Small Van de Graaff in Nuclear Nondestructive Analysis," IEEE, Los Alamos Scientific Laboratory, 1973
- [39] P. Rinard, "Shufflers," LANL Passive Nondestructive Assay Manual - PANDA, Los Alamos National Laboratory, 2006. [Online]. Available: <http://www.lanl.gov/orgs/n/n1/panda/9.%20Shufflers%20LAUR.pdf> [Accessed 05 June 2016]
- [40] J.E Doyle. *Nuclear Safeguards, Security, and Nonproliferation*, Burlington, MA: Butterworth-Heinemann, pp 50-532008
- [41] LANL Newsroom. (2013), "Using Laser-driven Neutrons to Stop Nuclear Smugglers." 04 [Online] Available: https://www.eurekalert.org/pub_releases/2013-06/danl-uln060413.php [Accessed] 29 March 2015.
- [42] Martz, H., "Gamma-Ray Scanner Systems for Nondestructive Assay of Heterogeneous Waste Barrels." LLNL. UCRL-JC126865. International Symposium on International Safeguards, Vienna, Austria, 1997.
- [43] Foster, A., and Wright, R., *Basic Nuclear Engineering*, 4th ed. Boston, MA: Allyn and Bacon, 1983.
- [44] Lamarsh, J., and Baratta, A., *Introduction to Nuclear Engineering*, 3rd ed. Upper Saddle River, NJ: Prentice Hall, 2001.
- [45] Sapling Learning, "Electromagnetic Spectrum," 1999. [Online]. Available: <https://sites.google.com/site/chempendix/em-spectrum>. [Accessed 28 April 2017].
- [46] Hall, E., and Giaccia, A., *Radiobiology for the Radiobiologist*, 7th ed. Philadelphia, PA: Lippincott Williams & Wilkins, 2012
- [47] Relative importance of the three principal interactions of photons in matter. Digital Image. Encyclopaedia of Occupational Health and Safety. [Online]. Available: <http://www.iloencyclopaedia.org/part-vi-16255/radiation-ionizing> [Accessed 17 Jan 2016].
- [48] National Nuclear Data Center. Q-value Calculator. [Online]. Available: <http://www.nndc.bnl.gov/qcalc/>. [Accessed 5 Dec 2015].
- [49] National Nuclear Data Center. Evaluated Nuclear Data File (ENDF) Retrieval & Plotting. [Online]. Available: <http://www.nndc.bnl.gov/sigma/> [Accessed 13 March 2016].
- [50] Lowe, D., "Novel Production Techniques of Radioisotopes Using Electron Accelerators," Ph.D. dissertation, Department of Mechanical Engineering, University of Nevada, Las Vegas, Nevada, Las Vegas, 2012.

- [51] Broemme, J., *et al.*, "Adjuvant therapy after resection of brain metastases: Frameless image-guided LINAC-based radiosurgery and stereotactic hypofractionated radiotherapy," *Strahlentherapie Und Onkologie*, vol. 189, no. 9, pp. 765-770, 2013.
- [52] Fong, B., *et al.*, "Hearing preservation after LINAC radiosurgery and LINAC radiotherapy for vestibular schwannoma." *Journal of Clinical Neuroscience.*, vol. 19, pp. 1065-1070, 2012.
- [53] Dracos, M., "The ESSvSB Project for Leptonic CP Violation Discovery based on the European Spallation Source Linac," *Nuclear Particle Physics Proceedings*, vol. 273-275, pp. 1726-1731, 2016.
- [54] Brice, S., "Proton Improvement Plan II: An 800 MeV Superconducting Linac to Support Megawatt Proton Beams at Fermilab." *Nuclear Particle Physics Proceedings*, vol. 273-275, pp. 238-243, 2016.
- [55] Hori M., and Hanke, K., "Spatial and temporal beam profile monitor with nanosecond resolution for CERN's Linac4 and Superconducting Proton Linac" *Nuclear Instruments and Methods in Physics Research A*, vol. 588 (3), pp. 359-374, 2007.
- [56] Kim, H., *et al.*, "Superconducting linac for the Rare Isotope Science Project." *J. Korean Physics Society*, vol. 66 (3), pp. 413-418, 2015.
- [57] Jones, J. *et al.*, "Detection of shielded nuclear material in a cargo container," *Nuclear Instruments and Methods in Physics Research A*, vol. 562, pp. 1085-1088, 2006.
- [58] University of Cincinnati. (2015). "Generation of Bremsstrahlung," [Online] Available <http://cmap.ucfilespace.uc.edu:8085/rid=1L7GLWXM3-C57CXQ-4YK/brems.gif> [Accessed 11 Nov 2016]
- [59] Kosako, K., *et al.*, "Angular Distributions of Photoneutrons from Copper and Tungsten Targets Bombarded by 18, 28, and 38 MeV Electrons." *Journal of Nuclear Science and Technology*, 48 (2), pp. 227-236, 2011.
- [60] U.S. NRC. (2015). "Units of radiation dose," [Online]. Available: <http://www.nrc.gov/reading-rm/doc-collections/cfr/part020/part020-1004.html>. [Accessed 25 Aug 2016].
- [61] Pelowitz, D., MCNPX User's Manual Version 2.7.0 LA-CP-11-00438, 2011.
- [62] 10 CFR § 20.1301 Radiation Dose Limits for Individual Members of the Public. 1991. [Online] Available: <http://www.nrc.gov/reading-rm/doc-collections/cfr/part020/full-text.html#part020-1301> [Accessed 04 June 2014].

- [63] Varian Medical Systems. (2016). "Linatron-M6 & M6A Modular high-energy X-ray source," [Online] Available: https://www.varian.com/sites/default/files/resource_attachments/LinatronM6.pdf. [Accessed 01 Aug 2015].
- [64] Varian Medical Systems (2016) "Linear Accelerators - Linatron M," [Online] Available: <https://www.vareximaging.com/products/linear-accelerators>. [Accessed 26 Mar 2016]
- [65] Varian Medical Systems. (2016). "Linatron K15 Modular high -energy X-ray source," [Online] Available: https://www.varian.com/sites/default/files/resource_attachments/LinatronK15.pdf. [Accessed 26 Mar 2016].
- [66] Varian Medical Systems. (2016). "Linear Accelerators - Linatron K15," [Online] Available: <https://www.vareximaging.com/products/linear-accelerators>. [Accessed 26 Mar 2016]
- [67] National Institute of Biomedical Imaging and Bioengineering. "Computational Modeling." 2016 [Online] Available: <https://www.nibib.nih.gov/science-education/science-topics/computational-modeling>. [Accessed 4 Feb 2017]
- [68] Kirkby, C. *et al.*, "RBE of KV CBCT Radiation Determined by Monte Carlo DNA Damage Simulations." *Physics in Medicine and Biology*, vol.58 (16), pp. 5693-5704. 2013.
- [69] Carlson, D., *et al.*, "Combined Use of Monte Carlo DNA Damage Simulations and Deterministic Repair Models to Examine Putative Mechanisms of Cell Killing." *Radiation Research*, vol. 169 (4), pp. 447-459, 2008.
- [70] Eylenceoglu, E., *et al.*, "Two-dimensional hybrid Monte Carlo-fluid modelling of dc glow discharges: Comparison with fluid models, reliability, and accuracy," *Physics of Plasmas*, vol. 22 (1), pp. 013509-1–013509-9, 2015.
- [71] Heerikhuisen, J., *et al.*, "Interaction between the solar wind and interstellar gas: A comparison between Monte Carlo and fluid approaches." *Journal of Geophysics Research: Atmosphere.*, vol. 111 (A6), 2006.
- [72] Creal, D., 2012. "A Survey of Sequential Monte Carlo Methods for Economics and Finance." *Economics Review*, vol. 31 (3), 2012.
- [73] Tadeu, H., and Silva, J., "An empirical analysis using private investments cross analyses method (PICAM) and Monte Carlo simulation to evaluate economic sector performance." *WSEAS Transactions on Business Economics*, vol. 12, 2015.
- [74] X-5 MonteCarloTeam, 2003.MCNP-Version5,Vol.I:Overview and Theory,LA- UR-03–1987.
- [75] Pelowitz, D.B., MCNP6 Users Manual Version Version 1.0 LA-CP-13-00634, 2013.

- [76] Bednarz, B., "Detailed Varian Clinac Accelerator Modeling for Calculating Intermediate- and Low-Level Non-Target Organ Doses from Radiation Treatment," Ph.D. Dissertation, Rensselaer Polytechnic Institute, Troy, NY, 2008.
- [77] Ghassal, N., and Ajaj, F., "An MCNP-Based Model of a Medical Linear Accelerator X-Ray Photon Beam," *Australasian Physical & Engineering Sciences in Medicine* vol. 26 (3) pp. 140-144, 2003.
- [78] Ding, G., "Energy Spectra, Angular Spread, Fluence Profiles and Dose Distributions of 6 and 18 MV Photon Beams: Results of Monte Carlo Simulations for a Varian 2100EX Accelerator," *Physics in Medicine and Biology* vol. 47 (7), pp.1025-1046, 2002.
- [79] Mesbahi, A., *et al.*, "Development and Commissioning of a Monte Carlo Photon Beam Model for Varian Clinac 2100EX Linear Accelerator," *Applied Radiation and Isotopes*, vol. 64 (6), pp. 656-662, 2006
- [80] Farajollahi, A., and Mesbahi, A., "Monte Carlo Dose Calculations for a 6-MV Photon Beam in a Thorax Phantom." *Radiation Medicine*, vol. 24 (4), pp. 269-276, 2006.
- [81] Lewis, R., *et al.*, "An MCNP-based model of a linear accelerator X-ray beam," *Physics in Medicine and Biology*, vol. 44(5), pp. 1219–1230, 1999.
- [82] Udale-Smith, M. "Monte Carlo Calculations of Electron Beam Parameters for Three Philips Linear Accelerators." *Physics in Medicine and Biology*" vol. 37 (1), pp. 85-105, 1992.
- [83] Catchpole, M., "Comparison of Secondary Neutron Dose from 10 MV Intensity Modulated Radiation Therapy and Volume Modulated Arc Therapy," M.S. Thesis, Department of Nuclear Engineering and Radiation Health Physics, Oregon State University, Corvallis, OR 2010.
- [84] Carinou, E., *et al.*, "An MCNP-based model for the evaluation of the photoneutron dose in high energy medical electron accelerators." *Physica Medica*. 21 (3), pp. 95-99, 2005
- [85] Patil, B., *et al.*, "Estimation of neutron production from accelerator head assembly of 15 MV medical LINAC using FLUKA simulations." *Nuclear Instruments and Methods in Physics Research B*, vol. 269 (24), 3261–3265, 2011.
- [86] Mohammadi, N., *et al.*, "Neutron spectrometry and determination of neutron contamination around the 15 MV Siemens Primus LINAC," *Journal of Radioanalytical and Nuclear Chemistry*, vol. 304 (3), pp. 1001-1008, 2015.
- [87] Zanini, A., *et al.*, "Monte Carlo simulation of the photoneutron field in linac radiotherapy treatments with different collimation systems," *Physics in Medicine and Biology*, vol. 49 (4), pp. 571-582, 2004.
- [88] Vega-Carillo, H., and Baltazar-Raigosa, A., "Photoneutron spectra around an 18 MV LINAC," *Journal Of Radioanalytical and Nuclear Chemistry*, vol. 287 (1), pp. 323-327, 2011.

- [89] Torabi, F., *et al.*, "Photoneutron production by a 25 MeV electron linac for BNCT application." *Annals of Nuclear Energy*, vol. 54, pp. 192-196, 2013.
- [90] Baker, C., and Thomas, S., "Neutron Transport in a Clinical Linear Accelerator Bunker: Comparison of Materials for Reducing the Photo-Neutron Dose at the Maze Entrance," *Radiation Physics and Chemistry*, vol. 61 (3), pp. 633-634, 2001.
- [91] Garnica-Garza, H., "Characteristics of the Photoneutron Contamination Present in a High-Energy Radiotherapy Treatment Room." *Physics in Medicine and Biology*, vol. 50 (3), pp. 531-539, 2005.
- [92] Mahdavi, S., 2009. "MCNP Estimation of Photoneutrons of Hi-Energy Linac in Treatment Room and Maze." *Radiotherapy and Oncology*, vol. 92 (1), S236.
- [93] Ghassoun, J., "Neutron and photon doses in high energy radiotherapy facilities and evaluation of shielding performance by Monte Carlo method." *Annals of Nuclear Energy*, vol. 38, pp. 2163–2167. 2011
- [94] R. McConnell, *et al.*, "Compendium of Material Composition Data for Radiation Transport Modeling," Pacific Northwest National Laboratory. Report No. PNNL-15780, 2011. [Online] Available:http://www.pnnl.gov/main/publications/external/technical_reports/pnnl-15870rev1.pdf. [Accessed 15 Dec 2015].
- [95] J. Verbeke, *et al.*, "Simulation of Neutron and Gamma Ray Emission from Fission and Photofission," Lawrence Livermore National Laboratory, UCRL-AR-228518. 2014.
- [96] ANSI/ANS 6.1.1-1977, "Neutron and Gamma-ray Flux-to-Dose-Rate Factors," ANSI, 1977
- [97] Hughes, H., "Treating Electron Transport in MCNP" LA-UR-96-4583. 1997.
- [98] Centre for Photonuclear Experiments Data "Reaction Thresholds and Energies," 2010. [Online] Available: http://cdfc.sinp.msu.ru/services/calc_thr/calc_thr.html [Accessed 14 Jan 2017]
- [99] Kavouras, J., "Detection and simulation of delayed γ -rays from photofission," M.S. Thesis, Department of Civil and Environmental Engineering, University of Utah, Salt Lake City, UT 2014
- [100] Kane, S., "Detection of Special Nuclear Materials Using Prompt Gamma-Rays from Fast and Slow Neutron-Induced Fission," PhD Dissertation, Department of Nuclear Engineering, Purdue University, West Lafayette, IN, 2010.
- [101] Carrel, F., "New Experimental Results on the Cumulative Yields From Thermal Fission of ^{235}U and ^{239}Pu and From Photofission of ^{235}U and ^{238}U Induced by Bremsstrahlung." *IEEE Transactions on Nuclear Science*, vol. 58 (4), pp. 2064-2072, 2011.

- [102] Jacobs, E., *et al.*, "Product yields for the photofission of ^{238}U with 12-, 15-, 20-, 30-, and 70-MeV bremsstrahlung," *Physical Review C*, vol. 19, pp. 422–432, 1979.
- [103] Jacobs, E., *et al.*, "Product yields for the photofission of ^{235}U with 12-, 15-, 20-, 30-, and 70-MeV bremsstrahlung," *Physical Review C* 21, pp. 237–245, 1980.
- [104] Wehe, D., *et al.*, "Observation of ^{238}U photofission products," *IEEE Transactions on Nuclear Science*, vol. 53 (3), pp. 1430-1434, 2006
- [105] Wen, X., and Yang, H., "Photofission product yields of ^{238}U and ^{239}Pu with 22 MeV bremsstrahlung," *Nuclear Instruments and Methods in Physics Research A*, vol. 821, pp. 34-39, 2016
- [106] Dore, D., "Delayed neutron yields and spectra from photofission of actinides with bremsstrahlung photons below 20 MeV," *Journal of Physics: Conference Series*, vol. 41, pp. 241-247, 2006.
- [107] Kouzes, R. (2009). "The ^3He Supply Problem," Pacific Northwest National Laboratory [Online] Available: http://www.pnl.gov/main/publications/external/technical_reports/PNNL-18388.pdf. [Accessed 11 Feb 2017]
- [108] Shea, D., and Morgan, D., (2010). "The Helium-3 Shortage: Supply, Demand, and Options for Congress" [Online] Available: <http://www.fas.org/sgp/crs/misc/R41419.pdf>. [Accessed 13 Feb 2017]
- [109] Richardson, N., "Time Correlated Measurements Using Plastic Scintillators with Neutron-Photon Pulse Shaped Discrimination." M.S. Thesis, Department of Mechanical Engineering, University of Nevada, Las Vegas, Las Vegas, NV, 2014.
- [110] Guckes, A., "Modeling of Time-Correlated Detection of Fast Neutrons Emitted in Induced SNM Fission." *Physics Procedia*, vol. 66, pp. 403-409, 2015.
- [111] "Pulse Shape Discrimination EJ-299-33A, EJ-299-34." [Online] Available: <http://www.eljentechnology.com/products/plastic-scintillators/ej-299-33a-ej-299-34>. [Accessed 11 Feb 2017].
- [112] Zaitseva, N., *et al.*, "Plastic scintillators with efficient neutron / gamma pulse shape discrimination," *Nuclear Instruments and Methods in Physics Research A*, vol. 668, pp. 88–93. 2012.
- [113] Bridgeport Instruments, "eMorpho - Multichannel Analyzer for Scintillator Detectors." [Online] Available http://www.bridgeportinstruments.com/products/emorpho/emorpho_brief_u11.pdf. [Accessed 11 Feb 2017]

- [114] Hamel, M., "A fluorocarbon plastic scintillator for neutron detection: Proof of concept", *Nuclear Instruments and Methods in Physics Research A*, vol. 768, pp. 26-31, 2014.
- [115] Ovechkina, L., "Gadolinium-loaded Plastic Scintillators for high efficiency neutron detection", *Physics Procedia*, vol 2, pp. 161-170, 2009.
- [116] Dumazert, J., "Gadolinium-loaded Plastic Scintillators for Thermal Neutron Detection using Compensation", *IEEE Transactions on Nuclear Science*, vol. 63 (3), pp. 1551-1564, 2016.
- [117] Pozzi, S. *et al.*, "Pulse shape discrimination in the plastic scintillator EJ-299-33," *Nuclear Instruments and Methods in Physics Research A*, vol. 723, pp. 19-23, 2013.
- [118] Cester, d. *et al.*, "Experimental tests of the new plastic scintillator with pulse shape discrimination capabilities EJ-299-33," *Nuclear Instruments and Methods in Physics Research A* vol. 735, pp. 202-206, 2014.
- [119] Bourne, M., *et al.*, "Cross-correlation measurements with the EJ-299-33 plastic scintillator" *Nuclear Instruments and Methods in Physics Research A*, vol. 784, pp. 460-464, 2015.
- [120] Pozzi, S., *et al.*, "Plutonium metal vs. oxide determination with the pulse-shape-discrimination-capable plastic scintillator EJ-299-33," *Nuclear Instruments and Methods in Physics Research A*, 767, pp. 188-192, 2014.
- [121] Liao, C., and Yang, H., "Pulse shape discrimination using EJ-299-33 plastic scintillator coupled with a silicon photomultiplier array," *Nuclear Instruments and Methods in Physics Research A*, vol. 789, pp. 150-157, 2015.
- [122] Hartman, J., *et al.*, "Measurements of response functions of EJ-299-33A plastic scintillator for fast neutrons," *Nuclear Instruments and Methods in Physics Research A.*, vol. 804, pp. 137-143, 2015.
- [123] Hartman, J. " Neutron Spectroscopy with Scintillation Detectors using Wavelets," M.S. Thesis, Department of Mechanical Engineering, University of Nevada, Las Vegas, Las Vegas, NV, 2014.
- [124] IAEA, "Average number of neutrons emitted per fission [Online]. Available: <https://www-nds.iaea.org/sgnucdat/a6.htm>. [Accessed 1 February 2017].
- [125] Enqvist, A., *et al.*, "A combined neutron and gamma-ray multiplicity counter based on liquid scintillation detectors," *Nuclear Instruments and Methods in Physics Research A*, vol. 652, pp. 48-51, 2011.

[126] Flaska, M., *et al.*, "Measurement of FastNeutron/Gamma-Ray Cross- Correlation Functions with Cf-252 and Pu-Be Neutron Sources," *IEEE Nuclear Science Symposium Conference Record*, vol. 13 (243), pp. 961-963, 2009.

[127] Pozzi, S., *et al.*, "Pulse Height Distributions of Neutrons and Gamma-Rays from Plutonium Oxide." *Nuclear Instruments and Methods in Physics Research A*, vol 608 (2), pp. 310-315, 2009.

[128] Miloshevsky, G., and Hassanein, A., "Multiplicity correlation between neutrons and gamma-rays emitted from SNM and non-SNM sources." *Nuclear Instruments and Methods in Physics Research B*, vol. 342, pp. 277-285, 2015.

[129] McKinney, G., *et al.*, "MCNPX 2.7.0 - New Features Demonstrated." LA-UR-12-25775, 2012.

Curriculum Vitae

Matthew Hodges
Matthew.S.Hodges@gmail.com

Education:

Ph.D., Mechanical Engineering, 2017
University of Nevada, Las Vegas

Master of Science, Materials and Nuclear Engineering, 2015
University of Nevada, Las Vegas

Graduate Certificate, Nuclear Safeguards and Security, 2015
University of Nevada, Las Vegas

Graduate Certificate, Nuclear Criticality Safety Engineering, 2015
University of Nevada, Las Vegas

Master of Science in Engineering, Mechanical Engineering, 2006
University of Nevada, Las Vegas

Bachelor of Science in Engineering, Chemical Engineering, 2003
Arizona State University

Publications, Conferences & Presentations

M. Hodges, A. Barzilov, Y. Chen, "Computational Analysis of Neutron Signatures for Photofission Assay of SNM Using a Varian K15 Linac." *13th International Topical Meeting on Nuclear Applications of Accelerators*, Quebec City, Quebec, Canada (To be presented August 2017)

M. Hodges, A. Barzilov, Y. Chen, D. Lowe, "Characterization of a 6 MeV Accelerator Driven Mixed Neutron/Photon Source." *Physics Procedia*, 2017 (under review)

M. Hodges, A. Barzilov, Y. Chen, "Computational Study of 15 MeV Linac Radiation Doses at the UNLV Accelerator Facility." *2016 ANS Winter Meeting and Nuclear Technology Expo*, Las Vegas, NV (November 2016)

M. Hodges, A. Barzilov, Y. Chen, D. Lowe, "Characterization of a 6 MeV Accelerator Driven Mixed Neutron/Photon Source." *24th Conference on Application of Accelerators in Research and Industry*, Fort Worth, Texas (November 2016)

M. Hodges, A. Barzilov, Y. Chen, D. Lowe, "Varian K15 linac radiation environment at the UNLV accelerator facility." *13th International Conference on Radiation Shielding*, Paris, France (October 2016).

M. Hodges, A. Barzilov, Y. Chen, D. Lowe, "Characterization of the radiation environment at the UNLV accelerator facility during operation of the Varian M6 linac." *Radiation Physics and Chemistry*. 127 (October 2016), 72-77. <http://dx.doi.org/10.1016/j.radphyschem.2016.06.010>

M. Hodges, A. Barzilov, Y. Chen, D. Lowe, "Characterization of the radiation environment at the UNLV accelerator facility." *2015 ANS Winter Meeting and Nuclear Technology Expo*, Washington DC (November 2015).

M. Hodges, C. Sanders, "Nuclear criticality accident safety, near misses and classification," *Progress in Nuclear Energy*, 76 (2014): 88-99. <http://dx.doi.org/10.1016/j.pnucene.2014.05.018>

M. Hodges, "Nuclear Fallout Models - An Overview," DOE/NV/25946--2230, October 2014, National Security Technologies Remote Sensing Laboratory, Las Vegas, NV. Report.

M. Hodges, "Nuclear Fallout Models - An Overview," DOE/NV/25946--2268, October 2014, National Security Technologies Remote Sensing Laboratory, Las Vegas, NV. Presentation.

Y. Chen, J. Nie, A. Johnson, M. Hodges, A. Hechanova, "Energy Analysis of Bayonet Heat Exchanger and Decomposer For Hydrogen Production," *Societe Francaise D'Energie Nucleaire (SFEN) Global 2009: The Nuclear Fuel Cycle: Sustainable Options and Industrial Perspectives*, Paris, France (September 2009)

M. Chang, H. T. Hsieh, Y. T. Chen, M. Hodges, G. Vandegrift, J. Copple, and J. Laidler, "Development of an Integrated Systems Engineering Modeling Package for Chemical Separation Processes under Advanced Fuel Cycle Initiative," *International Conference on Advances in Nuclear Power Plants (ICAPP)*, Anaheim, CA (June 2008), pg 2014

M. Chang, H. Hsieh, Y. Chen, M. Hodges, G. Vandergrift, J. Copple, J Laidler, "Development of an Object-Oriented Integrated Systems Engineering Modeling Package Using Unified Modeling Language (UML) For Chemical Separation Processes," *International Conference On Nuclear Engineering (ICONE)*, Orlando, Florida (May 2008)

M. Chang, H. Hsieh, Y. Chen, M. Hodges, G. Vandergrift, J. Copple, J Laidler, "An Object-Oriented Engineering Model Design For Integrating Spent Fuel Treatment Facility (SFTF) and Chemical Separation Processes," *International Conference On Nuclear Engineering (ICONE)*, Nagoya, Japan (April 2007)

M. Hodges, M. Chang, K. Kwan, H. Hsieh, Y. Chen, "An Object-Oriented Engineering Model Design For Integrating Spent Fuel Treatment Facility (SFTF) and Chemical Separation Processes," *International Mechanical Engineering Congress and Exposition (IMECE)*, Chicago, Illinois (November 2006)

K. Kwan, M. Hodges, H. Hsieh, Y. Chen "An Object Oriented Systems Engineering Model Design For Integrating Spent Fuel Extraction and System Progress," *International Mechanical Engineering Congress and Exposition*, Orlando, Florida (November 2005)

K. Kwan, M. Hodges, H. Hsieh, Y. Chen "An Object Oriented Systems Engineering Model Design For Integrating Spent Fuel Extraction and System Progress," *Energy Conversion and Resources 2005*, pg 121

Dissertation Title:

Fast Neutron Detection in Nuclear Material Photofission Assay Using a 15 MeV Linear Electron Accelerator

Dissertation Committee:

Co-Chairperson, Yi-Tung Chen, Ph.D.

Co-Chairperson, Alexander Barzilov, Ph.D.

Committee Member, William Culbreth, Ph.D.

Committee Member, Robert Boehm, Ph.D.

Committee Member, Ke-Xun Sun, Ph.D.

Graduate Faculty Representative, Daniel Gerrity, Ph.D.

Honors and Awards:

NRC Nuclear Engineering Ph.D. Fellowship, 2016-2017

18th Annual Graduate & Professional Student Research Forum - 2nd Place, Science and Engineering, 2016

NSTec National Security Scholarship, 2015-2016

NSTec Nuclear Engineering Fellowship, 2012-2014

ANS Member, 2012-current

ASU Honors College, 1998

Sun Devil Scholarship, 1998

Valedictorian (1 of 802) – High School Class of 1998, Cimarron-Memorial HS, Las Vegas, NV